Copyright Warning & Restrictions

The copyright law of the United States (Title 17, United States Code) governs the making of photocopies or other reproductions of copyrighted material.

Under certain conditions specified in the law, libraries and archives are authorized to furnish a photocopy or other reproduction. One of these specified conditions is that the photocopy or reproduction is not to be "used for any purpose other than private study, scholarship, or research." If a, user makes a request for, or later uses, a photocopy or reproduction for purposes in excess of "fair use" that user may be liable for copyright infringement,

This institution reserves the right to refuse to accept a copying order if, in its judgment, fulfillment of the order would involve violation of copyright law.

Please Note: The author retains the copyright while the New Jersey Institute of Technology reserves the right to distribute this thesis or dissertation

Printing note: If you do not wish to print this page, then select "Pages from: first page # to: last page #" on the print dialog screen

The Van Houten library has removed some of the personal information and all signatures from the approval page and biographical sketches of theses and dissertations in order to protect the identity of NJIT graduates and faculty.

ABSTRACT

SYNTHESIS AND CHARACTERIZATION OF PLASMA ENHANCED CHEMICALLY VAPOR DEPOSITED TANTALUM FILMS

by
Weizhong Chen

A low temperature inorganic plasma-enhanced chemical vapor deposition (PECVD) process has been developed for the growth of Ta using tantalum pentachloride ($TaCl_5$) as the preferred precursor and hydrogen as the reactant gas. Ta coatings were deposited at substrate temperature of 370~400 °C, reactor working pressures of 0.7-2 Torr, hydrogen carrier flow rate of 10-20 sccm, hydrogen reactant flow rates of 500 sccm, and plasma power ranging from 60 to 100W. Ta coatings were characterized with respect to their chemical, structural, and morphological properties by Auger electron spectroscopy (AES), x-ray diffraction (XRD), atomic force microscopy (AFM), x-ray photoelectron spectroscopy (XPS), scanning electron microscopy (SEM), and x-ray reflectivity (XRR). The hydrogen concentration was detected by NRA. These studies indicated that α phase predominant Ta coatings with traces of oxygen, carbon, chlorine, and hydrogen were deposited by PECVD method.

The coatings properties had been investigated in relation to deposition temperature, precursor temperature, RF input power, plasma working distance and reactant concentration. The growth rate was significantly enhanced by decreasing the plasma working distance between the plasma shower head and substrate. The growth rate increased with increasing in the precursor temperatures and deposition temperatures. The plasma working distance was also discussed as the main experimental parameter to cause α-phase formation in PECVD Ta deposition. The in-situ annealing process was produced

to evaluate effects of thermal treatment of Ta phase formation. XRR measurements showed that the density of the CVD Ta coatings is closed to that of bulk Ta.

The various seed layers were used to try to promote the α-phase formation, such as Cr, Au, Nb, Pt, Ti, and TaNx. Tantalum coatings had successfully been deposited on all different seed layers. The SEM results exhibited dense Ta coatings with perfectly conformal coverage. The typical topography of CVD Ta coatings were indicated by AFM analysis. The α-phase promoting effect of those seed layers was indicated by XRD analysis. XRD analysis indicates that mixture α and β phase were deposited on the Cr seed layers, but Cr seed layers do not promote α phase formation. However, sputtered Cr gave more crystalline β phase formation. CVD Ta coatings deposited on Nb and Au seed layers no longer exhibited evidence of β phase. XRD results of CVD Ta coatings deposited on TaN_x seed layers showed predominant presence of α phase formation.

SYNTHESIS AND CHARACTERIZATION OF PLASMA ENHANCED CHEMICALLY VAPOR DEPOSITED TANTALUM FILMS

by
Weizhong Chen

A Dissertation
Submitted to the Faculty of
New Jersey Institute of Technology and
Rutgers, The State University of New Jersey-Newark
in Partial Fulfillment of the Requirements for the Degree of
Doctor of Philosophy in Applied Physics

Federated Physics Department

May 2008

Copyright © 2008 by Weizhong Chen

ALL RIGHTS RESERVED

APPROVAL PAGE

SYNTHESIS AND CHARACTERIZATION OF PLASMA ENHANCED CHEMICALLY VAPOR DEPOSITED TANTALUM FILMS

Weizhong Chen

4/14/08

Dr. Roland A. Levy, Dissertation Advisor — Date
Distinguished Professor of Physics, NJIT

4/14/08

Dr. Haimin Wang, Committee Member — Date
Distinguished Professor of Physics, NJIT

4/14/08

Dr. Nuggehalli M. Ravindra, Committee Member — Date
Professor of Physics, NJIT

Dr. Trevor A. Tyson, Committee Member — Date
Professor of Physics, NJIT

4/14/08

Dr. Durga Misra, Committee Member — Date
Professor of Electrical and Computer Engineering, NJIT

BIOGRAPHICAL SKETCH

Author: Weizhong Chen

Degree: Doctor of Philosophy

Date: May 2008

Undergraduate and Graduate Education:

- Doctor of Philosophy in Applied Physics,
  New Jersey Institute of Technology, Newark, NJ, 2008
- Master of Science in Physics,
  Lanzhou Institute of Physics, Lanzhou, P. R. China, 2000
- Bachelor of Material Science & Engineering,
  Xi'an Technological University, Xi'an, P. R. China, 1997

Major: Applied Physics

Presentations and Publications:

"Low Temperature Inorganic Plasma Enhanced Chemical Vapor Deposition of alpha phase Tantalum on high strength Steel", Weizhong Chen, Yong Seok Suh, Sungmin Maeng, Sipeng Gu, Roland A. Levy. (preparing 2008)

"Investigation of Chemically Vapor Deposited Tantalum for Medium Caliber Gun Barrel Protection", New Jersey Institute of Technology Advisory Board Meeting, NJIT, Newark, NJ, 9 April 2008.

"Investigation of Chemically Vapor Deposited Tantalum for Medium Caliber Gun Barrel Protection", SERDP/ESTCP Partners in Environmental Technology Symposium & Workshop, December 4-6, 2007, Washington, DC.

"Investigation of Chemically Vapor Deposited Tantalum for Medium Caliber Gun Barrel Protection", New Jersey Institute of Technology Advisory Board Meeting, NJIT, Newark, NJ, 11 April 2007.

"Investigation of Chemically Vapor Deposited Tantalum for Medium Caliber Gun Barrel Protection", SERDP/ESTCP Partners in Environmental Technology Symposium & Workshop, November 28 – 30, 2006, Washington, DC.

Yong Seok Suh, Weizhong Chen, Sung Min Maeng, Roland A. Levy, Hareesh Thridandam, Kirk S. Cuthill, T. Gaffney, "Investigation of Plasma Enhanced Chemically Vapor Deposited Tantalum on High Strength Steels", Material Science and Technology Conference Proceedings, PP 563-572, Detroit, MI, 16-20 September 2007.

Weizhong Chen, Chang Liu, Hui Song, Na Deng, Changyi Tan, and Haimin Wang, "Statistical Study of Rapid Sunspot Structure Change Associated with Flares", 2007, Chin. J. Astron. Astrophys. 7(5), 733-742.

Hui Song, Vasyl Yurchyshyn, Guo Yang, Changyi Tan, Weizhong Chen and Haimin Wang, "The Automatic Predictability of Super Geomagnetic Storms from Halo CMES Associated with Large Solar Flares", 2006, Solar Phys. 238,141.

This dissertation is dedicated to my beloved wife, Kexin Zhang,

and my parents, 陈 永 志 and 张 玉 香,

for their love, encouragement, and support.

ACKNOWLEDGMENT

I would like to address my deepest appreciation to my dissertation advisor, Dr. Roland A. Levy, who not only served as my research supervisor, providing valuable and countless resources, insight, and intuition, but also constantly gave me support, encouragement, and reassurance.

I am also deeply grateful to Dr. Haimin Wang who not only served as a committee member and mentor, but also always provided me with much valuable guidance and suggestions throughout my entire PhD period.

Special thanks are due towards Dr. Trevor A. Tyson, Dr. Nuggehalli M. Ravindra, and Dr. Durga Misra for serving as committee members and their helpful suggestions.

I would also like to thank Dr. Yong Seok Suh, Dr. Sung Min Maeng, and Sipeng Gu for their encouragement and friendship throughout these years. Many of my fellow graduate students in the Physics department are deserving of recognition for their support. I would like to extend my grateful to all my friends and colleagues at NJIT. I thank you for having made these days enjoyable and unforgettable at NJIT. I am going to miss u forever!

Last, but certainly not the least, I thank my parents, Chen Yongzhi and Zhang Yuxiang, for being my permanent source of love and strength, and my wife, Zhang Kexin, for her constant loving support and encouragement, so that I could achieve this degree. I would like to thank my sister Huifen Chen and her family for their loving support, and taking care of our parents in China. Therefore, this work is dedicated to them.

TABLE OF CONTENTS

Chapter **Page**

1 INTRODUCTION AND TECHNOLOGY REVIEW 1

1.1 Introduction 1

1.1.1 Objective 1

1.1.2 Background Information 1

1.1.3 Research Purpose of this Thesis 2

1.2 Review of Technology 3

1.2.1 The Structural Properties of Tantalum 3

1.2.2 Literature Overview 7

1.2.3 Chemical Vapor Deposition Theory 9

1.2.4 Characterization of Plasma 15

1.2.5 Plasma Enhanced CVD 18

2 EXPERIMENTAL PROCEDURE 23

2.1 Introduction 23

2.2 PECVD Reactor 24

2.3 Temperature Correction 25

2.4 Determination of Precursors 26

2.4.1 Main Requirements 26

2.4.2 Candidate Precursors for CVD Tantalum 27

2.5 Deposition Procedure 31

2.5.1 Precursor Flow Rate Calibration 31

2.5.2 Preparation of Samples 33

TABLE OF CONTENTS
(Continued)

Chapter **Page**

2.5.3 Film Deposition 34

2.6 Characterization Techniques 34

2.6.1 Scanning Electron Microscopy (SEM) 35

2.6.2 Energy-Dispersive X-Ray (EDX) 37

2.6.3 X-Ray Diffraction (XRD) 38

2.6.4 Atomic Force Microscopy (AFM) 40

2.6.5 X-Ray Reflectivity (XRR) 43

2.6.6 X-Ray Photoelectron Spectroscopy (XPS) 45

2.6.7 Auger Electron Spectroscopy (AES) 47

2.6.8 Nuclear Reaction Analysis (NRA) 48

3 THERMODYNAMIC CALCULATIONS 49

3.1 Reaction Feasibility 49

3.2 Thermodynamic Calculations 50

4 PLASMA ENHANCED CVD TANTALUM ON HIGH STRENGTH STEELS 54

4.1 Introduction 54

4.2 Topographical Characterization 54

4.3 Step Coverage Characterization 57

4.4 Compositional Analysis 58

4.4.1 AES Depth Profile Analysis 58

4.4.2 XPS Analysis 59

4.5 Crystallographic Structures Analysis 61

TABLE OF CONTENTS
(Continued)

Chapter **Page**

4.5.1 The Crystallographic Structures Changed with Plasma Working Distance in PECVD Ta coatings 61

4.5.2 Effects of Thermal Treatment on Ta Microstructure 63

4.6 Hydrogen Concentration Detected 65

4.7 X-ray Reflectivity Analysis 66

4.8 Establish Growth Rate Dependence on Processing Parameters 66

4.8.1 Growth Rate with Respect to Precursor Temperature 66

4.8.2 Growth Rate with Respect to Plasma Power and Plasma Working Distance 67

4.8.3 Growth Rate with Respect to Substrate Temperature 68

4.9 Result and Discussion 71

5 PLASMA ENHANCED CVD TANTALUM ON VARIOUS SEED LAYERS 73

5.1 Introduction 73

5.2 Ta Coatings on Chromium Seed Layer 74

5.2.1 Surface Morphology and EDX analysis of Ta on Sputtered Cr Seed Layer 74

5.2.2 Surface Morphology and EDX analysis of Ta on Electroplated Cr Seed Layer 77

5.2.3 Ta Microstructure Comparison on Different Methods Deposited Cr Substrates 78

5.3 Ta Coatings on Au Seed Layer 80

5.4 Ta Coatings on Niobium Seed layer 83

5.5 Ta Coatings on Titanium Seed Layer 85

TABLE OF CONTENTS
(Continued)

Chapter **Page**

5.6 Ta Coatings on Platinum Seed Layer 88

5.7 Ta Coatings on Tantalum Nitride Seed Layer 90

5.7.1 Topographical Characterization 90

5.7.2 Step Coverage Characterization 91

5.7.3 Crystallographic Structures Analysis 92

5.8 Conclusion 94

6 CONCLUSION 95

REFERENCES 98

LIST OF TABLES

Table **Page**

1.1 Properties of Tantalum 5

2.1 The properties of tantalum halide precursors 30

2.2 Summary of PECVD Ta film properties obtained for each of the listed halide precursors 30

2.3 The evaporation rate of tantalum chloride 32

2.4 Polishing Procedure of Steel substrate 33

LIST OF FIGURES

Figure Page

1.1 (a) Structure of β-Uranium. (b) Stacking Arrangement in the structure of β-Uranium. 6

1.2 (a) $P\text{-}42_1m$ structure. (b) Stacking arrangement in $P\text{-}42_1m$ structure. 7

1.3 Fundamental steps of CVD process 12

1.4 Schematic representation of the plasma enhanced CVD reaction process 19

2.1 Schematic diagram of PECVD reactor. 25

2.2 Correlation of measured surface temperatures to setting temperatures. 26

2.3 Vapor pressure of tantalum halide precursors versus temperature. 30

2.4 $TaCl_5$ evaporation rate v.s. precursor temperature 32

2.5 (a) The formation of backscattered electrons, (b) The yield of secondary electrons and back scattered electrons relates with atomic number versus the incident electron energy 37

2.6 Elements in an EDX spectrum are identified based on the energy level. 38

2.7 The illustration for Bragg's Law 40

2.8 Schematic illustration of AFM 41

2.9 The Common AFM Modes: Contact Mode (left), Non-contact Mode (middle) and Tapping Mode (right). 42

2.10 Schematic illustration of photoelectron emission. 46

2.11 Schematic illustration of Auger Electron emission. 47

3.1 (a) Enthalpy and (b) Gibbs free energy change versus temperature. 53

LIST OF FIGURES
(Continued)

Figure **Page**

3.2 Gibbs free energy change in tantalum metallization reaction involving (a) hydrogen molecules (H2) and (b) active hydrogen atoms (H). 53

4.1 SEM surface images and EDX elemental analysis of CVD Ta coatings deposited inside nut.......... 55

4.2 SEM surface images of CVD Ta coatings deposited on AISI 4340 steel coupons: (a) 2K X (b) 100K X. 55

4.3 AFM topography on: (a) polished steel substrate as reference and (b) Ta coatings on polished steel substrate. (Both data scale is 50nm.) 56

4.4 The cross-sectional SEM images of (a) CVD Ta on polished steel coupon 57

4.5 SEM images of cross sections of CVD Ta coatings. 57

4.6 CVD Ta on V-grooved Si wafer (145 μm depth and 103 μm width) 58

4.7 AES spectra of CVD Ta coatings. 58

4.8 AES spectra of CVD Ta coatings on steel coupons produced under (a) 60 W (b) 100 W RF plasma power. 59

4.9 Depth profile of XPS spectra for CVD Ta coatings on polished steel substrate: (a) Ta 4f (b) O 1s (c) C 1s. 60

4.10 XRD patterns of CVD Ta coatings on polished steel substrates with different plasma power under different plasma working distance: (a) 1.5 inch, (b) 2 inch, and (c) 2.5 inch 63

4.11 XRD patterns of PECVD Ta coatings on polished steel substrates: (a) annealed at 460 °C 2 h, (b) annealed at 430 °C 1 h, (c) as-deposited, (d) α-Ta reference, and (e) β-Ta reference 64

4.12 XRD patterns of CVD Ta coatings on polished Ta foil substrates: (a) annealed at 460 °C 2 h, (b) annealed at 430 °C 1 h, (c) Ta foil, (d) α-Ta reference, and (e) β-Ta reference. 65

LIST OF FIGURES
(Continued)

Figure **Page**

4.13 Hydrogen depth profiles in as-deposited PECVD Ta films.................................. 66

4.14 The influence on the growth rate with the various precursor temperatures (process pressure = 2 Torr, deposition temperature = 430 °C, plasma power = 60W, plasma working distance = 1.5"). 67

4.15 The plot of the growth rate vs. RF plasma power: Deposition conditions (process pressure = 0.7 Torr, deposition temperature = 370 °C and precursor temperature = 110 °C).. 68

4.16 Deposition rate as a function of substrate temperature exemplifying diffusion controlled and surface-reaction controlled regimes.. 69

4.17 Variation of growth rate as a function of inverse substrate temperature: (■) mark (process pressure = 2 Torr, plasma power = 60 W, precursor temperature = 120 °C and plasma working distance = 1.5") 71

5.1 Comparison of SEM surface images of CVD Ta coatings deposited on sputtered Cr coated steel substrates under different magnification: (a,b) sputtered Cr coating only, (c,d) Ta on Cr-coated steel substrate 75

5.2 EDX patterns before and after Ta coated on sputtered Cr-coated polished steel substrate... 76

5.3 Ta AFM 3D and 2D topography of sputtered Cr coated on polished steel substrate (Data scale: 50nm, R_{RMS}=5.05nm.) 76

5.4 Comparison of SEM surface images of CVD Ta coatings deposited on electroplated Cr coated steel substrates: (a,b) electroplated Cr coating only, (c,d) Ta on Cr-coated steel substrate.. 77

5.5 EDX patterns of Ta on electroplated Cr-coated polished steel substrate.................. 78

5.6 Ta AFM 3D topography of electroplated Cr coated on polished steel substrate (Data scale: (a) 5 μm, (b) 1 μm; R_{RMS}=280.38nm.) 78

LIST OF FIGURES
(Continued)

Figure **Page**

5.7 Comparison of Ta XRD patterns on Sputtered Cr-coated (b) and electroplated Cr-coated (d) polished steel substrate. (a) Ta on sputtered Cr, (c) Ta on electroplated Cr, (e) α-Ta reference, and (f) β-Ta reference 79

5.8 Comparison of SEM surface morphology without (a,b) and with (c,d) Ta coatings on Au-coated steel substrates 80

5.9 EDX patterns of Ta on sputtered Au coated polished steel substrate 81

5.10 Ta AFM 3D and 2D topography of Au-coated on polished steel substrate (Data scale: 200nm, R_{RMS}=8.496nm.) 81

5.11 XRD patterns of CVD Ta coatings: (a) Ta on Au-coated polished steel substrate (b) Ta on Au-coated Si wafer, and (c) Au coating on polished steel substrate. 82

5.12 Grazing incidence XRD data of CVD Ta coated on Au with different grazing incidence angle: (a) 5°, (b) 3°, (c) 2°, and (d) 1° 82

5.13 Comparison of SEM surface images of CVD Ta coatings deposited on sputtered Nb-coated steel substrates: (a,b) sputtered Nb coating only, (c,d) Ta on Nb-coated steel substrate 83

5.14 EDX patterns of Ta on sputtered Nb coated polished steel substrate 84

5.15 Ta AFM 3D and 2D topography of sputtered Nb coated on polished steel substrate (Data scale: 400nm, R_{RMS} = 18.705 nm.) 84

5.16 XRD patterns of CVD Ta coatings on Nb coated polished steel substrates and Si wafer. 85

5.17 Comparison of SEM surface images of CVD Ta coatings deposited on sputtered Ti-coated steel substrates: (a,b) sputtered Ti coating only, (c,d) Ta on Ti-coated steel substrate. 86

5.18 EDX patterns of Ta on sputtered Ti coated polished steel substrate 86

5.19 Ta AFM 3D topography of sputtered Ti coated on polished steel substrate (Data scale: 400nm, R_{RMS} = 28.605 nm.) 87

LIST OF FIGURES
(Continued)

Figure **Page**

5.20 XRD patterns of CVD Ta coatings on Ti-coated polished steel substrates. 87

5.21 Comparison of SEM surface images of CVD Ta coatings deposited on sputtered Pt-coated steel substrates: (a,b) sputtered Pt coating only, (c,d) Ta on Pt-coated steel substrate. 88

5.22 EDX patterns of Ta on sputtered Pt-coated polished steel substrate. 89

5.23 Ta AFM 3D topography of Pt-coated on polished steel substrate (Data scale: 400nm, R_{RMS} = 129.04 nm.) 89

5.24 XRD patterns of CVD Ta coatings on Pt-coated polished steel substrates. 90

5.25 SEM surface images of CVD Ta coatings deposited on in-situ TaN_x on polished AISI 4340 steel coupons. 91

5.26 Ta AFM 3D and 2D topography of TaN_x seed layer on polished steel substrate (Data scale: 400nm, R_{RMS} = 26.196 nm.) 91

5.27 The cross-sectional SEM images of Ta coating on in-situ TaN_x seed layer on polished steel coupon 92

5.28 XRD patterns of CVD Ta coatings on TaN_x seed layer: (a) Ta on TaN_x (higher N_2 flow rate), (b) Ta on TaN_x (lower N_2 flow rate), (c) steel substrate, (d) α-Ta reference, and (e) β-Ta reference 93

CHAPTER 1

INTRODUCTION AND TECHNOLOGY REVIEW

1.1 Introduction

1.1.1 Objective

The overall objective of this program is to investigate the use of chemical vapor deposition (CVD) to produce high quality tantalum coatings for wear and erosion protection of medium caliber gun barrels. In addition to offering an environmentally benign alternative to chromium plating, this relatively low temperature process promises to provide high throughput, low cost, conformal step coverage, and coatings with desirable properties and performance.

1.1.2 Background Information

Chromium is widely used as a protective coating on the interior bore surfaces of medium caliber gun barrels to reduce the erosive effects of hot propellant gases and the mechanical effects of the projectiles. Current coatings are electro-deposited from aqueous solutions of hexavalent chromium, a known carcinogen and toxic substance that is strictly regulated and entails high disposal costs. In the past, chromium has proven to be quite effective due to its chemical inertness as well as its excellent adherence and close thermal match to the substrate. However, current lethality requirements have increased to the point where chromium has become thermally overmatched and the resulting wear life has declined to unacceptable levels. Furthermore, the cracking tendency of chromium remains a serious issue that is incompatible with the ever-increasing need for higher

muzzle energies (~20 MJ) and hotter propellants (~3700 °K). Chromium cracking provides a path for the hot propellant gases to reach the lower melting substrate, resulting in a lift-off of the coating and subsequent exposure of the underlying steel to excessive wear and erosion.

The dual challenge of replacing the toxic chromium plating process and extending the barrel life by introducing a superior wear and erosion material was addressed through the use of internally magnetized cylindrical magnetron sputtered (IM-CMS) of tantalum. The IM-CMS process is preferable to electro-plating for several reasons:

- It is a dry (non-aqueous) environmentally friendly process
- It offers an attractive plug-in solution to the existing gun barrel manufacturing sequence
- The properties of the underlying steel are unaffected by deposition of the sputtering coating
- Acceptable deposition rates can be attained
- Post-processing is unnecessary.

In comparison to chromium, tantalum offers advantages that include a higher melting point (2996 °C versus 1857 °C) and higher ductility (in case of α-Ta) that leads to better resistance to thermal shock and cracking and, thus, higher resistance to corrosive propellant by-products attack of the substrate.

1.1.3 Research Purpose of this Thesis

Although IM-CMS is an acceptable method for cylinders with internal diameters of 60 mm and greater, it has proven not to perform well on cylinders with diameters below 45 mm since the smaller bore diameter of medium caliber guns cannot accommodate the

critical ionization distance required for this process. Generally, sputtering is a room temperature process limits inter-diffusion at the substrate-coating interface. This creates adhesion difficulties, which in turn leads to more extensive surface preparation (cleaning). Furthermore, another important consideration particularly pertinent to medium caliber guns, where the bores are rifled as compared to being smooth for large caliber guns, is that sputtering is a "line-of-sight" technique, thus, limiting the uniform coverage required for proper wear and erosion protection along spiraled paths.

Chemical vapor deposition (CVD) offers promising solutions to the problems associated with IM-CMS coatings. Reported studies have demonstrated the use of CVD in producing tantalum coatings from tantalum halide sources [1-5]. High quality CVD tantalum coatings were produced at deposition temperatures in the range of 250 to 450°C with excellent step coverage in sub-micron trench structures with high aspect ratios [2].

1.2 Review of Technology

1.2.1 The Structural Properties of Tantalum

Tantalum is strong, ductile metal that is nearly immune to chemical attack at room temperature. It combines the inertness of glass with the strength and ductility of low-carbon steel and has a much higher heat transfer capability than glass. Tantalum metal possesses excellent resistant to erosion, chemical stability, histocompatibility, and robust mechanical properties to make it a particularly desirable material.

Tantalum is known in two distinct crystalline phases or structures: a stable body centered cubic (bcc) α-phase (Im3m space group, a=3.3Å) and the metastable tetragonal β-phase ($P4_2/mnm$ space group, a=5.313, c=10.194Å) known since 1965 [6-8], which

have very different physical and electrical properties. The structure of the tantalum obtained may be bcc, tetragonal, or amorphous which depends on deposition technique and condition used [9, 10].

1.2.1.1 α-phase Tantalum

The bulk tantalum has the α-phase Tantalum and possessed good chemical, thermal and mechanical properties, including a high melting temperature (2996 °C), high elastic modulus similar to that of steel, good ductility and formability, with a Knoop microhardness values of 300-400, and resistance to acids and aggressive hot propellant gases [11, 12]. The bcc-Ta has a superconducting transition temperature T_c of 4.4 K, a relatively low thermal conductivity (57 W/m °C), and a low electrical resistivity of 15-60 μΩ/cm [13, 14], which makes it good choice for the thin film interconnection and for protective coatings.

The structure of bulk tantalum is the bcc structure is (a = 3.3 Å). The lattice constant of bcc tantalum in thin films is usually larger than Ta bulk (a = ~ 3.30-3.4 Å) [15]; this is attributed to the inclusion of impurities in the film during the deposition process [16-18]. Because the bcc-Ta lattice can incorporate considerably larger amounts of reactive gases than β-Ta without changing its structure, bcc-films can have a much wider range of cell parameters than β-Ta films [19].

1.2.1.2 β-phase of Tantalum

The tetragonal structure, known also as β-phase, has been identified in sputtering tantalum films [7, 13, 20]. There is only one report on β-Ta grown in the bulk form [21]. The physical properties of β-phase tantalum are not well know, except that it is hard,

brittle, and thermally unstable, as it converts to α-phase tantalum upon heating to 750 °C [6, 7, 20]. Typical Knoop microhardness values for the β- Ta are greater than 900. These properties make β-Ta more susceptible to crack formation and failure, and hence less desirable for protective coating applications where thermal shock and high shear forces are present [13]. Comparing to α-Ta, the β-Ta has an order of magnitude higher electrical resistivity (170-210 μΩ/cm) [22, 23] which may be advantageous in microelectronic techniques in the fabrication of resistance and capacitance elements of microcircuits [24, 25]. The properties of the two phase of tantalum are listed in the Table 1.1 [7, 21]:

Table 1.1 Properties of Tantalum

Ta (Phase)	Structure	Density (g/cm^3)	Resistivity (μΩ-cm)	Temperature coef. of Resistance (ppm/°C)	Super Conductivity	Lattice constant (Å)	Knoop Hardness
α-Ta	Bcc	16.55-16.27	24-50	+500+1800	3.25	a=b=c=0.3306	300-400
β-Ta	Tetragonal	16.9	180-220	-100+100	0.5	a=b=1.0194 C=0.5313	900

Numerous crystal structures have been reported for β-Ta since its discovery. Read and Altman [7] proposed a tetragonal unit cell Ta with a=0.534, c=0.994 nm, containing 16 atoms with a theoretical density of about 16.9 $g.cm^{-3}$. Two tantalum structures for β-Ta thin films have been stood out from many proposed β-Ta structures as the most possible candidates. These two structures belong to the $P4_2/mnm$ (No. 136) and $P\text{-}42_1m$ (No. 113) space group, and are both tetragonal with 30 atoms per unit cell. However, $P\text{-}42_1m$ has a lower symmetry than $P4_2/mnm$.

***$P4_2/mnm$* Structure**

Moseley and Seabrook revealed that the crystal structure of β-Ta is isomorphous with β-uranium [26]. They derived a tetragonal structure with same space group

($P4_2/mnm$) as β-uranium for β-tantalum. The c/a ratio for β-tantalum (0.521) is close to that for β-uranium (0.526). The $P4_2/mnm$ structure contains 30 atoms per unit cell. Its structure is shown in Figure 1.1 (a-b), which is a composite of Holden's representation of the β-Uranium structure and of Pearson's representation of the σ-phase. The centrosymmetry of the β-uranium structure means that a planar configuration of the I, II, IV and V atoms, which comprise the B and C layers, is required for symmetry. Within the layers, the pseudohexagonal arrangement is not symmetry determined, but rather shows the influence of close packing on the atomic coordinates. The A layers composed by atom type III, which are not close packed, show a small puckering. These atoms form chains running along the c axis.

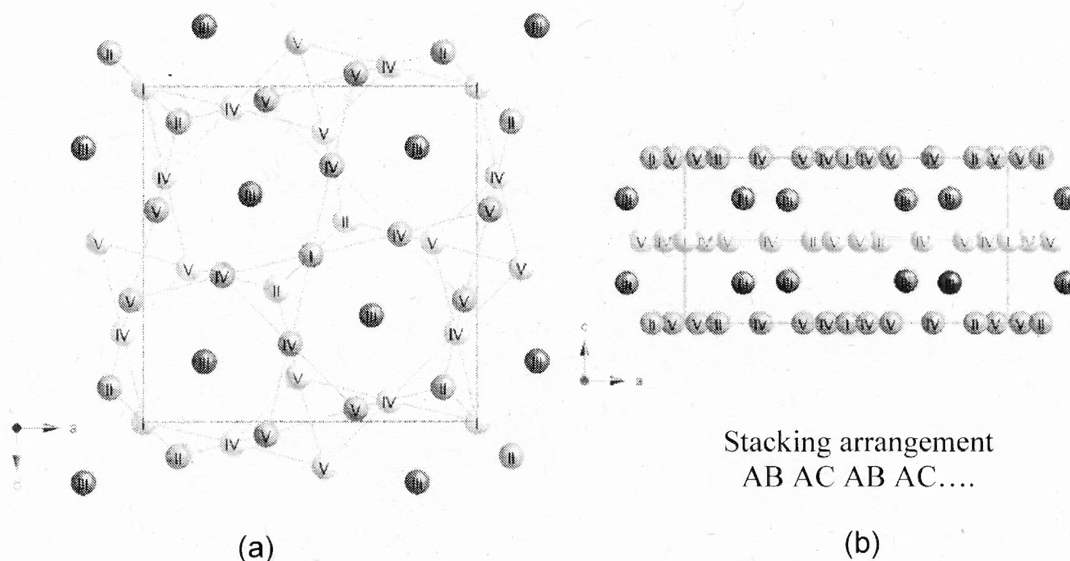

Figure 1.1 (a) Structure of β-Uranium. (b) Stacking Arrangement in the structure of β-Uranium.

$P\text{-}42_1m$ Structure

Arakcheeva et al. [27, 28] obtained single crystals of tetragonal β-tantalum for the first time at normal pressure by electrodeposition from a bath of molten fluorides. A self-hosting tetragonal structure with unit-cell parameters of a=1.021 1, c=0.53064 nm and

space group of $P\text{-}42_1m$ was determined for β-Ta. The $P\text{-}42_1m$ is shown in Figure 1.2 (a-b) it exhibits all the main features of a σ-phase [29], in spite of reducing the symmetry from $P4_2/mnm$ to $P\text{-}42_1m$. They are formed by the atomic positions A, B, C and D according to the accepted notation given in Frank & Kasper [29].

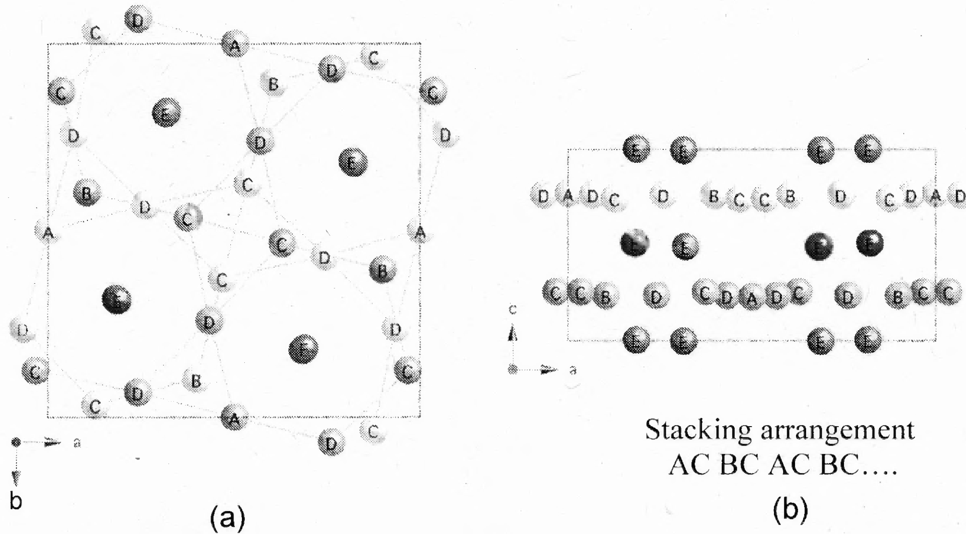

Figure 1.2 (a) $P\text{-}42_1m$ structure. (b) Stacking arrangement in $P\text{-}42_1m$ structure.

1.2.2 Literature Overview

A variety of methods has been developed to produce tantalum films, such as chemical vapor deposition [2, 30-33], electrochemical deposition [6], physical vapor deposition which including DC and RF sputtering [19, 34-36], electron beam evaporation [37-39], triode sputtering [40], ion beam assisted sputtering [41], and magnetron sputtering [9, 11, 42]. With these different deposition processes, the α-Ta, β-Ta or mixed phase tantalum coatings have been grown on different substrates according to specific deposition condition.

There are many factors can affect Tantalum nucleation and growth. However, it is still controversial to cause β phase formation. Numerous authors have reported effects of

impurity levels [35, 43, 44], oxygen and nitrogen concentrations [35], substrate temperature [12, 20, 35, 38], substrate type [45], sputtering gas species [40], deposition rate [46], and bias on tantalum phase formation [47-50], and the nature of the substrate[40].

Higher temperatures promoted the growth of α-Ta. Matson et al. [12, 20] reported that typically substrate temperatures been above 300 °C and as high as 600 °C were necessary to produce a completely bcc phase coating using an argon sputtering gas. Fischer [51] reported that pure Ta films deposited at substrate temperatures lower than 400 °C grow in the tetragonal modification. Increasing the substrate temperature (300 °C) caused the tantalum films initially nucleated as the β phase to be converted into α-Ta during film growth [11, 52]. Schauer and Roschy [35] found that in pure argon on sufficiently preheated substrates (> ~300 °C) a very pure bcc Ta phase was formed. β-Ta is known to be thermally unstable, transforming to the bcc phase in the temperature range of 600 to 800 °C, depending on deposition conditions [53, 54].

Feinstain and Hutteman [55] concluded that β-phase tantalum resulted when either oxygen or oxide was present on the substrate. They investigated twenty different substrates and classified them into three group: (I) oxides, such as glass, or substrates which readily form surface oxides in air at room temperature, which nucleated β-Ta; (II) substances such as Au which do not readily form oxides and nucleated bcc Ta; (III) substances that do not form surface oxides in air at room temperature, but which may be oxidized at elevated temperatures, these nucleated bcc Ta when freshly prepared and β-Ta when oxidized. Feinstain and Hutteman [55] also concluded that the formation of β-Ta or α-Ta was determined in the nucleation step. Once nucleated on their specific

substrates, β-Ta and α-Ta films will continue to grow side by side in the same sputtering ambient, even homogenous mixtures of β/α Ta. However, β-Ta nucleating substrates yield bcc Ta films in the growth stage if incorporated impurities exceed the solubility limit in the β-Ta.

Feinstein and Huttemann [55] work indicated that β-Ta is a metastable allotrope, and the O^{2-} or OH^{-} formed on surface oxide is necessary for the nucleation of β-Ta. Schauer and Roschy [35] reported that the formation of β-Ta may be produced either by impurities adsorbed on the surface or by adding oxygen or nitrogen to some degree to the sputtering argon atmosphere.

Sato [42] suggested that the role of OH^{-} on the substrate surface in the formation of β-Ta may be related to the limitation of the diffusion, which could assist the nucleation of β-Ta. Axelrod and Marcus [56] also reported that tantalum films deposited by nonreactive sputtering onto an oxide or glassy surface normally possess β-Ta structure. They concluded that β-Ta nucleates on an oxygen containing substrate, while bcc-Ta nucleates on a relatively oxygen-free substrate. Once nucleated, the respective structures continue to propagate under identical deposition conditions. In-situ resistivity measurement by Hieber and Mayer [57] demonstrated that tantalum nucleates as the β phase on oxide substrates (Corning 7059 glass, sapphire or BeO) at substrate temperatures above 25 °C.

1.2.3 Chemical Vapor Deposition Theory

Chemical Vapor Deposition (CVD) is one of the most important methods of film formation used in the fabrication of very large scale integrated (VLSI) silicon circuits, as well as of microelectronic solid state devices in general [58]. In this process, chemicals in

the gas or vapor phase are reacted at the surface of the substrate where form a solid production. A large variety of materials, particularly all those needed in microelectronic device technology, can be created by CVD. These materials comprise insulators and dielectrics, elemental and compound semiconductors, electrical conductors, superconductors and magnetics.

In addition to its unique versatility, this materials synthesis and vapor phase growth method can operate efficiently at relatively low temperatures. For example, refractory oxide gasses and metals can be deposited at low temperatures of only 300℃ to 500℃. This feature is very important in advanced VLSI devises with short channel lengths and shallow junctions, where lateral and vertical diffusion of the dopants must be minimized. This also helps minimizing process-induced crystallographic damage, wafer warpage and contamination by diffusion of impurities. Another important feature of CVD processing is the ease for creating films of both homogeneous and graded structures and of concisely controllable composition, features that are important in advanced microelectronic device fabrication. Unusual solid solutions and alloys can be prepared, as well as materials that cannot be readily obtained by other methods. Both chemicals composition and physical structure can be tailored by control of the reaction chemistry and deposition conditions.

1.2.3.1 Transport Phenomena of CVD

Chemical vapor deposition is defined as a process whereby constituents of the gas or vapor phase react chemically near or on the substrate surface to form a solid product. This product can be in the form of a thin film, a thick coating, or if allowed to grow, a massive bulk. It can have a single-crystalline, poly-crystalline, or amorphous structure.

Chemical and physical conditions during the deposition reaction can strongly affect the composition and structure of the product. This deposition technology has become one of the most means of creating thin films and coatings in solid state microelectronics where some of the most sophisticated purity and composition requirements must be met.

Chemical reaction types basic to CVD include pyrolysis (thermal decomposition), oxidation, reduction, hydrolysis, nitride and carbide formation, synthesis reactions, disproportionation, and chemical transport [58]. A sequence of several reaction types may be involved to create a particular end product. Some important basic aspects are involved in the CVD reactions. Volatility requirements dictate that the vapor pressure of liquid reactants is sufficiently high (usually when heated) to produce an adequate quantity of vapor that can be transported by a carrier gas to the reaction chamber. Solids must be melted and then treated like a liquid. Gaseous reactions, if available, are preferred since they can be readily meterd and introduced into the CVD reactor. The vapor pressure of side products must be high to facilitate their elimination from the reactor, whereas the resulting coatings product must have a low volatility to remain on the substrate. CVD reactions are homogeneous, heterogeneous, or a combination of both. Most CVD processes are chosen to be heterogeneous reactions. The sequence of the steps in the usual heterogeneous processes can be described as follows (shows in Figure 1.3) [59]:

a) Arrival of the reactants

- Bulk transport of reactants into the chamber,
- Gaseous diffusion of reactants to the substrate surface,
- Adsorption of reactants onto the substrate surface.

b) Surface chemistry

- Surface diffusion of reactants,
- Surface reactions.

c) Removal of by-products

- Desorption of by-products from the substrate surface,
- Gaseous diffusion of by-products away from the substrate surface,
- Bulk transport of by-products out of the reaction chamber.

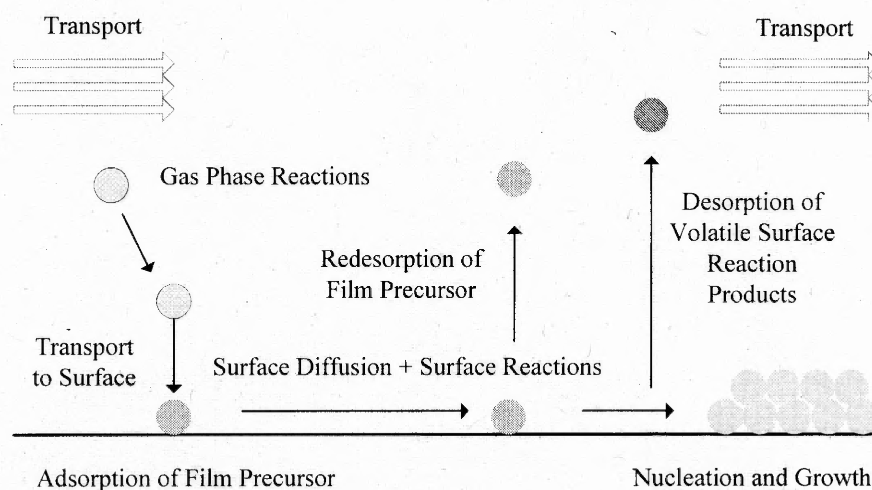

Figure 1.3 Fundamental steps of CVD process

1.2.3.2 Advantage and Limitation of CVD

In general, lower temperature and higher gas phase concentration favor formation of polycrystalline deposits. Under these conditions, the arrival rate at the surface is high, but the surface mobility of adsorbed atoms is low. Many nuclei of different orientation are formed, which upon coalescence result in a film consisting of many differently oriented grains. Further decrease in temperature and increase in supersaturation result in even more nuclei, and consequently in finer-grained films, eventually leading to the formation

of amorphous films when crystallization is completely prevented. Amorphous films include oxides, nitrides, carbides, and glasses are of great technical important for microelectronic applications. Deposition variables such as temperature, pressure, input concentrations, gas flow rates, reactor geometry and reactor opening principle determine the deposition rate and the properties of the film deposit.

Thin films are used in a host of applications in VLSI fabrication, and can be synthesized by a variety of techniques. Although CVD is a complex chemical system, CVD processes are often selected over competing deposition techniques because it offers the following distinctive advantages [60]:

- The capability of producing highly dense and pure materials.
- Produces uniform films with good reproducibility and adhesion at reasonably high deposition rates.
- CVD is a non-line-of-sight process with good throwing power. Therefore, it can be used to uniformly coat complex shaped components and deposit films with good conformal coverage. Such distinctive feature outweighs the PVD process.
- It has the ability to control crystal structure, surface morphology and orientation of the CVD products by controlling the CVD process parameters.
- Selective deposition can be obtained with proper design of the reactor.
- Deposition rate can be adjusted readily. Low deposition rate is favoured for the growth of epitaxial thin films for microelectronic applications. However, for the deposition of thick protective coatings, a high deposition rate is preferred and it can be greater than tens of μm per hour. This is substantially exceeded only by techniques such as plasma spraying.

- Reasonable processing cost for the conventional CVD technique.
- The flexibility of using a wide range of chemical precursors such as halides, hydrides, organometallics which enable the deposition of a large spectrum of materials including, metal, carbides, nitrides, oxides, sulphides, III–V and II–VI materials.
- Relatively low deposition temperatures and the desired phases can be deposited in-situ at low energies through vapour phase reactions, and nucleation and growth on the substrate surface. This enables the deposition of refractory materials at a small fraction of their melting temperatures.

Fundamental limitations of CVD are the chemical reaction feasibility and the reaction kinetics that govern the CVD processes. Technological limitations of CVD include the unwanted and possibly deleterious but necessary by-products of reaction that must be eliminated, and the ever present particle generation induced by homogeneous gas phase nucleation that must be minimized.

1.2.3.3 Classification of CVD Process Types

The energy to activate and drive the chemical processes can be thermal, supplied by an electric glow discharge plasma, or attained by electromagnetic radiation (usually ultraviolet or laser radiation). According to the type of energy supplied to initiate and sustain the reaction, CVD processes can be classified into following categories [58]:

- Thermally activated reactions at various pressure ranges, which comprise the vast majority of CVD processes. Heat is applied by resistance heating, RF inducting heating, or infrared radiation heating techniques.

- Photo induced reactions, where a specific wavelength radiation triggers and sustains the reaction by direct photolysis or by an energy transfer agent.
- Plasma promoted reactions, where an RF (or DC)-induced glow discharge is the source for most of the energy that initiates and enhances the rate of reaction, usually called plasma-enhanced CVD (PECVD).

The most important and widely used CVD processes are atmospheric pressure CVD (APCVD), low pressure CVD (LPCVD) and plasma enhanced CVD (PECVD). PECVD as the technique employed in this study will be discussed in detail.

1.2.4 Characterization of Plasma

The interactions of charged particles in the plasma over large distances imply that they seldom come close to one another and suffer a hard collision. However, the densities of charged particles in the plasma and the temperature of the plasma are important in determining the importance of hard collisions. If the density of charged particles in the plasma is high, the charged particles in the plasma may appear to present a dipole-like appearance to other charges and consequently hard collisions are important. At low temperatures, electrons and ions rapidly combine to form neutral atoms and molecules. Therefore, heating of a gas to a high temperature is one way to maintain plasma and clearly the density of charged particles increases with increase in temperature [61]. The plasma state depends on its comprised particles, the densities of particles and the temperature of particles. Most other parameters have relationship with these two parameters.

1.2.4.1 The Density of Particles and the Degree of Ionization

Plasma is a partially ionized gas consisting of equal numbers of positively and negatively charged particles, the remainder made up of unionized neutral particles and electromagnetic radiation [61]. Generally, n_e is electron densities, n_i is ion densities, and n_g is neutral densities. For a plasma composed of various of ions, at densities of n_{i1}, n_{i2}, n_{i3} ... and an electron density of n_e, the relation

$$n_e = n_{i1} + n_{i2} + n_{i3} + \ldots = n \quad (1.1)$$

should be satisfied for the plasma as a whole. This shows the electrical neutrality of the plasma, i.e., the plasma is macroscopically neutral in the equilibrium state, so that n is known as the plasma density. In most of cases, we mainly discuss the plasma which only the first level of ionization is of primary importance. Then we can approximatively consider $n_i \approx n_e$. The degree of ionization α can be defined as

$$a = \frac{n_e}{n_e + n_g} \quad \mathbf{(1.2)}$$

The relation between α, temperature T, and pressure P is given internal partition functions Q_g and Q_i for gas molecules and ions, respectively[62]

$$\frac{a^2}{1-a^2} = \left(\frac{2\pi m_e kT}{h^2}\right)^{3/2} kT \frac{2Q_i}{Q_g} \exp\left(-\frac{u_i}{kT}\right) \quad \mathbf{(1.3)}$$

Where m_e is the mass of electron, h is the Planck constant, and u_i is the ionization potential of gas molecule. This is known as the Saha equation, which is applied to the ionization of neutral molecule to a singly charged ion.

1.2.4.2 Plasma temperature

The temperature of the plasma is described according to the temperature of the respective particle: the electron temperature T_e, ion temperature T_i, and gas temperature T_g.

Considered "thermal capacitance", the macro temperature of plasma depends on the temperature of heavy particles. According to the temperature of particles, plasma can be classified into two groups: thermal equilibrium plasma and nonthermal equilibrium plasma.

When $T_e = T_i$, it is called thermal equilibrium plasma, or short for thermal plasma. This type of plasma has not only high electron temperature but also has high heavy particle temperature.

When $T_e \gg T_i$, it is called nonthermal equilibrium plasma. The electron temperature can higher than 10^4K. However, the heavy particles, like ions and atoms, can lower than 300~500K. Hence, it also is called "cold plasma" according to the temperature of heavy particles. Generally, cold plasma can be generated at low pressure which is below 100 Torr.

Plasmas are cold plasmas which are used for the deposition of thin films. It mainly is generated under the category of glow discharge at low pressures of about 10^{-3} to 10 Torr. These plasmas have average electron energies and electron densities in the range of 1-10eV and 10^{10} cm^{-3}, respectively. Plasma, such as can be obtained by a direct current glow discharge, can also be generated by a high frequency or a microwave discharge at low pressure [61]. In this plasma, the degree of ionization is typically only 10^{-4}, so the gas consists mostly of neutral but excited species. A characteristic of this plasma is the lack of thermal equilibrium.

1.2.5 Plasma Enhanced CVD

1.2.5.1 Reaction Mechanisms of Plasma Enhanced CVD

Plasma Enhanced CVD (PECVD) is essentially the extension and enhancement of the technique by using a plasma. The plasma makes it possible to decrease the reaction temperature. The reaction mechanisms involved in film formation in PECVD are not yet well understood, due to complexity of the reaction system, i.e., (1) the cold plasma is not in thermal equilibrium, (2) the gases used in the process are sometimes polyatomic molecules, and (3) the lack of basic data such as reaction cross sections [62]. Furthermore, gas phase reactions in the plasma and surface reactions on the substrate contribute roughly equally to the film formation process. Figure 1.4 shows the PECVD reaction process in film formation schematically. The gas molecules are excited, ionized or dissociated in the plasma mainly by electron impact. Thus excited molecules, atoms, radicals, molecular and/or atomic ions are produced and reach the substrate surface by diffusion. The flow of reaction gases and the configuration of electrodes and substrate holder cause a spatial distribution in the particle density. The particles which reach the surface migrate and find adsorption sites on the substrate. Finally, the atoms react with each other, resulting in film formation. Dissociation of molecules during adsorption may also occur. Bombardments of ions accelerated in the sheath affect surface reactions.

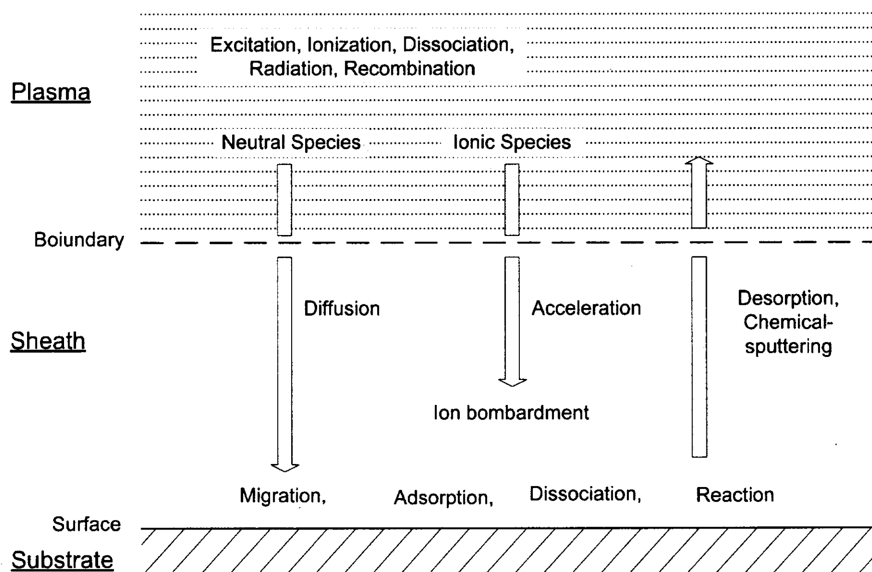

Figure 1.4 Schematic representation of the plasma enhanced CVD reaction process

In ordinary CVD processes, films are formed purely through thermochemical reactions at the substrate surface from gases in the ground state. The reaction progresses under nearly thermodynamic equilibrium. On the other hand, plasma-enhanced CVD is a film formation technique that causes excited species to react with each other. This makes it possible to deposit films at lower substrate temperatures than with thermal CVD, in which a high temperature is necessary to cross over the activation energy. In order to generate a discharge for producing cold plasma, low pressure is of course required. However, plasma enhanced CVD is a film formation process which includes chemical reactions. Therefore, higher particle densities of active species are required in order to get higher deposition rates. The pressure range in PECVD lies between 0.1 and 10 Torr. Mean-free paths of gas particles at this pressure range are as short as several hundred micrometers. The plasma is not dense. Most electron energies are probably in the range 0.5~10eV and the plasma density is 10^9~10^{12} cm^{-3}. The degree of ionization is less than 10^{-5}. The populations of free radicals are much greater than those of ions, and some

radicals have much longer lifetimes. Many reactions may occur among excited molecules and among ions and molecules, which complicates the reaction system further.

When the flow rate of reaction gas per unit electric power used for maintaining the plasma is relatively small, the deposition rate of the film is limited by the effective flow rate of the reaction gas. When the gas flow rate is high, the deposition rate is limited by externally supplied electric power. Although the deposition rate also changes with substrate temperature, the activation energy of the deposition rate is often very small. Occasionally, the apparent activation energy may even take a negative value when deposition rates are plotted directly against the inverse of the substrate temperature.

Even though reaction mechanisms are still not well understood, application to film formation has moved forward rapidly because of the technological demand from industries. In principle, by adopting as source gas, compounds which contain elements of the desired film and which have higher vapor pressure, any film can be deposited by PECVD. Hydrides and halogenides have been widely used. Organometallic compounds can also be used as source gases. These have already been applied to the semiconductor and electronic parts industries at the production levels.

1.2.5.2 Advantages of PECVD

In addition to inherited advantages from traditional CVD, plasma enhance CVD has several more advantages. The major advantage of PECVD is its lower temperature capability compared to that of thermally driven CVD [63, 64]. Applications of PECVD thin films and coatings range from electronics to optics and metallurgy. As explained above, the generation of reactive chemical species is done at gas temperatures near ambient due to the non-thermal equilibrium nature of the plasma. Therefore many high

temperature reactions can be made on temperature-sensitive substrates at low temperatures. Examples are aluminum, which would melt at the required LPCVD temperature, organic polymers which would otherwise degrade and outgas, or of metals and metal alloys which would undergo structural changes at higher temperatures such as austenitic steel. Dopants for semiconductors (boron, phosphorus) can readily diffuse between buried layers of the device if the temperature exceeds 800° C with damaging effects to the semiconductor properties. These doped materials can easily be coated without diffusion using PECVD.

Another advantage is that the effects of thermal expansion mismatch between substrate and coating and resulting stresses are reduced since the temperature of deposition remains low. The other advantages of the plasma process are that deposition rates are usually increased. With the low pressures used, the rate-controlling regime is surface reaction-limited kinetics leading to greater film uniformity. Low temperatures are more conducive to the growth of amorphous or very fine grained polycrystalline films which usually have superior properties. A number of deposition parameters necessary to alter film characteristics are available with PECVD for "tailoring" of these properties.

1.2.5.3 Limitation of PECVD

The limitations of PECVD are as follows. Deposits of pure materials are often difficult to achieve. Low temperatures during deposition in many cases results in incomplete desorption of byproducts and other gases, particularly hydrogen, resulting in unwanted inclusions and outgassing causing thermal instability. An example of this phenomenon is hydrogen given off from plasma nitride films that may cause damaging effects on the electronic properties of certain devices [65]. The complexity of reactions makes

stoichiometric compounds difficult to achieve, as in the case compounds such as carbides, nitrides, silicides or oxides. While usually detrimental to film properties and lowering its resistance to chemical etching and radiation, such alterations can be beneficial in certain applications, i.e. improved optoelectronic properties of amorphous silicon used in solar cells when hydrogen is present.

Other disadvantages include the creation of undesirable compressive stresses particularly at lower frequencies. In very thin films used in semiconductor applications, this may not be a problem. However, in thicker films typical of metallurgical applications, the compressive stresses could cause spalling and cracking of films.

Another disadvantage is potential damage to fragile substrates such as in VLSI and some III-V and H-VI semiconductor materials due to ion bombardment if the ion energy exceeds 20 eV. In addition, the plasma will react strongly to the surface as deposition takes place meaning that the deposition rate and many film properties will be a function of the plasma uniformity. More fully exposed areas of the substrate will therefore be affected by plasma interactions than less exposed, more sheltered regions. Reproducibility and deposition control is often inhibited by these complex gas phase and surface dynamics. Finally, the equipment is generally more expensive and complicated.

Overall the advantages of plasma enhance CVD are considerable and it is used in an increasing number of applications.

CHAPTER 2

EXPERIMENTAL PROCEDURE

2.1 Introduction

Tantalum thin films were prepared in PECVD reactor by adjusting deposition parameters including substrate temperature, pressure, gas composition and deposition time. The experiments yield a variety of coatings which were carefully subjected to physical and chemical analyses. These characterization procedures were aimed at standardizing the processing conditions to produce Tantalum coatings. The surface morphology and conformal coverage of the Ta coatings were investigated by using scanning electron microscope (SEM). Energy Dispersive X-ray analysis (EDX) was carried out for elemental analysis of the coatings. Atom force microscope (AFM) in contact mode was employed to examine the topography and surface roughness. X-ray diffraction (XRD) and X-ray Reflectivity (XRR) were performed in order to investigate the crystallographic structure, preferred orientation, and density of coatings. The compositional analysis has been carried out using a variety of diagnostic techniques including Auger electron spectroscopy (AES), X-ray photoelectron (XPS), and Nuclear Reaction analysis (NRA). The hardness and Young's Modulus of coatings was determine by nanoindentation. Resistance of coatings was measured by four-probe method. The following sections describe the experimental setup and brief theoretical aspects of characterization procedures.

2.2 PECVD Reactor

The plasma enhanced chemical vapor deposition (PECVD) reactor used in our experiments is schematically shown in Figure 2.1. It provides a maximum allowable substrate diameter of 15 cm. The reactor was connected to an Edwards QDP 80 vacuum station comprised of a Roots blower and a mechanical pump, which has a pump speed of 375 m^3/h and an ultimate base pressure of 5.3×10^{-3} Torr. The pressure of the reactor was measured at the reactor inlet using a vacuum gauge with a 0-10 Torr range and controlled by a throttle valve pressure controller to maintain constant pressure. An Advanced Energy RFX-600 with a frequency of 13.56 MHz was used as the source of radio frequency (RF) power. That source was connected to an RF matching network for impedance matching. The reactor was equipped with a load lock to prevent atmospheric contamination. The load lock was isolated from the reactor by a pneumatically operated slit valve and evacuated using a rotary pump. Sample transfer was achieved through a manual load lock arm. Mass flow controllers were used to measure and control the flow rate of process gasses. The H_2 reactant gas and the He dilute gas were delivered through a shower head located above the substrate. The shower head also served as the powered RF electrode. The $TaCl_5$ precursor with H_2 carrier gas was delivered through a gas dispersal ring. The cooling ring was attached with the gas dispersal ring to prevent the decomposition of the precursor inside the ring. N_2 was used as a coolant. The precursor was contained in the stainless steel bubbler. The precursor bubbler and delivery line were heated and controlled by a Watlow anafaze CLS 208 heat controller. The temperature of the delivery line was set higher than that of the container to avoid the condensation of the precursor within the line.

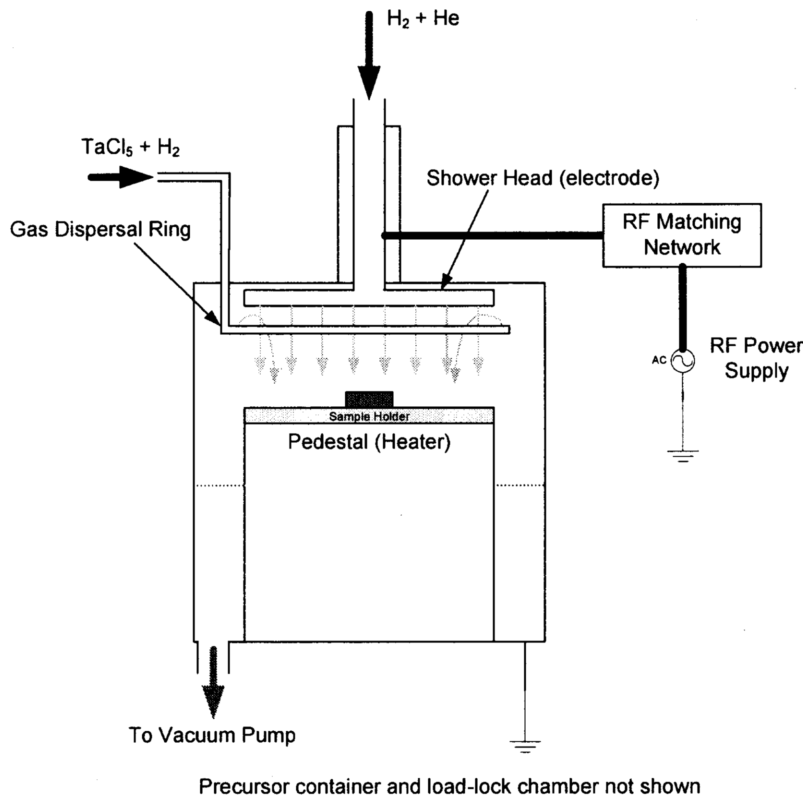

Figure 2.1 Schematic diagram of PECVD reactor.

2.3 Temperature Correction

The substrates were heated using a resistive heater. The temperature was measured and controlled by a heat controller with a type K thermocouple. The surface temperature of the substrate was observed using a "Thermodynamic Sensors 100 mm thermocouple wafer". Five thermocouples were attached on that wafer. The data was collected through a Pico TC-08 eight channel thermocouple data logger and monitored by a computer. The results are shown in Figure 2.2. The relationship between the temperatures at the surface and the setting point was established by fitting a curve through the following Eq. (2.1):

$$(\text{Surface Temperature}) = 0.6 \times (\text{Setting Temperature}) + 70 \tag{2.1}$$

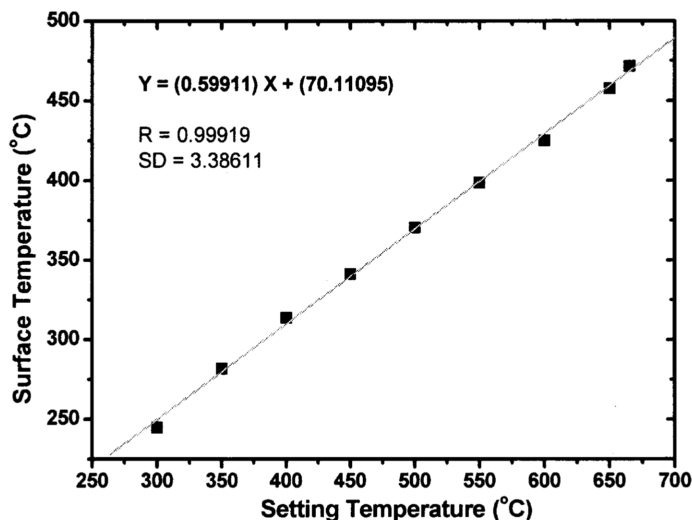

Figure 2.2 Correlation of measured surface temperatures to setting temperatures.

2.4 Determination of Precursors

2.4.1 Main Requirements

One of the most important starting points in CVD process development is the identification of an appropriate source precursor. The main requirements for a precursor are listed below: [64]

- Ease of decomposition: A candidate precursor should have relatively low dissociation energy of primary bonds, i.e., the bonds which link the target element to the rest of the compound. It is highly desired that the breakage of these primary bonds be achievable at deposition temperatures below 450 ℃. This criterion is dictated by the low processing temperature which is required for microelectronics applications to prevent interactions with previously deposited metallization layers or breakdown of other materials (e.g low k polymeric dielectrics).

- Sufficient Vapor Pressure: To achieve reasonably high deposition rates, the vapor pressure of a precursor should be high enough to allow the delivery of a large precursor flux to the reaction zone as needed.
- Reasonable thermal stability: A candidate precursor should remain stable during storage, transport and handling, as well as at its vaporization temperature to prevent its premature decomposition prior to reaching the CVD reaction zone.
- Low cost: The selected precursor should be reasonably inexpensive to produce with a very high degree of purity.

2.4.2 Candidate Precursors for CVD Tantalum

a) Metalorganic precursors

There are three metalorganic CVD (MOCVD) processed reported for growth of Tantalum films. The carbonyl-based process,

$$Ta(CO)_5 + H_2 \rightarrow Ta \qquad \textbf{(2.2)}$$

produced coatings on copper between 725K to 875K. [66], but the films contained 5-10% impurities. However, these compounds leave carbon impurities in the resulting films. The presence of impurities such as carbon and oxygen in the films results in lower performance. Two other processes [4], from the patent literature, were thermal decompositions

$$Ta(\eta^6 - C_6H_6)_2 \rightarrow Ta \qquad \textbf{(2.3)}$$

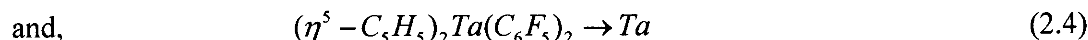

and, $$(\eta^5 - C_5H_5)_2Ta(C_6F_5)_2 \rightarrow Ta \qquad (2.4)$$

Low temperatures depositions were declaimed, but details are sketchy and material purity was not addressed.

As we have seen from current tantalum CVD, coatings based on the alkoxide precursors have been studied extensively. A look in the literature indicates there may already be some other promising metalorganic compounds for tantalum CVD studies. However, although the MOCVD routes are the ones that produce low-temperature chemistries, its disadvantage also is obvious.

Perhaps the most compelling reason not to look towards MOCVD is the precursors themselves. They could be viewed as "designer" precursors and not everyone has the luxury of having an organometallic chemist on-hand. This is, basically, a staffing decision. Second, the air sensitivity of MOCVD precursors is a potential problem. These precursors require special handing that may not be compatible with one's processing. Careful design of the processing will certainly address this. Lastly, if one decides to purchase the organometallic precursor, there is always the question of "what is in the bottle?" The exact composition, and many other properties, is highly dependent on the synthetic route used to prepare the compound. A change by the supplier, is synthetic route, could affect many months or years of effort. Additional problems with Ta are that all resulting films have relatively high concentrations of oxygen and carbon impurities and require the use of carrier gas. Furthermore, MOCVD has not shown a viable pathway to tantalum metal.

b) Halide precursors

In order to prepare carbon-free films, an alternative approach was examined using Tantalum halides as starting materials. The tantalum halide precursor is tantalum fluoride (TaF), tantalum chloride (TaCl) or tantalum bromide (TaBr), preferably tantalum pentafluoride (TaF_5), tantalum pentachloride ($TaCl_5$) or tantalum pentabromide ($TaBr_5$).

The use of tantalum halide precursors such as TaF_5, $TaCl_5$, and $TaBr_5$ has been reported in the synthesis of CVD Ta coatings[3, 4, 33, 67-69]. Now, Tantalum halides are the most widely used precursors. For preventing the contamination from halogen and improving the purity of the film, we can add a reducing agent during the deposition, like H_2. The heat of formation of these halide precursors increase in the following order: $TaBr_5 < TaCl_5 < TaF_5$ (Table 2.1) [69]. At a given temperature, the vapor pressure of these halides consequently follows a reverse order: $TaBr_5 < TaCl_5 < TaF_5$ (Figure 2.3) [33, 69]. $TaCl_5$ has a medium value of the heat of formation and vapor pressure. Furthermore, Joseph Hillman et.al. got the tantalum films with halogen content less than 0.5% by CVD using different halide precursors. Especially, they didn't detected halogen exist when they use $TaBr_5$ as precursor [30]. However, compared the best step coverage, moderate deposition rate, and minor halogen content in Table2.2 [30], $TaCl_5$ was chosen as the precursor in our experiment.

Further reduction in processing temperature could be achieved by employing low power hydrogen plasma, given the critical role that atomic or ionic hydrogen plays in the $TaCl_5$ reduction process. The overall chemical reaction involved in CVD Ta using tantalum pentachloride shows as follows:

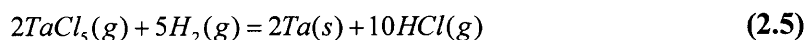

$$2TaCl_5(g) + 5H_2(g) = 2Ta(s) + 10HCl(g) \quad \mathbf{(2.5)}$$

Furthermore, the halide precursor and its effluent (e.g., HF, HCl, and HBr) are non-toxic, non-pyrophoric, and non-explosive. They are not listed by EPA, IARC, NTP, OSHA, or ACGIH as a carcinogen or potential carcinogen. Furthermore, both the precursor and its effluent do not contain ozone-depleting chemicals.

Table 2.1 The properties of tantalum halide precursors

Precursors	Melting point (°C)	Boiling point (°C)	Heat of Formation (ΔHf, kcal/mol)
TaF_5	97	230	-455
$TaCl_5$	216	242	-205
$TaBr_5$	265	349	-143

Table 2.2 Summary of PECVD Ta film properties obtained for each of the listed halide precursors

	TaF_5	$TaCl_5$	$TaBr_5$
Deposition temperature (°C)	350	350	350
Halogen Impurity (XPS)	0.50%	0.10%	Not detected
Step Coverage	70%	90%	75%
Deposition Rate (Å/min)	145	35	10
Surface Roughness (nm)	0.5	0.6	1.2

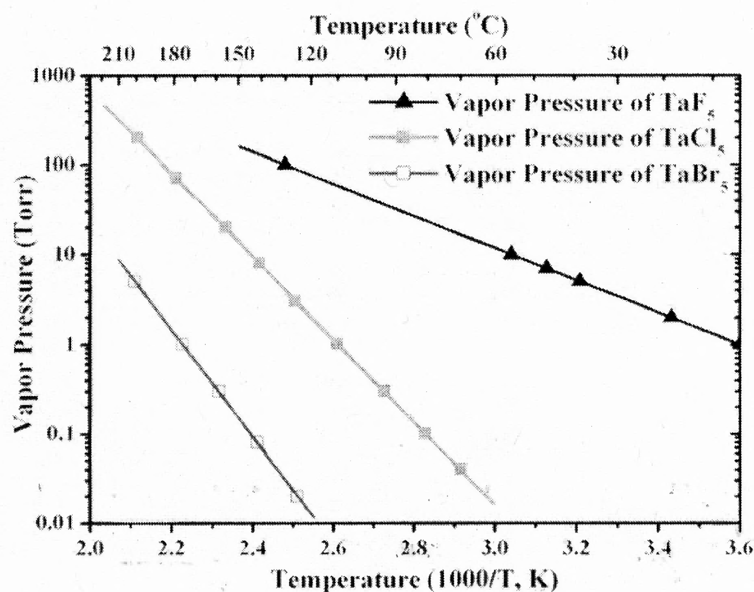

Figure 2.3 Vapor pressure of tantalum halide precursors versus temperature.

2.5 Deposition Procedure

2.5.1 Precursor Flow Rate Calibration

From the above discussed, the vapor pressure depends on the precursor temperature. The higher vapor pressure has more potential to increase the growth rate of Tantalum coatings. However, the higher precursor temperature can cause safety issues. Therefore, it is very important to find an efficient precursor temperature.

The flow rate of the precursor is generally expressed in units of sccm, i.e., standard cubic centimeter per minute. This is the volume that would be occupied by the precursor, which is measured at standard temperature and pressure, as result of flow for one minute. In order to verify the rate of flow, the precursor was delivered into the CVD reaction chamber at a known initial pressure and temperature, using the standard flow controller which was set to control at desired flow. The flow rate of H_2 carrier gas is set to 10 sccm.

The sublimator of $TaCl_5$ contains 50 g $TaCl_5$ powder. The mass of the container is measured before and after several runs in order to define the mole number of $TaCl_5$ evaporated per hour. One mole of an ideal gas will occupy a volume of 22.4 liters at STP (Standard Temperature and Pressure, 0°C and one atmosphere pressure). The state of precursor $TaCl_5$ was assumed to keep at STP. Therefore, the evaporation rate of precursor $TaCl_5$ can be readily equivalent to flow rate by unit sccm by the following procedure:

$$s = n \times \frac{22.4 \times 10^3}{60} = \frac{m}{M} \times \frac{22.4 \times 10^3}{60} = \frac{m}{358.21} \times \frac{22.4 \times 10^3}{60} = 1.0422m \qquad \textbf{(2.6)}$$

where s expresses flow rate, n expresses number of moles, m expresses evaporation rate, and M expresses the Molecule mass of $TaCl_5$.

Table 2.3 shows the evaporation rate and calculation results of flow rate under different precursor temperature.

Table 2.3 The evaporation rate of tantalum chloride

Measurement Number	#1	#2	#3	#4	#5	#6
Precursor Temperature (°C)	135	135	110	110	105	105
Evaporation Rate (g/hr)	1.73	1.93	1.5	1.28	0.83	0.77
Flow Rate (sccm)	1.8	2.01	1.56	1.33	0.87	0.80

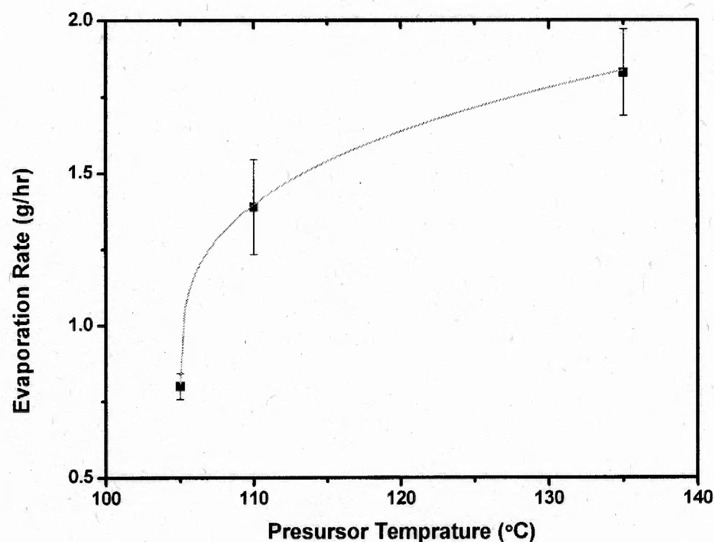

Figure 2.4 $TaCl_5$ evaporation rate v.s. precursor temperature

Figure 2.4 shows the evaporation rate of precursor versus precursor temperature. It dictates that the evaporation rate drops very quickly when the precursor temperature is lower than about 107 °C.

2.5.2 Preparation of Samples

The substrates used for the CVD Ta deposition consisted of AISI 4340 steel coupons (non-polished and polished) and pieces from silicon wafers (V-groove pattern and non-pattern) as a reference.

Table 2.4 Polishing Procedure of Steel substrate

Surface	Lubricant Extender	Abrasive Type/Size	Speed (RPM)	Time (min:sec)
CARBIMET®	Water	SiC 240 grit/51.8μm	700	Until plane
CARBIMET®	Water	SiC 320 grit/34.3μm	400	All scratch along same direction
CARBIMET®	Water	SiC 400 grit/22.1μm	400	All scratch along same direction
CARBIMET®	Water	SiC 600 grit/14.5μm	400	All scratch along same direction
TRIDENT Polishing Cloth 8"	Water	METADI Diamond Suspensions - 9μm	150~200	All scratch along same direction
TRIDENT Polishing Cloth 8"	Water	METADI Diamond Suspensions - 3μm	150~200	All scratch along same direction
TRIDENT Polishing Cloth 8"	Water	METADI Diamond Suspensions - 1μm	150~200	10:00
TRIDENT Polishing Cloth 8"	Water	METADI Diamond Suspensions – 0.25μm	120~150	5:00

The polishing procedure of steel coupons is shown in Table 2.4. It involves a series of silicon carbide sandpaper from 320 to 600grit and a special polishing pad requiring polycrystalline diamond suspensions. TRIDENT Polishing Cloth (8") has to use with different polycrystalline diamond suspensions. The particle size of a polycrystalline

diamond suspension was down to 0.25μm in the last step. After final polished, the steel coupons were received an ultrasonic cleaning process consisting of a 10-min immersion in baths of acetone and ethanol.

Before loading the substrates into the reactor, all substrates were cleaned in an ultrasonic bath with isopropanol, acetone and methanol sequentially, rinsed with DI water, and dried with clean nitrogen.

2.5.3 Film Deposition

After loading the substrates into the reactor, in-situ cleaning with excited molecular and atomic hydrogen produced by the RF plasma for 5~20 minutes was conducted to remove native oxide and organic contaminants. In this study, $TaCl_5$ was used with 10sccm H_2 carrier gas while the gas flow rate of reactant H_2 and dilute He gas was 500sccm and 150sccm, respectively. The precursor temperature was in the range of 100-135 °C. The deposition temperature and the reactor pressure were varied in the range of 370~400 °C and 0.7~1 Torr, respectively. The RF power used to produce the plasma was varied in the range of 50~100 W.

2.6 Characterization Techniques

The CVD Ta coatings deposited on steel coupons (AISI 4340) and Si wafers have been characterized in terms of their structural, morphological, and step coverage properties to assess the viability of the CVD Ta process. Prior to characterization, all the coated samples were ultrasonically cleaned in acetone followed by methanol. For the cross sectional analyses of the Ta coatings, the specimens were cross-sectioned and mechanically polished by following the same process as steel coupons. The only

improvement is that the particle size of a polycrystalline diamond suspension was down to 0.05μm in the last step.

2.6.1 Scanning Electron Microscopy (SEM)

The surface morphology and conformal coverage of the Ta coatings were investigated by using FE-SEM (LEO 1530 VP) on the surface and cross-sections of coatings deposited on steel coupons as well as silicon wafers.

The SEM is designed for direct studying of the surfaces of solid objects. The SEM allows a greater depth of focus than the optical microscope. For this reason the SEM can produce an image that is a good representation of the three-dimensional sample. Therefore, it can be useful to gain topographic images and microstructural analysis. Also, it can do elemental analysis if equipped with appropriate detector (EDAX, WDX). The range of magnification is about 10 - 50,000 times. Since the SEM uses electrons to produce an image, most conventional SEM's require that the samples be electrically conductive or coated with thin conductive layer and compatible with vacuum environment.

During SEM inspection, a beam of electrons is focused on a spot volume of the specimen, resulting in the transfer of energy to the spot. These bombarding electrons, also referred to as primary electrons, dislodge electrons from the specimen itself. The dislodged electrons, also known as secondary electrons, are attracted and collected by a positively biased grid or detector, and then translated into a signal. By scanning with an electron beam that has been generated and focused by the operation of the microscope, an image is formed in much the same way as a TV. The energy of the primary electrons determines the quantity of secondary electrons collected during inspection.

The electrons incident beam can generate a lot of signals. While all these signals are present in the SEM, not all of them are detected and used for information. The signals most commonly used are the Secondary Electrons, the Backscattered Electrons and X-rays. Aside from secondary electrons, the primary electron beam results in the emission of backscattered (or reflected) electrons from the specimen. Backscattered electrons possess more energy than secondary electrons, and have a definite direction. All emissions above 50 eV are considered to be backscattered electrons. Because they are moving so fast, they travel in straight lines. These electrons are called backscattered electrons because they come back out of the sample as shown in Figure 2.5(a). In order to form an image with BSE (backscattered electrons), a detector is placed in their path. When they hit the detector, a signal is produced which is used to form the TV image. All the elements have different sized nuclei. As the size of the atom nucleus increases, the number of BSE increases. Thus, BSE can be used to get an image that showed the different elements present in a sample. Backscattered electron imaging is useful in distinguishing one material from another, since the yield of the collected backscattered electrons increases monotonically with the specimen's atomic number. Backscatter imaging can distinguish elements with atomic number differences of at least 3, i.e., materials with atomic number differences of at least 3 would appear with good contrast on the image. Figure 2.5(b) shows the yield of secondary electrons and back scattered electrons relates with atomic number versus the incident electron energy. It indicates that the number of secondary electrons produced is relatively insensitive to atomic number of the atoms in the material. The number of backscattered electrons, however, is sensitive to atomic number of the material.

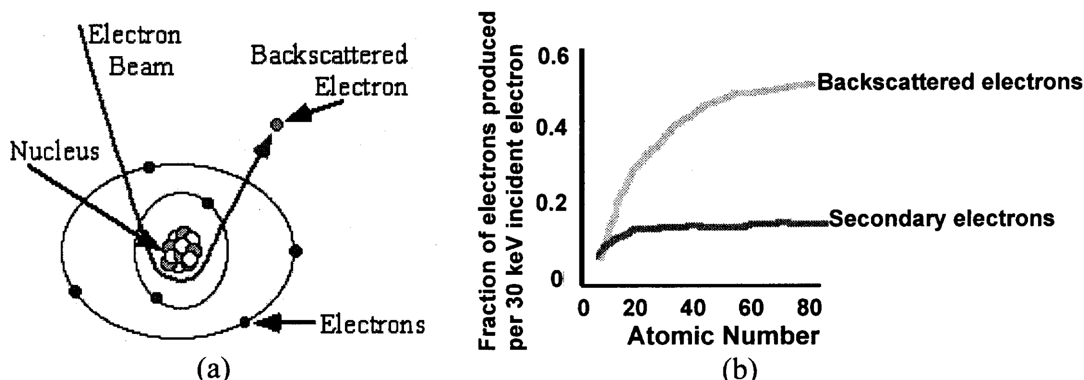

Figure 2.5 (a) The formation of backscattered electrons, (b) The yield of secondary electrons and back scattered electrons relates with atomic number versus the incident electron energy

2.6.2 Energy-Dispersive X-Ray (EDX)

Energy Dispersive X-ray analysis (EDX) is sometimes referred to also as EDS or EDAX analysis. It is a technique used for identifying the elemental composition of the specimen, or an area of interest thereof. The EDX analysis system works as an integrated feature of a SEM, and can not operate on its own without the latter. EDX analysis is useful in identifying materials and contaminants, as well as estimating their relative concentrations on the surface of the specimen. EDX (Oxford INCA Energy 400) was carried out for elemental analysis of the coatings in our experimental.

During EDX Analysis, the specimen is bombarded with an electron beam inside the SEM. The bombarding electrons collide with the specimen atoms' own electrons, knocking some of them off in the process. A position vacated by an ejected inner shell electron is eventually occupied by a higher-energy electron from an outer shell. The transferring outer electron must give up some of its energy by emitting an X-ray. The amount of energy released by the transferring electron depends on which shell it is transferring from, as well as which shell it is transferring to (Figure 2.6). Furthermore, the

atom of every element releases X-rays with unique amounts of energy during the transferring process. Thus, by measuring the amounts of energy present in the X-rays being released by a specimen during electron beam bombardment, the identity of the atom from which the X-ray was emitted can be established. The EDX spectrum is just a plot of how frequently an X-ray is received for each energy level. An EDX spectrum normally displays peaks corresponding to the energy levels for which the most X-rays had been received. Each of these peaks is unique to an atom, and therefore corresponds to a single element. The higher a peak in a spectrum, the more concentrated the element is in the specimen. An EDX spectrum plot not only identifies the element corresponding to each of its peaks, but the type of X-ray to which it corresponds as well. For example, a peak corresponding to the amount of energy possessed by X-rays emitted by an electron in the L-shell going down to the K-shell is identified as a K-α peak.

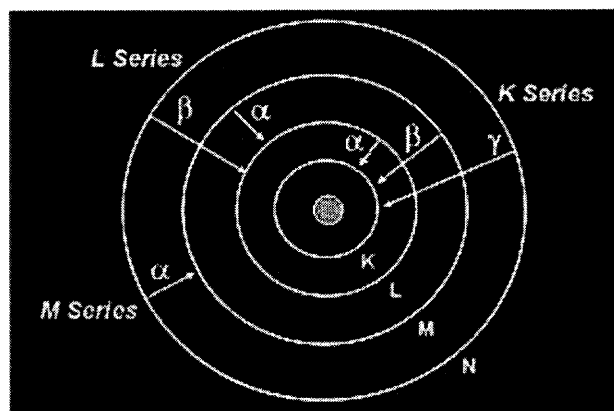

Figure 2.6 Elements in an EDX spectrum are identified based on the energy level.

2.6.3 X-Ray Diffraction (XRD)

X-ray diffraction spectra were studied to investigate the crystallographic structure of the deposited coatings. XRD was performed using a Philips X'Pert MRD X-ray diffractometer (Bragg-Brentano θ:θ) with Cu Kα radiation operated at 45 kV and 40 mA.

Each crystalline solid has its unique characteristic X-ray powder pattern which may be used as a "fingerprint" for its identification. Once the material has been identified, X-ray crystallography may be used to determine its structure, i.e. how the atoms pack together in the crystalline state and what the interatomic distance and angle are etc. We can determine the size and the shape of the unit cell for any compound most easily using the diffraction of x-rays.

X-rays primarily interact with electrons in atoms. When x-ray photons collide with electrons, some photons from the incident beam will be deflected away from the direction where they original travel, much like billiard balls bouncing off one anther. If the wavelength of these scattered x-rays did not change (meaning that x-ray photons did not lose any energy), the process is called elastic scattering (Thompson Scattering) in that only momentum has been transferred in the scattering process. These are the x-rays that we measure in diffraction experiments, as the scattered x-rays carry information about the electron distribution in materials. On the other hand, In the inelastic scattering process (Compton Scattering), x-rays transfer some of their energy to the electrons and the scattered x-rays will have different wavelength than the incident x-rays. Diffracted waves from different atoms can interfere with each other and the resultant intensity distribution is strongly modulated by this interaction. If the atoms are arranged in a periodic fashion, as in crystals, the diffracted waves will consist of sharp interference maxima (peaks) with the same symmetry as in the distribution of atoms. Measuring the diffraction pattern therefore allows us to deduce the distribution of atoms in a material. The peaks in a x-ray diffraction pattern are directly related to the atomic distances.

Figure 2.7 shows the illustration for Bragg's Law. The atoms, represented as yellow spheres in the graph, can be viewed as forming different sets of planes in the crystal. For a given set of lattice plane with an inter-plane distance of d, the condition for a diffraction (peak) to occur can be simply written as

$$2d\sin\theta = n\lambda \tag{2.7}$$

which is known as the Bragg's law. In the equation, λ is the wavelength of the x-ray, θ the scattering angle, and n an integer representing the order of the diffraction peak. The Bragg's Law is one of most important laws used for interpreting x-ray diffraction data.

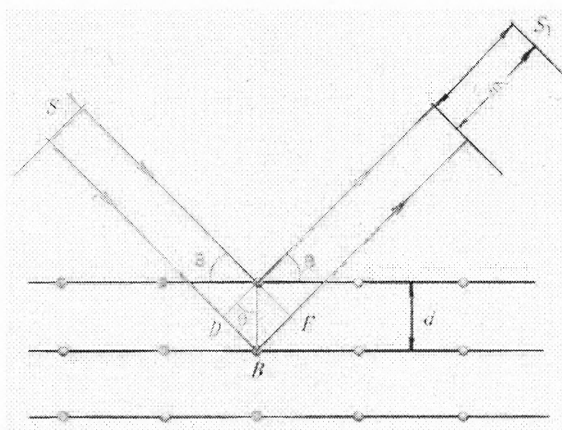

Figure 2.7 The illustration for Bragg's Law

2.6.4 Atomic Force Microscopy (AFM)

Atomic Force Microscopy and Scanning Probe Microscopy (AFM/SPM) provide topographic information down to the Angstrom level. AFM (Nanoscope IIIA Multimode scanning probe microscope, Digital Instruments) in contact mode was employed to examine the topography and surface roughness of the CVD Ta coatings. Additional properties of the sample, such as thermal and electrical conductivity, magnetic and electric field strength, and sample compliance can simultaneously be obtained using a

specialty probe. Many applications require little or no sample preparation. Atomic force microscopy (AFM) is a powerful technique for investigating surfaces. In the imaging mode, a sharp tip is scanned over a surface and some surface parameter monitored. Traditionally, the deflection of a cantilever holding the tip is monitored by a photodiode. When the tip scans across the surface, it will interact with the latter, and deflect according to the interaction: if there is an attractive interaction between the surface and the tip, the tip will be deflected towards the surface, whereas deflection away from the surface will occur in the case of a repulsive tip-surface interaction. In the most frequently used AFM technique, the deflection is kept constant through a feed-back loop, and the z-movement of the stage needed for accomplishing this monitored. From this, one essentially obtains an interaction map, which under certain conditions may be translatable to a topographic map.

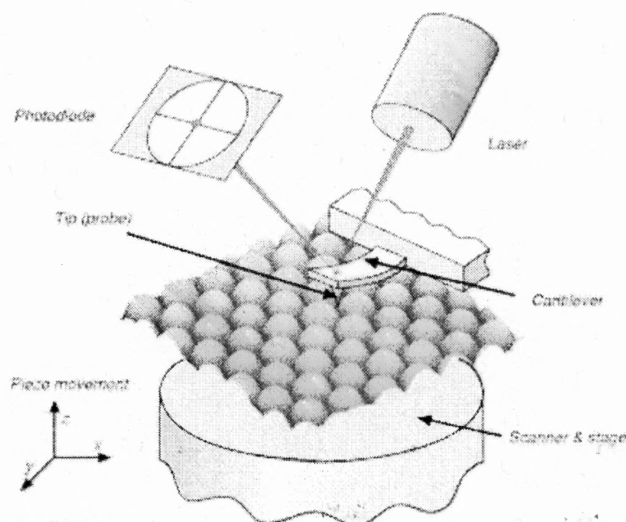

Figure 2.8 Schematic illustration of AFM

Many AFM modes have appeared for special purpose while the technique of AFM is becoming mature. The three commonly used techniques were specified here (Figure 2.9):

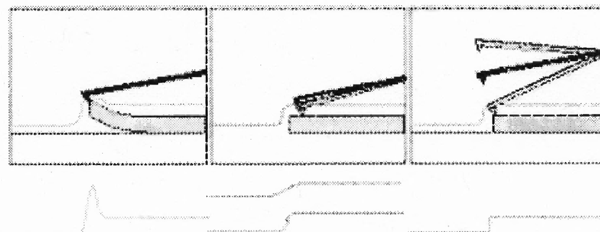

Figure 2.9 The Common AFM Modes: Contact Mode (left), Non-contact Mode (middle) and Tapping Mode (right).

The first and foremost mode of operation, contact mode is widely used. As the tip is raster-scanned across the surface, it is deflected as it moves over the surface corrugation. In constant force mode, the tip is constantly adjusted to maintain a constant deflection, and therefore constant height above the surface. It is this adjustment that is displayed as data. However, the ability to track the surface in this manner is limited by the feedback circuit. Sometimes the tip is allowed to scan without this adjustment, and one measures only the deflection. This is useful for small, high-speed atomic resolution scans, and is known as variable-deflection mode. Because the tip is in hard contact with the surface, the stiffness of the lever needs to be less that the effective spring constant holding atoms together, which is on the order of 1 - 10 nN/nm. Most contact mode levers have a spring constant of < 1N/m.

Noncontact mode belongs to a family of AC modes, which refers to the use of an oscillating cantilever. A stiff cantilever is oscillated in the attractive regime, meaning that the tip is quite close to the sample, but not touching it (hence, "noncontact"). The forces between the tip and sample are quite low, on the order of pN (10 - 12 N). The detection

scheme is based on measuring changes to the resonant frequency or amplitude of the cantilever.

Commonly referred to as "tapping mode", it is also referred to as intermittent-contact or the more general term Dynamic Force Mode (DFM). A stiff cantilever is oscillated closer to the sample than in noncontact mode. Part of the oscillation extends into the repulsive regime, so the tip intermittently touches or "taps" the surface. Very stiff cantilevers are typically used, as tips can get "stuck" in the water contamination layer. The advantage of tapping the surface is improved lateral resolution on soft samples. Lateral forces such as drag, common in contact mode, are virtually eliminated. For poorly adsorbed specimens on a substrate surface the advantage is clearly seen.

2.6.5 X-Ray Reflectivity (XRR)

Glancing incidence x-ray reflectivity (XRR) measurements can determine the thickness, roughness, and density of the film. This technique does not require crystalline film and works even with amorphous materials. To measure the density of the CVD Ta coatings, XRR (PANalytical XPERT-PRO diffractometer) was utilized with Cu Kα radiation operating at 45 kV and 40 mA.

When X-rays strike a surface at glancing incidence they can reflect off the surface. However, if the surface is rough or covered by a film, then the X-ray reflectivity of a surface can change. XRR takes advantage of this effect by measuring the intensity of X-rays reflected from a surface as a function of angle. Thin films on a surface can give rise to oscillations of the X-ray intensity with angle. XRR can provide information on the thickness, roughness and density of thin films on a surface. XRR is a non-destructive, non-contact method to measure film thickness, interfacial roughness and density of films

ranging from 20 Å to 1 mm total thickness. Films can be single or multilayer structures, and the thickness of individual layers can be determined in minutes, with no optical constant corrections required. The films can be epitaxial, polycrystalline or amorphous. The thickness of the film is measured from the periodicity of fringes, the density from the angle at which the intensity begins to drop and the roughness from the damping of the thickness fringes and rate of intensity decrease with angle. These are not affected by the crystallinity of the film.

The complex refractive index in the x-ray region is slightly less than 1 and is given by

$$\tilde{n} = 1 - \delta + i\beta \tag{2.8}$$

where δ and β represent the dispersion and absorption, respectively. For frequencies far greater than the resonance frequencies, #₀, of the atom δ can be given by the expression

$$\delta = \frac{e^2 n_e}{2\varepsilon_0 m(2\pi c)^2}\lambda^2 = \frac{r_0\lambda^2}{2\pi}\cdot n_e \tag{2.9}$$

where r_0 is the Bohr atomic radius and n_e is the electron density. The electron density is given by $n_e = Z \cdot n_{Atom}$ where Z is the number of electrons per atom. For a more precise expression of δ, Z is usually replaced with the a complex atom form factor $f^{\sim} = f_0 + f' + if'' = Z + f' + if''$. The term $f' + if''$ is due to dispersion and absorption and describes the x-ray absorption edge. It follows that

$$\delta = \frac{r_0\lambda^2}{2\pi}\cdot(Z + f')\cdot n_{Atom} \tag{2.10}$$

and

$$\beta = \frac{r_0\lambda^2}{2\pi}\cdot f''\cdot n_{Atom} \tag{2.11}$$

The magnitudes of δ and β are of the order of 10^{-5} and 10^{-6}, respectively. Since the atomic concentration is given as

$$n_{Atom} = \frac{N_A}{A} \cdot \rho \tag{2.12}$$

It is apparent that, the density of the material can be determined from the values of δ and β. Here N_A is the Avogadros number and A the atomic weight. The density of a compound material of known stoichiometry can also be determined from δ and β with slight modifications in the formula.

We illustrate the determination of the different quantities obtained from XRR measurement with an example of a single film on a substrate. For qualitative discussion, it is adequate to consider an absorption free film i.e. $\beta = 0$ but it should be noted that β cannot be ignored in the simulation of XRR measurements. We consider reflection at an interface between air, $n_{air} = 1$ and another material, $n_1 = 1 - \delta$. For incident angles below a critical angle, θc, ($\theta < \theta c$), total reflection occurs. By applying Snell's law and small angle approximations, the critical angle, θc can be expressed as

$$\begin{aligned} 1-\delta = \cos\theta_C \approx 1-\frac{\theta_C^2}{2} \\ \Leftrightarrow \theta_C \approx \sqrt{2\delta} = \sqrt{\frac{r_0 \cdot \lambda^2}{\pi} N_A \frac{(Z+f')^2}{A} \cdot \rho} \end{aligned} \tag{2.13}$$

2.6.6 X-Ray Photoelectron Spectroscopy (XPS)

In order to evaluate the compositional chemistry of the coatings, XPS (ThermoElectron VG Scientific ThetaProbe) was utilized with an X-ray source of monochromated Al Kα (1486.6 eV) operating at 15 kV and 100 W. Survey and profile pass energies used in XPS analysis were 300 and 100 eV, respectively. During the XPS measurements, Ar ion etching was employed for depth profiling with an etching rate of 20 Å/min.

The principle of the XPS is the emission of electrons from atoms by absorption of photons. X-ray excitation is ised to induce emission of electrons from the core levels. An energy diagram is shown in Figure 2.10. The binding energy of the electron is dependent on the atomic charge distribution. For one configuration the binding energies of the orbital attain given values. The binding energy, E_B, of an electron level can be determined by measurement of the kinetic energy, E_{kin}, of the photoelectron. The energy diagram in Figure 2.10 gives the relationship:

$$E_B = h\nu - E_{kin} - \phi \quad \textbf{(2.14)}$$

Where $h\nu$ is the energy of the characteristic X-ray, h is Planck's constant, ν is the frequency, and ϕ is the work function of the spectrometer. In principle, the work function should be the work function of the analysed samples, but the photoelectron passes an electric field created by the difference between the work functions of the spectrometer and the sample so that ϕ becomes constant.

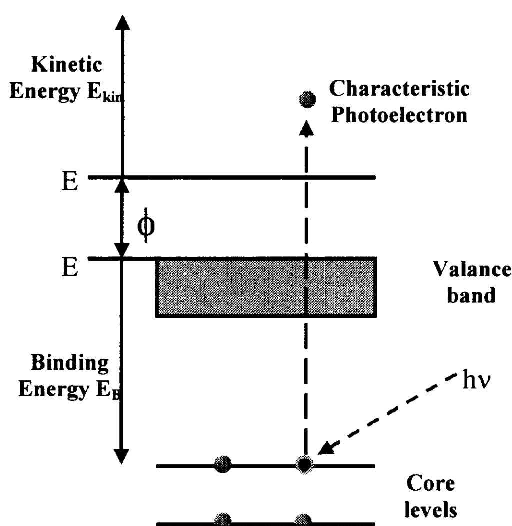

Figure 2.10 Schematic illustration of photoelectron emission.

2.6.7 Auger Electron Spectroscopy (AES)

The operation condition of AES (Perkin-Elmer Physical Electronic Model 660 Scanning Auger Microprobe) included achieving a base pressure of < 1.0×10^{-9} Torr, utilizing a primary beam energy of 10 keV, and a current of 1.0 μA. To establish a depth profile of the coatings during AES analysis, Ar ion etching was performed with an etching rate of 92 Å/min.

AES can be used to qualitative and quantitative elemental composition analysis. It is possible to detect all elements in the periodic table with the exception of hydrogen and helium. In certain cases, it is even possible to obtain information on the chemical bonding of the surface atoms. Elemental maps can be acquired with Scanning Auger. It has high surface sensitivity, approximately 1nm. The depth profiling can be obtained using Ar ion sputtering.

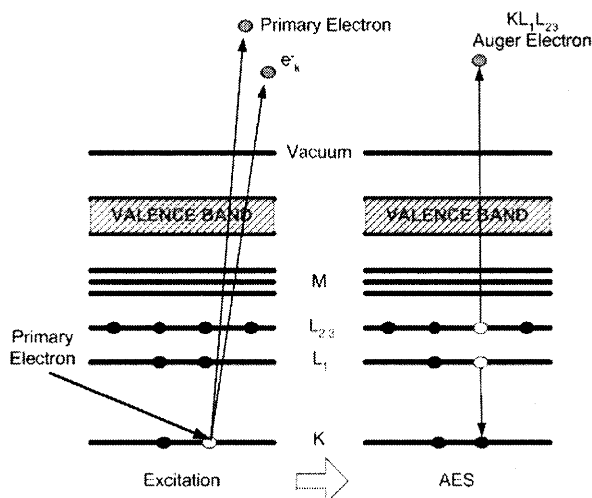

Figure 2.11 Schematic illustration of Auger Electron emission.

When a beam of electrons interacts with atoms in a material, core level electrons can be ejected if the energy of the incident electrons is larger than the ionization

threshold. Relaxation of the ionized atom can occur by filling the core vacancy with an electron from an outer shell. The relaxation energy is then dissipated in either of two ways. It can be given to a second electron, an Auger electron, which is emitted from the atom as demonstrated in Figure 2.11, or it can appear as a characteristic X-ray photon.

2.6.8 Nuclear Reaction Analysis (NRA)

NRA using $^{1}H(^{15}N, \alpha\gamma)^{12}C$ resonance nuclear reaction method was performed to determine hydrogen incorporation in the Ta coatings. Each sample was loaded in the analysis chamber at room temperature and bombarded with ~20 nA of ^{15}N ion.

A commonly used reaction to profile hydrogen is

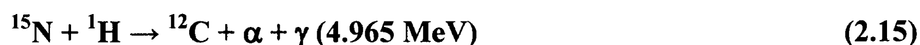

$$^{15}N + {}^{1}H \rightarrow {}^{12}C + \alpha + \gamma \text{ (4.965 MeV)} \qquad (2.15)$$

with a resonance at 6.385 MeV ion energy. The energetic emitted γ ray is characteristic of the reaction and the number than are detected at any incident energy is proportional to the concentration at the respective depth of hydrogen in the sample. The H concentration profile is then obtained by scanning the ^{15}N incident beam energy.

CHAPTER 3

THERMODYNAMIC CALCULATIONS

The Thermodynamic study of the phase equilibria during the CVD process provides a basic understanding of the process prior to designing suitable deposition experiments and provides a useful guideline for the selection of processing conditions. Prior to the CVD deposition, it is essential to determine the feasibility of the CVD reaction, the nature and amount of the solid and gaseous species present in the system. These can be determined from the calculation of the thermodynamic equilibrium (i.e. the equilibrium partial pressures of the system species) at a given set of processing conditions such as deposition temperature, pressure and reactant concentration [60]. Thermodynamic simulations are based on the minimization of the Gibbs free energy. They have been performed using the computer program HSC Chemistry 3.0 developed by ESM software which also supply the thermodynamic database.

3.1 Reaction Feasibility

The feasibility of a CVD reaction can be determined by calculating the Gibbs free energy ΔG_r of the reaction for the given temperature and pressure. In order to calculate the Gibbs free energy of reaction, ΔG_r, we have to first determine the free energy of formation, ΔG_f, of the individual species of the reactants and the products, using the following Eq. (3.1) at a temperature T, and followed by Eq. (3.2), where ΔH^0_f and S^0 are standard enthalpy of formation and entropy at 298 K, respectively, and C_p is heat capacity.

$$\Delta G_f(T) = \Delta H_f^0(298) + \int_{298}^{T} C_P dT - TS^0(298) - \int_{298}^{T} (C_P / T) dT \qquad \textbf{(3.1)}$$

$$\Delta G_r = \Delta G_f \text{ (products)} - \Delta G_f \text{ (rectants)} \quad (3.2)$$

The thermochemical data for many species can be found in the literature such as JANAF tables [70] and CRC Handbook of Chemical data. A reaction will occur when ΔG_r value is negative, whereas a positive ΔG_r means that the reaction will not occur. Under certain circumstances where there are several possible reactions, which are all, thermodynamically feasible, the reaction with the most negative ΔG_r value will dominate because it has the most stable reaction products. The equilibrium constant, K can be determined from Eq. (3.3), where R is the gas constant and T is the deposition temperature. Once K is known, the activity (or partial pressure) of gaseous species and products can be calculated using the law of mass action Eq. (3.4).

$$K = \exp(\Delta G_r / RT) \quad (3.3)$$

$$K_p = \frac{\text{multiple of product activites (or partial pressure)}}{\text{multiple of gaseous rectant activities (or partial pressure)}} \quad (3.4)$$

3.2 Thermodynamic Calculations

The construction of a CVD phase diagram at constant temperatures and pressures can be achieved either by (1) the equilibrium constant or (2) the minimisation of Gibbs free energy methods. The equilibrium constant method which requires information of all reactive species and reactions involves the use of non-linear equations. The minimisation of Gibbs free energy method involves the use of linear equations and it is independent of the reaction pathways. Therefore, the latter method is generally more suitable especially for complex chemical systems.

The thermochemical approach allows an assessment of the gaseous and condensed phase composition at equilibrium, and the definition of a suitable experimental set of parameters such as deposition temperature, total pressure, and partial pressures for the process.

The use of tantalum halide precursors such as TaF_5, $TaCl_5$, and $TaBr_5$ has been reported in the synthesis of CVD Ta coatings. The melting and boiling points of these precursors are found to increase in the following order: $TaF_5 < TaCl_5 < TaBr_5$. At a given temperature, the vapor pressure of these halides consequently follows a reverse order: $TaBr_5 < TaCl_5 < TaF_5$. The overall chemical reaction involved in CVD Ta using tantalum halides is as follows:

$$TaX_5(g) + 2.5H_2(g) = Ta(s) + 5HX(g), \quad \text{where } X \text{ represents } F,\ Cl, \text{ or } Br \qquad \textbf{(3.5)}$$

Thermodynamic calculations are carried out for a temperature range from room temperature to 1100 °C. They show that the aforementioned reaction is endothermic (Figure 3.1a). The enthalpy change for the reaction with TaF_5 is much greater than reactions involving $TaCl_5$ and $TaBr_5$ indicating that a CVD Ta process based on TaF_5 is expected to require more energy than processes based on the other two precursors. Additionally, the Gibbs free energy change indicates that reactions with $TaCl_5$ and $TaBr_5$ show a greater tendency for spontaneity as compared to TaF_5 as the temperature increases (Figure 3.1b). Based on this data, $TaCl_5$ emerged as a promising precursor candidate for Ta deposition. $TaCl_5$ is a white crystalline solid at room temperature with a 1 Torr vapor pressure at ~ 110 °C. It has a heat of formation of -205 kcal/mol, bonding energy of ~ 41 kcal/mol, and melting point of 210 °C and can readily be stored in a stainless steel bubbler.

The thermodynamic calculation of Gibbs free energy change in the above reaction (Eq. 3.5) reveals that a thermal CVD Ta process requires very high temperature where the reaction becomes spontaneous (Figure 3.1b). However, the use of plasma in the CVD Ta process can significantly lower the deposition temperature. In the presence of plasma, $TaCl_5$ and H_2 gas are dissociated into active species according to the following reaction:

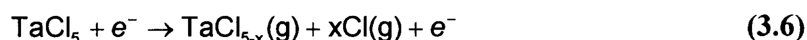

$$TaCl_5 + e^- \rightarrow TaCl_{5-x}(g) + xCl(g) + e^- \quad \textbf{(3.6)}$$

and

$$H_2(g) + e^- \leftrightarrow 2H(g) + e^- \quad \textbf{(3.7)}$$

Both Eq. 3.6 and Eq. 3.7 lead to the following reactions:

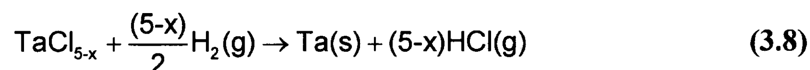

$$TaCl_{5-x} + \frac{(5-x)}{2} H_2(g) \rightarrow Ta(s) + (5-x)HCl(g) \quad \textbf{(3.8)}$$

and

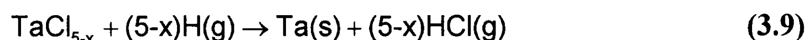

$$TaCl_{5-x} + (5-x)H(g) \rightarrow Ta(s) + (5-x)HCl(g) \quad \textbf{(3.9)}$$

where x represents the possible integers 1, 2, 3, or 4.

In Eq. 3.8 and Eq. 3.9, thermodynamic calculations of the Gibbs free energy change shows that the reaction in the presence of plasma spontaneously occurs even at relatively low deposition temperatures (Figure 3.2). In the presence of active hydrogen atoms, the reaction spontaneously takes place over the entire temperature regime of interest (Figure 3.2b).

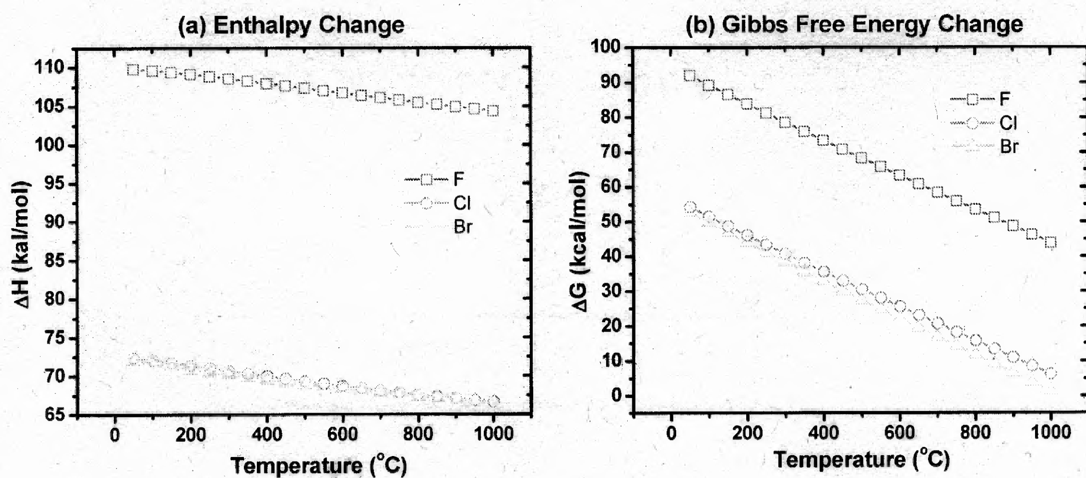

Figure 3.1 (a) Enthalpy and (b) Gibbs free energy change versus temperature.

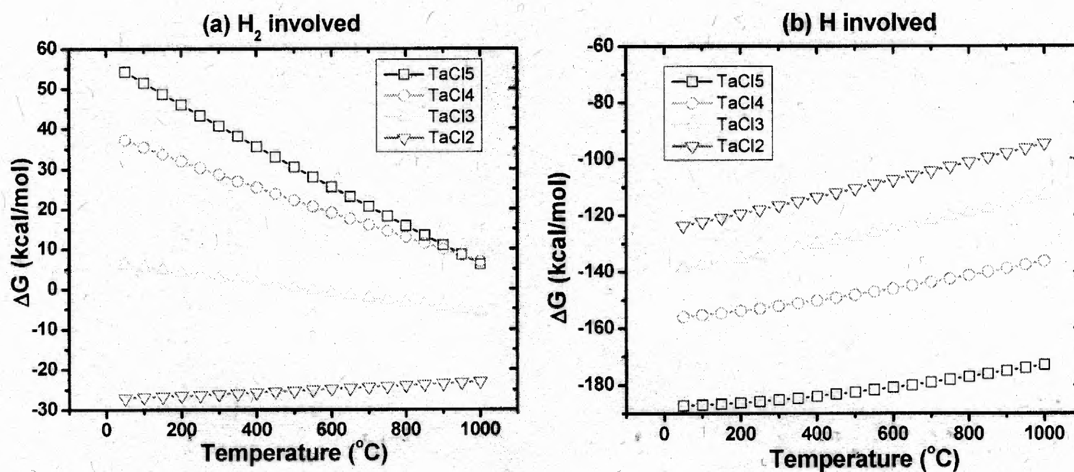

Figure 3.2 Gibbs free energy change in tantalum metallization reaction involving (a) hydrogen molecules (H2) and (b) active hydrogen atoms (H).

CHAPTER 4

PLASMA ENHANCED CVD TANTALUM ON HIGH STRENGTH STEELS

4.1 Introduction

The results of various characterization studies that were performed on the samples of Tantalum coatings are described in the following sub-sections of this chapter. These characterizations were aimed at standardizing the depositing process, so that the resulting coatings are suitable for protecting gun barrel. The initial study was aimed at synthesizing tantalum films which can perform conformal step coverage and pure α-Ta films. For this investigation, tantalum thin films with different deposition parameters on AISI 4340 steel coupons have been prepared by PECVD method. In the following sections, the properties of Ta thin films on steel coupon are discussed. The growth rate of tantalum thin films with respect to various PECVD deposition parameters are established. Furthermore, the effect of these deposition parameters on the composition, crystallographic structure and morphology of the Ta thin films is discussed. At the same time, the waste gases to environmental impact of CVD Ta are also evaluated. Finally, the chapter concludes by summarizing the PECVD parameters that produced α-Ta films with optimum qualities.

4.2 Topographical Characterization

Figure 4.1 illustrates the morphology of the surface of a CVD Ta coated nut (threaded inside) and EDX elemental analysis. SEM/EDX analysis indicates that inside of threaded tube is densely and uniformly covered with Ta coating.

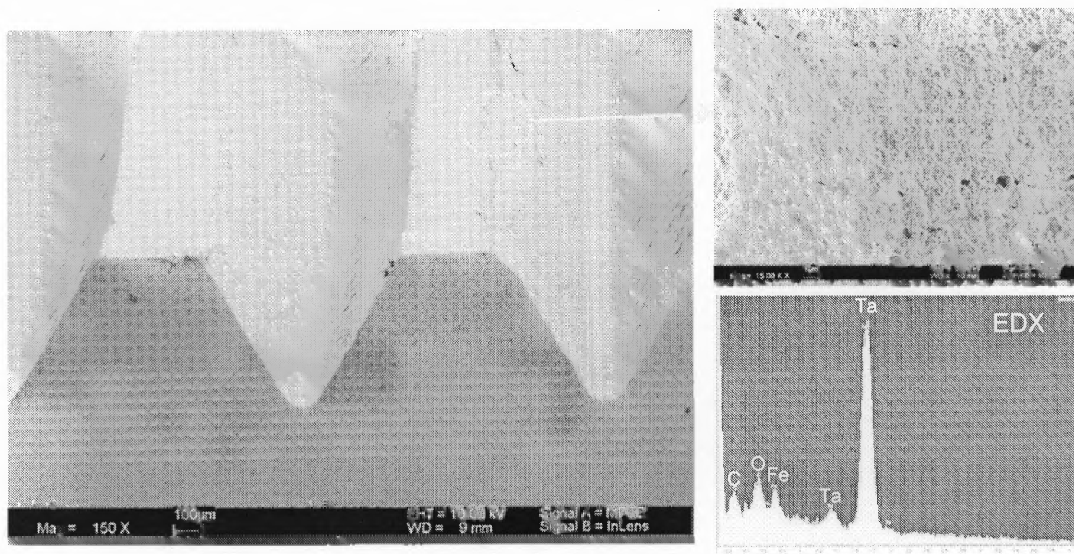

Figure 4.1 SEM surface images and EDX elemental analysis of CVD Ta coatings deposited inside nut.

Figure 4.2 shows the Tantalum morphology on polished AISI 4340 coupon under different magnification. The results reveal that the overall surface of the substrates is homogeneously covered by the coating with fewer defects. The very fine grain size is also observed on the surface. The elemental analyses by EDX of those coatings indicate that tantalum is the dominant specie.

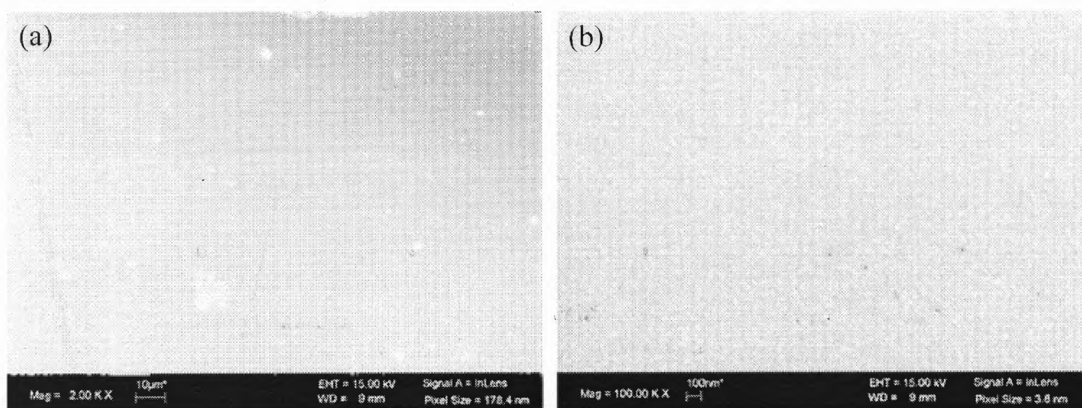

Figure 4.2 SEM surface images of CVD Ta coatings deposited on AISI 4340 steel coupons: (a) 2K X (b) 100K X.

Figure 4.3 illustrates a typical AFM topography observed for Ta coatings deposited on polished steel substrates. The results indicate that the coatings exhibit a relatively rougher surface (R_{RMS}=4.18 nm) to that of the underlying steel substrate (R_{RMS}=2.84nm).

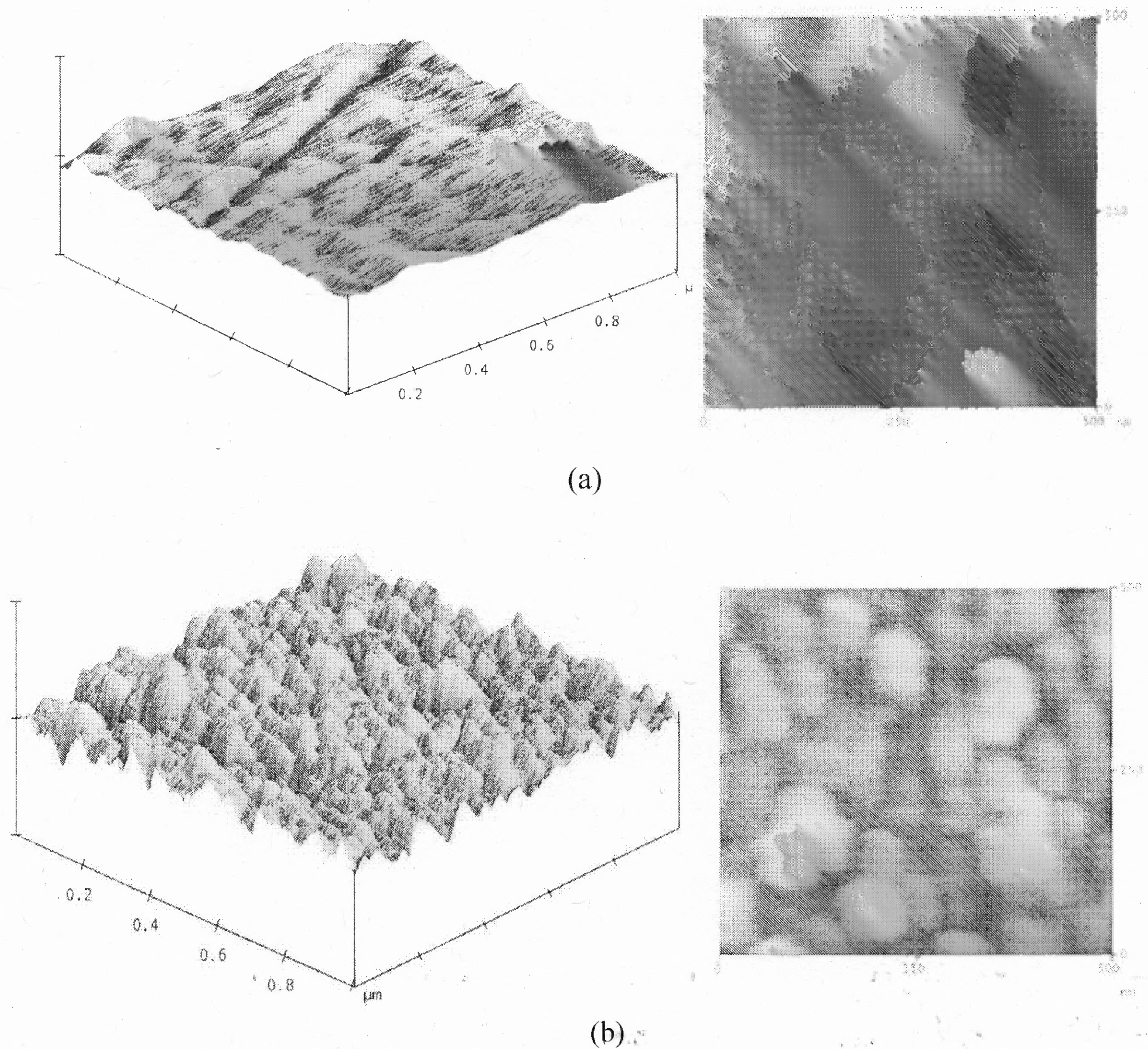

Figure 4.3 AFM topography on: (a) polished steel substrate as reference and (b) Ta coatings on polished steel substrate. (Both data scale is 50nm.)

4.3 Step Coverage Characterization

To evaluate the conformal coverage of the Ta coatings, the cross-section of Ta coatings deposited on polished and unpolished AISI 4340 steel substrate and V-groove Si wafer was investigated. Cross sectional FE-SEM revealed that the coatings exhibit uniform coating thickness (Figure 4.4) with excellent conformal step coverage (Figure 4.5).

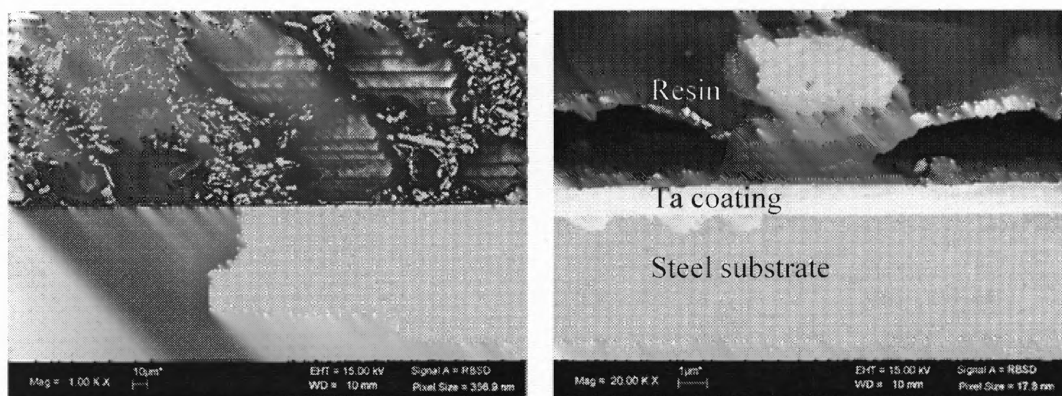

Figure 4.4 The cross-sectional SEM images of (a) CVD Ta on polished steel coupon

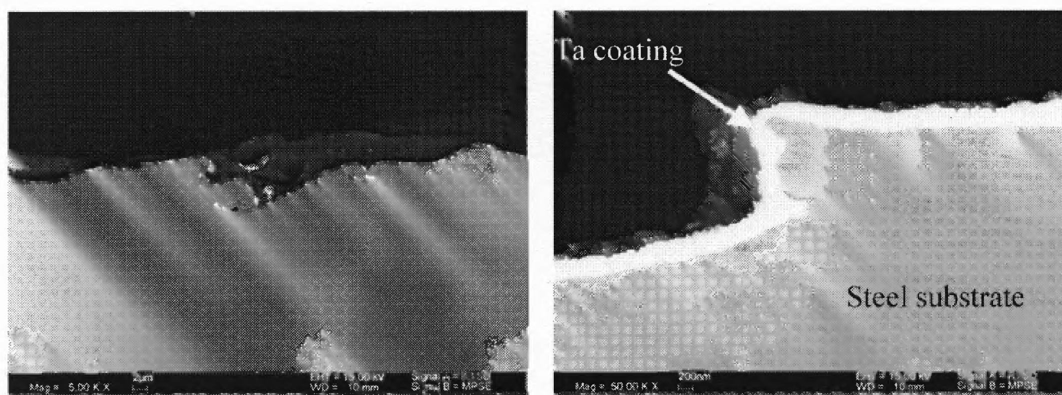

Figure 4.5 SEM images of cross sections of CVD Ta coatings.

Figure 4.6 indicates a step coverage that varied from ~90 % down to ~60 % as a function of depth from the surface of V-groove Si wafer.

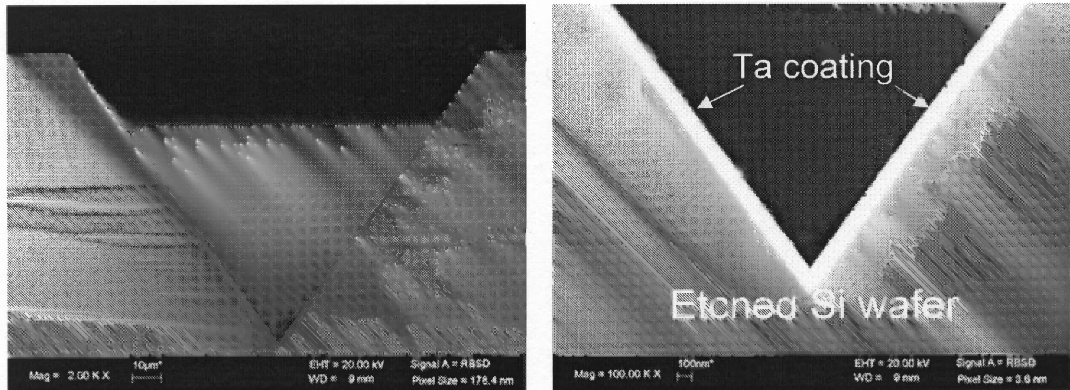

Figure 4.6 CVD Ta on V-grooved Si wafer (145 μm depth and 103 μm width)

4.4 Compositional Analysis

4.4.1 AES Depth Profile Analysis

To obtain comprehensive information on coating composition as a function of depth, AES analysis was performed on CVD Ta coated coupons. A typical Auger spectrum of a Ta coating prior to Ar etching is given in Figure 4.7.

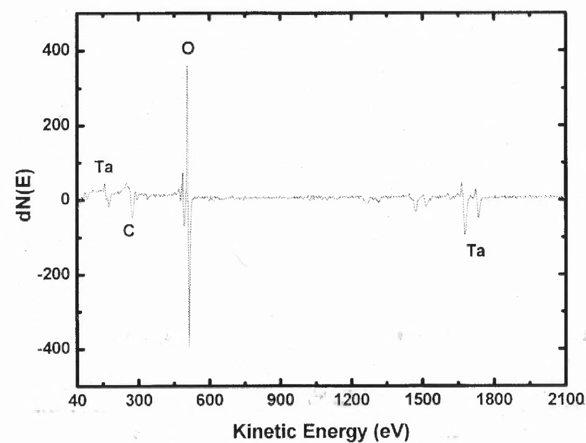

Figure 4.7 AES spectra of CVD Ta coatings.

The data reveals that carbon and oxygen are present as impurities on the surface. The chlorine, whose peak is obscured by the low-energy tantalum lines around 160 eV,

was found to be present within the detection limit (<1 at.%) of the instrument. Therefore, no depth profile was carried out for chlorine.

To obtain comprehensive information on coating composition as a function of depth, AES analysis was performed on CVD Ta coated coupons as shown in Figure 4.8. It illustrates the compositional depth profile of the elements including carbon, oxygen, and tantalum detected on the coating. The detected iron represents the underlying steel substrate. The results indicate the high purity Ta coatings with minor C and O impurities. The presence of the high oxygen concentration on the surface is indicative of the native tantalum oxide film that naturally forms on the surface. Carbon present on the surface was removed after the first Ar etching cycle, implying that the presence of carbon is most likely due to surface contamination. No significant variation in the purity of CVD Ta coatings was found at the various deposition conditions.

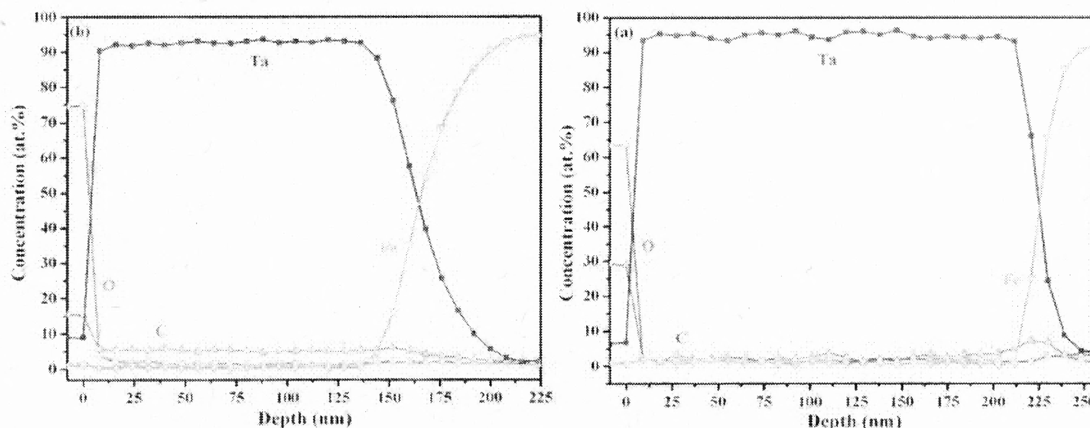

Figure 4.8 AES spectra of CVD Ta coatings on steel coupons produced under (a) 60 W (b) 100 W RF plasma power.

4.4.2 XPS Analysis

In order to evaluate the composition chemistry of the CVD Ta coatings, XPS analysis was performed on coatings deposited on AISI 4340 steel coupon. The survey

spectra of XPS measurements on the coating before depth profiling showed peaks for oxygen, carbon, and tantalum, consistent with the AES measurement. Figure 4.9 illustrates typical high-resolution XPS spectra of Ta4f, O1s, and C1s as a function of Ar sputter time. The depth profile of the Ta4f spectra (Figure 4.9 a) shows multiple peaks indicative of Ta in the oxide form at the surface followed by formation of metallic Ta below the surface. The oxygen peak remains fixed in position as a function of depth indicating the presence of a unique tantalum oxide layer (Figure 4.9 b). Using the half-maximum intensity of the oxygen signal as the interface marker in the XPS depth profile, the tantalum oxide on the surface was found to be 30~40 Å thick implying the formation of a native oxide film after deposition. From the XPS analysis of the C1s lines (Figure 4.9 c), the carbon detected in the coating was identified as adventitious carbon due to surface contamination. Overall, the compositional profile analysis confirmed that the CVD Ta coatings exhibit high purity with minor constituents of oxygen and chlorine in the bulk region.

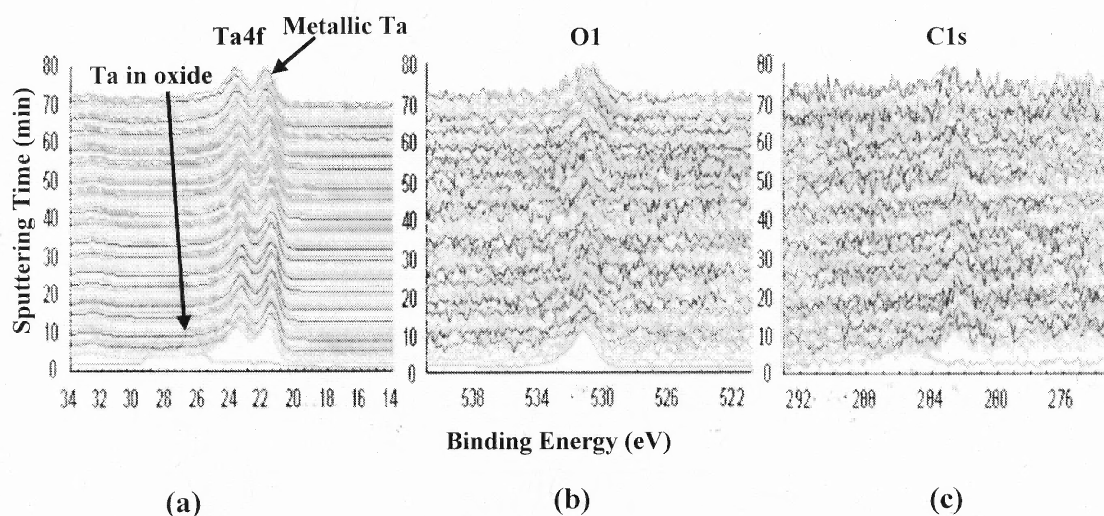

Figure 4.9 Depth profile of XPS spectra for CVD Ta coatings on polished steel substrate: (a) Ta 4f (b) O 1s (c) C 1s.

4.5 Crystallographic Structures Analysis

The microstructure of as-deposited and annealed PECVD Ta films is analyzed by XRD. The plasma working distance is discussed as the main experimental parameter to cause the α phase formation in PECVD Ta films. The in-situ annealing process is produced to evaluate the effects of thermal treatment for Tantalum phase formation. Namely, the samples temperature is increased to set temperature by 5 °C/min under 100 sccm He flow rate after Ta deposited. Then, the constant temperature was keep to 1 or 2 hours. After annealed, the samples are cooling down by 3 °C/min with 100 sccm He flow rate. The purpose of this thermal treatment is to establish baseline performance metrics and to determine the effects of annealing on the phase formation of Tantalum coatings.

4.5.1 The Crystallographic Structures Changed with Plasma Working Distance in PECVD Ta coatings

The crystallographic structures of Ta coatings deposited on steel substrates were examined using XRD with two theta (2θ) range from 20 to 120°. Figure 4.10 shows XRD patterns of CVD Ta coatings on polished steel substrates with different plasma power under different plasma working distance. The plasma working distance is defined as the distance between plasma shower head and substrate holder. The XRD patterns of Ta coatings were compared to those of tantalum references consisting of α (body centered cubic structure) and β (tetragonal structure) phases of tantalum. The proportion of α-Ta to β-Ta which varies from an α-Ta-rich phase (Figure 4.10 a) to a β-Ta-rich phase (Figure 4.10 c) mainly depends on the plasma working distance. When the plasma working distance was set to 2.5 inch, the XRD peak observed the only Ta peak at 38.438° which indicates α-phase Ta (110) and all other peaks represent those from the underlying steel

substrate (Figure 4.10 a). The α-Ta(110) was observed in all experiments with plasma working distance 2.5 inch. When the plasma working distance was decreased to 2 inch, the mixture of α and β phases was observed in some experiments (Figure 4.10 b). However, the pure α phase Tantalum still can be observed sometimes (Figure 4.10 b) even under the same deposition parameters. When the plasma working distance was further decreased to 1.5 inch, the intensity of the β phase Ta peak (002) and (513) was further enhanced (Figure 4.10 c). It illustrates that the proportion of β phases is increased after decreased the plasma working distance.

Deposition parameters control the structure and morphology in plasma enhanced CVD Ta coatings. The gas flow rate, plasma power, substrate nature, and substrate temperature can affect tantalum nucleation and growth. The one of main reason to cause α-phase Ta in PECVD process is the plasma working distance, and it is independent on the plasma power. The XRD analysis indicates that the lower plasma working distance more easily promoted the β-phase Ta. However, the plasma working distance is not the only factor controlling the formation of α-phase Tantalum. The substrate surface contamination may also play an important role in the growth of the α-Ta or β-Ta phase [55, 71, 72]. Westwood and Feinstein et. al. [55, 72] have already encountered a mixture of α and β phases in the PVD process. Westwood et.al [72] proposed that the tetragonal β-Ta is an impurity-stabilizing phase which is formed to accommodate impurities in the coatings at levels higher than the solubility limit for the bcc α-Ta. Theses studies report the high levels of impurities in the deposition chamber, substrate surface contamination, and a substrate that has low resistance to oxidation, all promoted the β phases Tantalum. The further investigations are necessary to understand this behavior. The observed

broadening of the peaks reflects the presence of small grains on the nano-scale. It is also identified by SEM and AFM results.

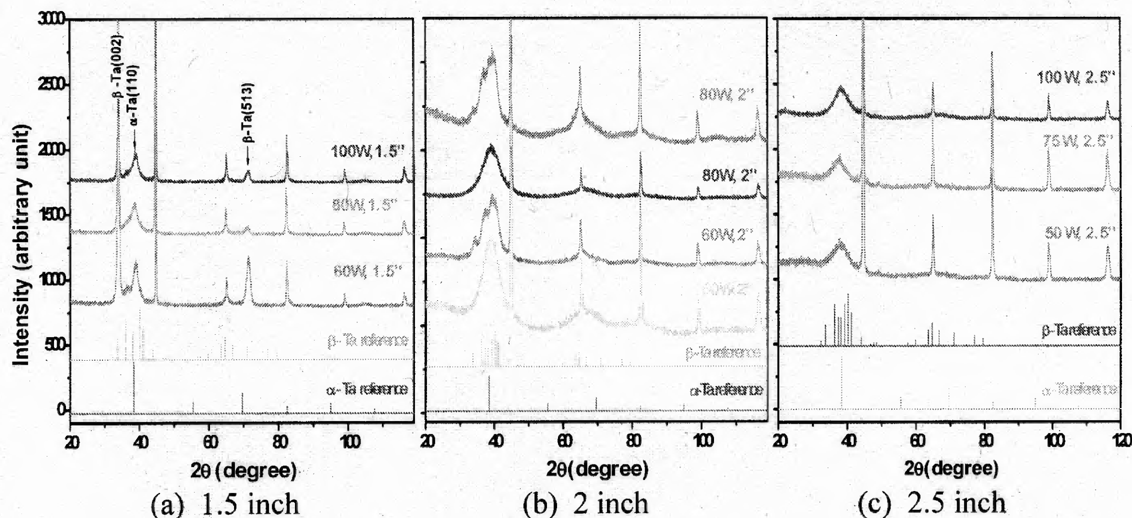

Figure 4.10 XRD patterns of CVD Ta coatings on polished steel substrates with different plasma power under different plasma working distance: (a) 1.5 inch, (b) 2 inch, and (c) 2.5 inch

4.5.2 Effects of Thermal Treatment on Ta Microstructure

The microstructure of Tantalum coatings pre- and post-annealed on polished AISI 4340 steel coupon and Ta foil were examined by XRD.

Figure 4.11 gives XRD spectra of as-deposited and post-annealed Ta coatings on polished AISI 4340 steel coupon under different annealing temperature and time. The XRD patterns of Ta coatings were compared to the tantalum references of α-Ta and β-Ta phases. Representative XRD spectra are displayed as follows: (a) annealed at 460 °C, 2 hours, (b) annealed at 430 °C, 1 hour, (c) no thermal treatment, (d) α-Ta reference, and (d) β-Ta reference. It is obvious that the β-Ta(002), β-Ta(410), β-Ta(411), and β-Ta(513) reflection lines were detected after annealing. Meantime, compared Figure 4.11 (a) and (b), the intensity of β-Ta(002) and β-Ta(513) were highly increased after using longer

annealed time (2 hours) and higher annealed temperature (460 °C). The phases of Ta thin films were changed from α-phase dominant Tantalum to β-phase dominant Tantalum after annealing process. The XRD data indicated that the annealing process could promote the β phase formation.

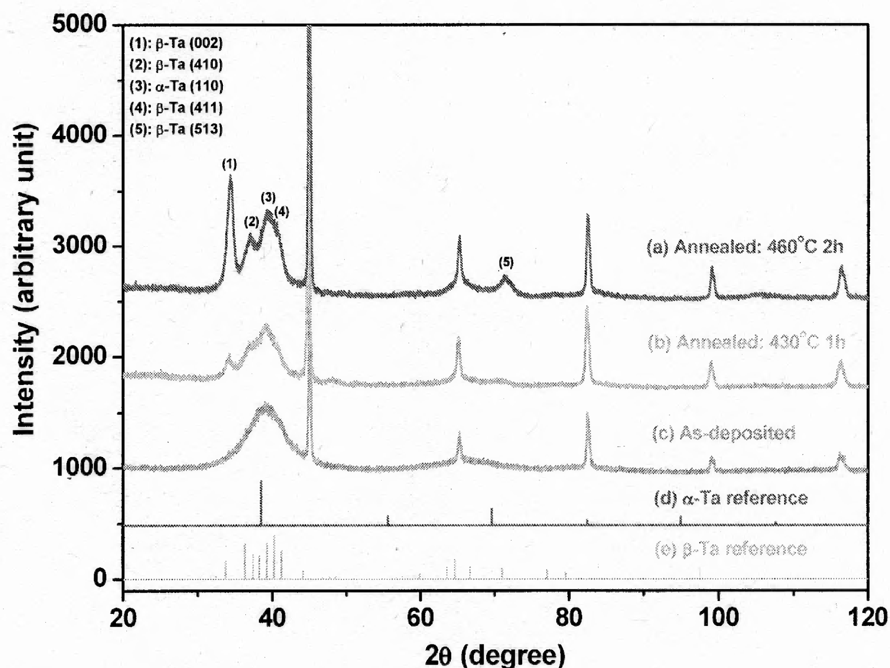

Figure 4.11 XRD patterns of PECVD Ta coatings on polished steel substrates: (a) annealed at 460 °C 2 h, (b) annealed at 430 °C 1 h, (c) as-deposited, (d) α-Ta reference, and (e) β-Ta reference

XRD spectra for Ta foil and post-annealed Ta coatings on the polished Ta foil substrates under different annealed temperature and time are shown in Figure 4.12. Ta coatings on Ta foil exhibit a mixture of α and β phases after annealed. XRD analysis of Pre- and post-annealed Ta coatings on the polished Ta foil indicates similar trend as PECVD Ta coatings on polished steel coupon. After 1 hour annealed at 430 °C, the clear β-Ta(002) and β-Ta(413) peaks were observed in Figure 4.12 (b). Under higher annealed temperature (460 °C) and longer annealed time (2 hours), the intensity of β-Ta(002) and

β-Ta(413) was increased and β-Ta(410) and β-Ta(411) were appeared. The similar XRD data on the Ta foil conformed that the β-phase of Ta thin films can be promoted by annealed process. The proportion of α-phase and β-phase Ta coatings depends on the annealed temperature and time.

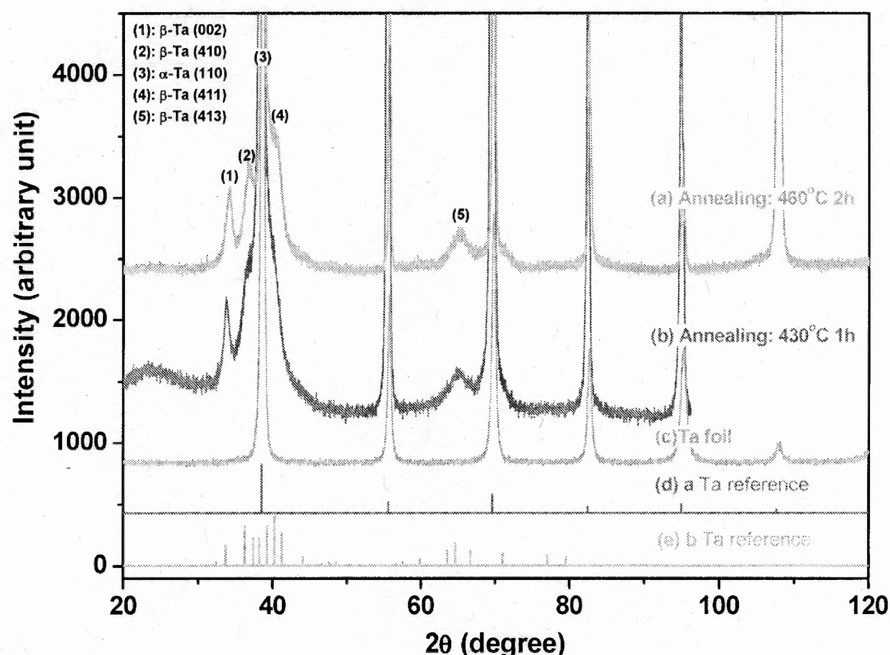

Figure 4.12 XRD patterns of CVD Ta coatings on polished Ta foil substrates: (a) annealed at 460 °C 2 h, (b) annealed at 430 °C 1 h, (c) Ta foil, (d) α-Ta reference, and (e) β-Ta reference.

4.6 Hydrogen Concentration Detected

Nuclear reaction analysis (NRA) for hydrogen profiling indicated the absence of hydrogen in Ta coatings. NRA yielded approximately only less than 0.55 at.% H in as-deposited PECVD Ta, as shown in Figure 4.13.

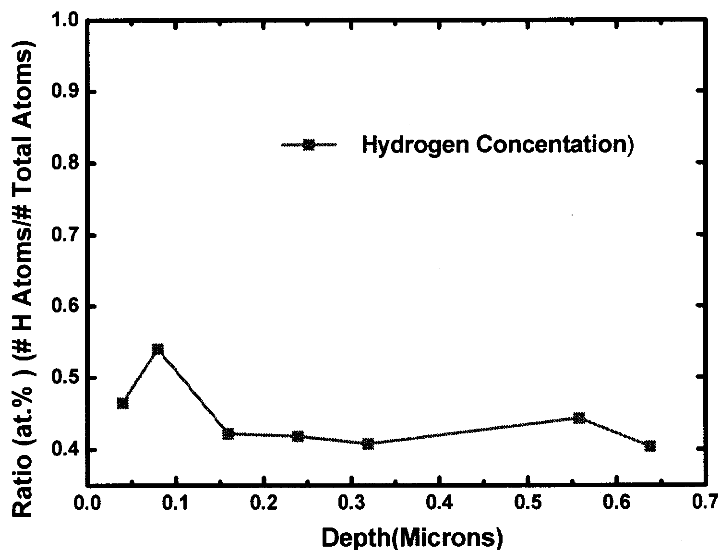

Figure 4.13 Hydrogen depth profiles in as-deposited PECVD Ta films.

4.7 X-ray Reflectivity Analysis

The X-ray Reflectivity (XRR) measurements revealed that the density of CVD Ta coatings on Si substrate was found to be ~ 15.6 g/cm^3, which is close to bulk Ta value of 16.6 g/cm^3.

4.8 Establish Growth Rate Dependence on Processing Parameters

4.8.1 Growth Rate with Respect to Precursor Temperature

To clearly indicate the relationship between actual evaporation rate and growth rate, the Figure 2.4 the evaporation rate versus the precursor temperature was superimposed onto Figure 4.14 the variation in growth rate as a function of precursor temperature. The scatter of triangles shows the growth rate in unit of angstrom per min. The squares stand for the average evaporation rate of precursor $TaCl_5$ in unit of gram per hour. The red line is the $TaCl_5$ evaporation rate with precursor temperature. By increasing the precursor

temperature from 105 to 110 °C, the growth rate is observed to increase by a factor of 2 reflecting the increase in vapor pressure within the reactor (Figure 2.1). However, the growth rate is slightly increased when the precursor temperature is increased from 110 to 120 °C. It confirms that the growth rate of Tantalum thin film is proportional to the evaporation rate of $TaCl_5$ precursor.

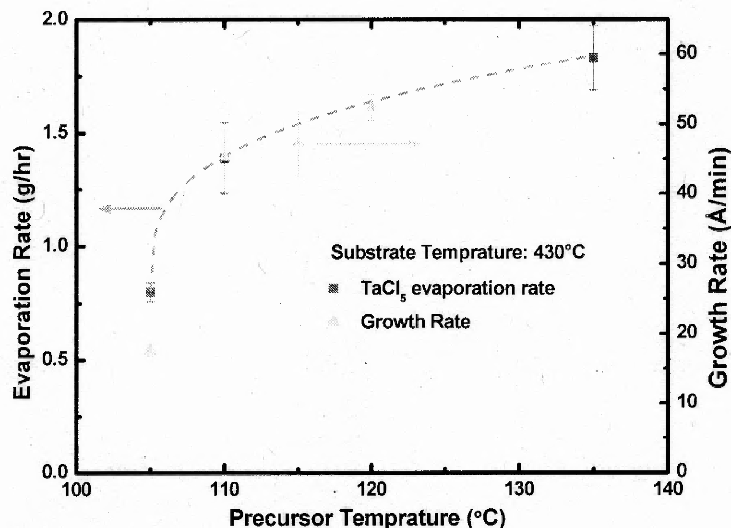

Figure 4.14 The influence on the growth rate with the various precursor temperatures (process pressure = 2 Torr, deposition temperature = 430 °C, plasma power = 60W, plasma working distance = 1.5").

4.8.2 Growth Rate with Respect to Plasma Power and Plasma Working Distance

The growth rate of CVD Ta coating as a function of RF plasma power is shown in Figure 4.15. A significant enhancement in growth rate was observed by decreasing the distance between the plasma shower head and substrate, and by increasing precursor temperature. The shorter plasma working distance will increase the plasma density. For the 2.5" distance, the growth rate was increased monotonically with higher RF plasma power. However, for the 2.0" distance, the growth rate exhibited a peak value at 80 W

presumably due to the onset of etching effects of the substrate at higher RF plasma powers.

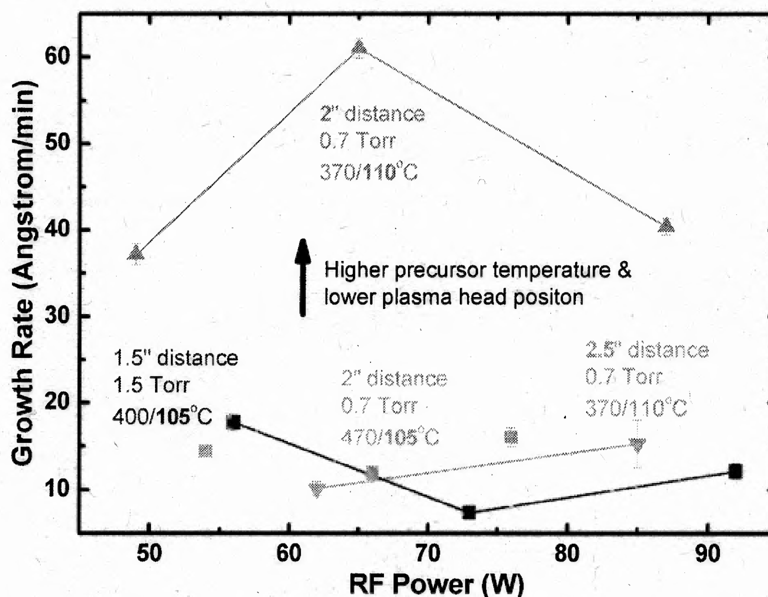

Figure 4.15 The plot of the growth rate vs. RF plasma power: Deposition conditions (process pressure = 0.7 Torr, deposition temperature = 370 °C and precursor temperature = 110 °C)

4.8.3 Growth Rate with Respect to Substrate Temperature

The deposition process shown in Figure 4.16 can be grouped into (i) mass transport-limited regime and (ii) surface reaction-limited regime. The steps are sequential and the slowest process is the rate determining step. If the deposition process is limited by the mass transfer, the transport process occurred by the gas-phase diffusion is proportional to the diffusivity of the gas and the concentration gradient. The mass transport process which limits the growth rate is only weakly dependent on temperature. The activation energy E_a is usually less than 40 KJ/mol for mass transport-limited process. On the other hand, it is very important that the same concentration of reactants be present in the bulk gas regions adjacent to all locations of a wafer, as the arrival rate is directly proportional

to the concentration in the bulk gas. Thus, to ensure films of uniform thickness, reactors which are operated in the mass-transport-limited regime must be designed so that all locations of wafer surfaces and all wafers in a run are supplied with an equal flux of reactant species.

If the deposition process is limited by the surface reaction, the activation energy E_a is usually 40-100 KJ/mol for surface process. In the operating regime, the deposition rate is a strong function of the temperature and an excellent temperature regime, the deposition rate is a strong function of the temperature and an excellent temperature control is required to achieve the film thickness uniformity that is necessary for controllable integrated circuit fabrication.

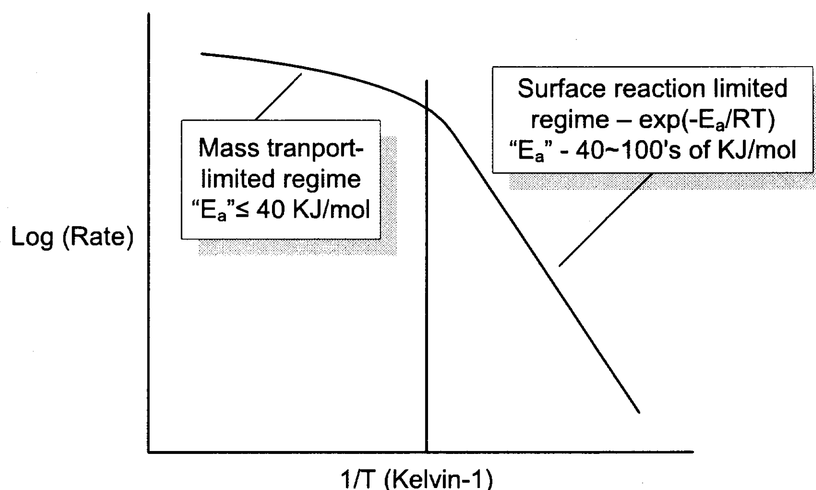

Figure 4.16 Deposition rate as a function of substrate temperature exemplifying diffusion controlled and surface-reaction controlled regimes

On the other hand, under such conditions the rate at which reactant species arrive at the surface is not as important. Thus, it is not as critical that the reactor be designed to supply an equal flux of reactants to all locations of the wafer surface. It will be seen that in horizontal low pressure CVD reactors, wafers can be stacked vertically and at very

close spacing because such systems operate in a surface-reaction-rate limited regime. In deposition processes that are mass-transport limited, however, the temperature control is not nearly as critical. As shown in Figure 4.16 [73], a relatively steep temperature in the lower range and a milder dependence in the upper range are indicating that the nature of the rate-controlling step changes with temperature. Furthermore, any study of temperature dependence should be supplemented by studies of gas flow rate dependence: a true "surface reaction-limited" is independent of flow rate and dependent on concentration, whereas a "mass transport-limited" reactor displays a deposition rate linearly proportional to the inlet flow rate.

The deposition rate of the CVD Ta coating was determined as a function of temperature between 400 and 460 °C while maintaining a constant pressure of 2 Torr, a carrier gas flow rate 10 sccm, plasma power 60 W, and plasma working distance 1.5". The activation energy Ea of the reaction in the plasma environment can be calculated by Arrhenius equation:

$$R(T) = R_0 e^{(E_a/KT)} \quad \textbf{(4.1)}$$

where R(T) is the rate constant at temperature T (in units of absolute temperature [Kelvin, or K]), R_0 is the frequency factor (also referred to in some cases as the pre-exponential factor), k is Boltzmanns constant ($8.6*10^{-5}$ eV/K), and Ea is the activation energy (expressed in units of eV). The unit can be transferred to KJ/mol using 1 J = $60.24*10^{18}$ eV.

As seen in Figure 4.17, a plot of the average deposition rate versus inverse substrate temperture. The growth rate is increased by increasing the substrate temperature between 400 and 460 °C. It follows an Arrhenius behavior between 400 and

460 °C which yields and apparent activation energy of 25.13 KJ/mol. This suggests a rate mechanism controlled by gas-phase diffusion or one that is complex [74]. The transport process occurred by the gas-phase diffusion is proportional to the diffusivity of the gas and the concentration gradient. The growth rate is only weakly dependent on temperature in this process.

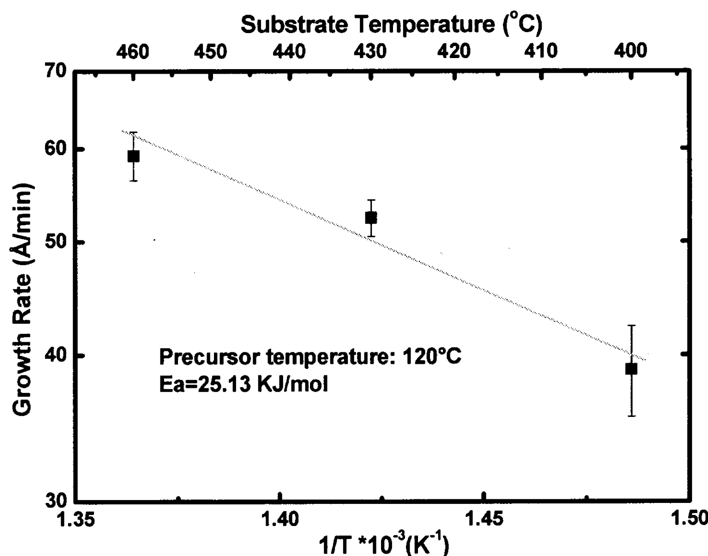

Figure 4.17 Variation of growth rate as a function of inverse substrate temperature: (■) mark (process pressure = 2 Torr, plasma power = 60 W, precursor temperature = 120 °C and plasma working distance = 1.5")

4.9 Result and Discussion

Tantalum coatings have successfully been deposited on steel substrates using tantalum pentachloride ($TaCl_5$) as the preferred precursor. SEM analysis provided proof that CVD Ta coatings can be deposited uniformly and conformally. AFM analysis indicated that the Ta coatings are continuous and exhibit the typical topography expected of CVD metals. The compositional analyses (AES, XPS and NRA) revealed that CVD Ta coatings are essentially pure with minor impurities of oxygen and chlorine present in the bulk of the

coatings. Hydrogen concentration is less than 0.55 at.% in the coatings. The XRD analysis of the CVD Ta coatings confirmed the presence of α or β phase rich Ta according to the deposition condition.

The plasma working distance is discussed as the main experimental parameter to cause the α-phase formation in PECVD Ta deposition process. Our results show that the proportion of β phases is increased after decreased the plasma working distance. The in-situ annealing process is produced to evaluate the effects of thermal treatment for Tantalum phase formation. The intensity of β-Ta (002) and β-Ta (513) were highly increased after using longer annealed time (2 hours) and higher annealed temperature (460 °C). The XRD data analysis indicated that the annealing process could promote the β phase formation. The growth rate was significantly enhanced by decreasing the distance between the plasma shower head and substrate and thus increasing the plasma density. The growth rate increased with increase in the precursor temperatures and deposition temperatures. XRR measurements showed that the density of the CVD Ta coatings (15.6 g/cm^3) is closed to that of bulk Ta (16.6 g/cm^3).

CHAPTER 5

PLASMA ENHANCED CVD TANTALUM ON VARIOUS SEED LAYERS

5.1 Introduction

The tantalum structure after deposition also mainly depends on the substrate or underlaying material [45]. Chen et al. [75] found that a titanium layer inhibits the formation of tetragonal β-Ta, and leads to deposition of cubic α-Ta arising from its epitaxial orientation on the underlying titanium. Sota [9] also reported that β-Ta structure was observed on a number of substrates except titanium. Lee et al. [76] reported triode-sputtered tantalum with an Nb interface layer produced α-phase tantalum coatings on steel cylinders, but adhesion improvement was needed. Lee and Windover [40] found that α-phase nucleation and growth of tantalum could be controlled by using the Nb sublayer, regardless of the impurity concentration. Matson et al. [12] showed that the use of a niobium seed layer or buffer layer promotes the formation of bcc Ta on gun steel. Sajovec et al. [41] also stated that the niobium underlayer thickness was critical with respect to the nucleation process of tantalum. α-Ta can be prepared if the films are deposited over thin (greater than 3 nm) Nb seed layers. When less than 3 nm, tantalum films resulted in mixtures of α and β phases. They concluded that this stems from the fact that niobium as a very thin film on fused silica exists as a phase different in its properties from the common bcc-Nb phase. β-Ta was observed after sputtering onto SiO_2 or (111)-textured Cu by a dc-magnetron sputtering system, with the orientation of the Ta grains depending on the Ta layer thickness. On the other hand, α-Ta was observed on an (111) Al underlayer due to epitaxial relations [45]. Gladczuk [77] recently reported that bcc

phase of Ta rather than β-Ta was grown on unheated substrates first covered with thin layers of fcc tantalum nitride by DC magnetron sputtering.

Although the literature search revealed that a few candidates would fit the criteria, however, there is no one who fabricated α phase tantalum using chemical vapor deposition method so far. In this chapter, the various seed layers were used to try to promote the α-phase formation, such as Cr, Au, Nb, Pt, Ti, and TaNx. Almost all seed layers were prepared by using magnetron sputtering PVD. Only the Cr coatings were prepared two methods which are magnetron sputtering and electroplated methods. TaNx was formed by in-situ reaction using NH_3 or N_2 in combination with the $TaCl_5$ precursor. For the investigation, the tantalum thin films on various seed layers have been prepared by PECVD. The results of various characterization studies that were performed on the samples of Tantalum coatings are described. These characterizations were aimed at standardizing the depositing process and evaluating the effect of seed layers which could promote pure α-Ta coating. In the following sections, the influence of different seed layers on the composition, morphology, and crystallographic structure of the Ta films was discussed. Furthermore, the best choice of seed layers to promote α phase formation is deduced. Finally, the chapter concludes the use of an underlaying lattice-matched seed layer by summarizing the effect of seed layers that could promote α-Ta films.

5.2 Ta Coatings on Chromium Seed Layer

5.2.1 Surface Morphology and EDX analysis of Ta on Sputtered Cr Seed Layer

Figure 5.1 compares the SEM surface morphology between sputtered Cr coated only and after Ta deposited on Cr coated on polished AISI 4340 steel coupon under lower and

higher magnification. The needle shape morphology is observed on the sputtered Cr thin film Figure 5.1(b). After Ta was deposited on the sputtered Cr coating, the typical CVD Ta morphology was observed in Figure 5.1(c,d). Ta coatings have very fine grain size. The particle size is about 70nm from Figure 5.1(d). It is composed of further smaller grain. A few bigger Ta clusters are scattered on the surface of Ta coatings. The size of clusters is about 500nm. It is consisted of many smaller Ta particles. It is obvious that the sputtered Cr coatings are completely covered by the Ta coatings on the surface. The results also reveal that the Ta coatings are continuously conformal with few defects.

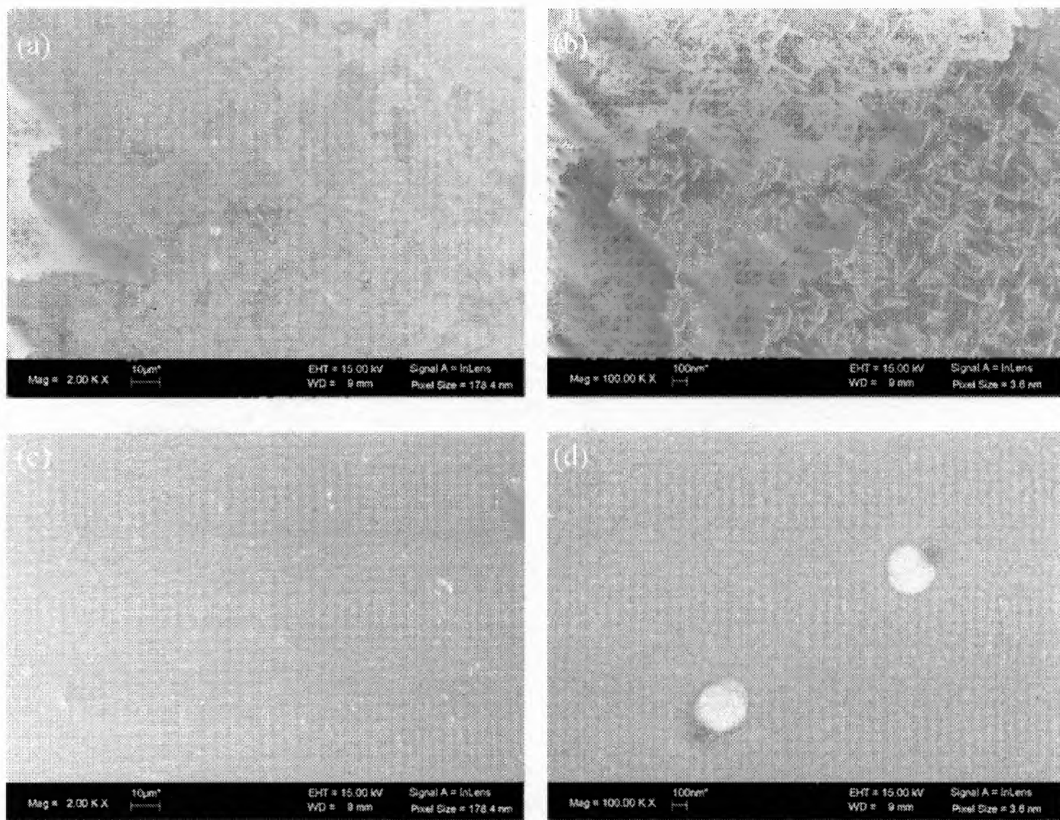

Figure 5.1 Comparison of SEM surface images of CVD Ta coatings deposited on sputtered Cr coated steel substrates under different magnification: (a,b) sputtered Cr coating only, (c,d) Ta on Cr-coated steel substrate

The same Figure 5.2 shows the EDX patterns before and after Ta deposited. On the EDX spectra, the Cr Lα line is strong before Ta deposition. After Ta deposited, the intensity of Cr Lα becomes very weak and the Ta Mα line appears with a very strong intensity. The elemental analyses by EDX also indicate that tantalum turns into the dominant species on the surface of Cr-coated steel substrate after Ta was deposited.

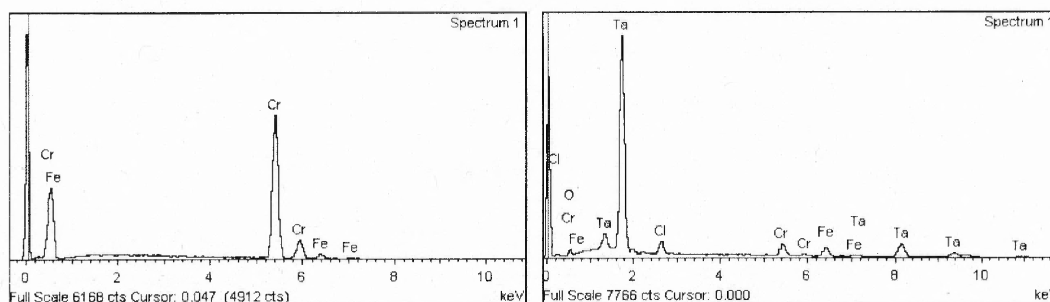

Figure 5.2 EDX patterns before and after Ta coated on sputtered Cr-coated polished steel substrate.

Figure 5.3 illustrates AFM topography of Ta coatings on the sputtered Cr-coated polished steel substrate with the surface roughness about 5.05 nm.

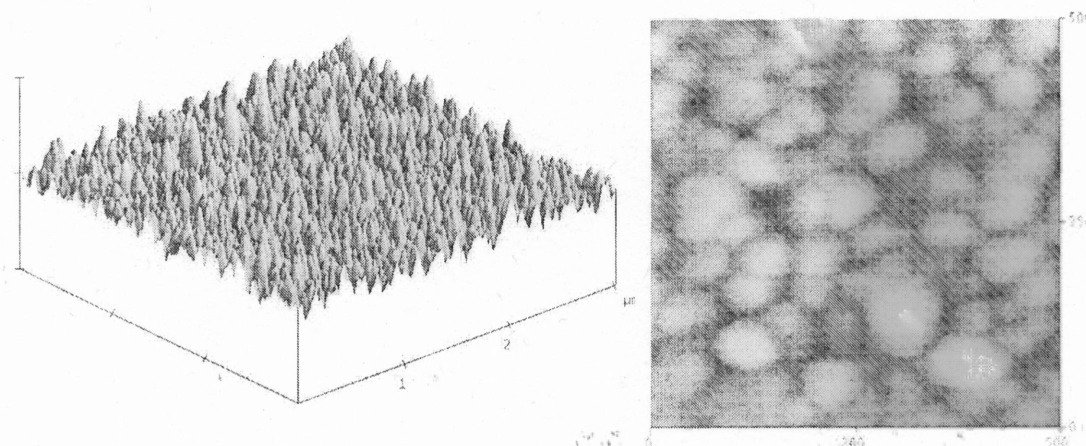

Figure 5.3 Ta AFM 3D and 2D topography of sputtered Cr coated on polished steel substrate (Data scale: 50nm, R_{RMS}=5.05nm.)

5.2.2 Surface Morphology and EDX analysis of Ta on Electroplated Cr Seed Layer

Figure 5.4 illustrates the surface morphology of electroplated Cr coating on the polished AISI 4340 steel coupon and Ta on electroplated Cr-coated steel substrate under different magnification. Figure 5.4 (a,b) shows that electroplated Cr coating has very rough surface and the particle size is about 1 to 2 micron. The edge of those particles is looks sharp. After deposited Ta on the electroplated Cr coating, the similar shape of particles still can be seen. However, the edge of those particles becomes smooth. The electroplated Cr coating has been completely covered by very fine Ta particles.

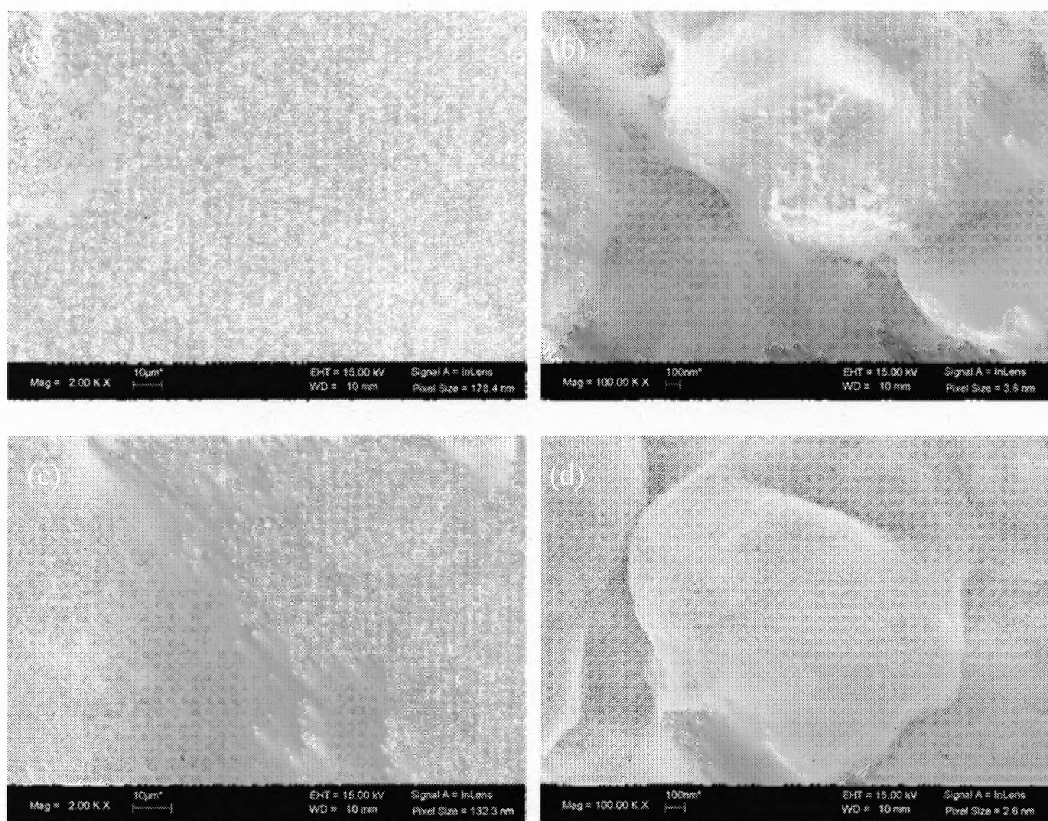

Figure 5.4 Comparison of SEM surface images of CVD Ta coatings deposited on electroplated Cr coated steel substrates: (a,b) electroplated Cr coating only, (c,d) Ta on Cr-coated steel substrate.

Figure 5.5 illustrates the EDX patterns before and after Ta deposited on electroplated Cr-coated steel substrate. The high intensity of Ta Mα line is clearly observed after Ta deposited on the electroplated Cr coating. The intensity of Cr Lα line becomes weaker but still strong. It could be because the thickness of CVD Ta coatings is too thin on the surface of electroplated Cr.

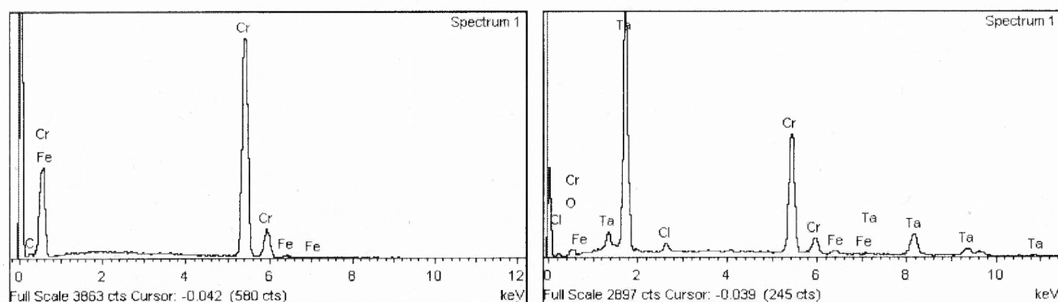

Figure 5.5 EDX patterns of Ta on electroplated Cr-coated polished steel substrate

The AFM topography of Tantalum coating on electroplated Cr-coated on polished steel substrate is shown in Figure 5.6. The surface roughness is about 280.38 nm.

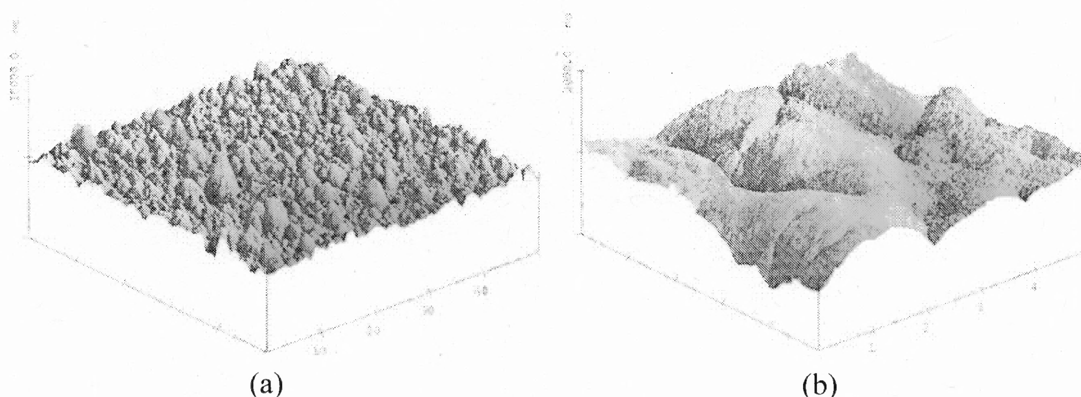

Figure 5.6 Ta AFM 3D topography of electroplated Cr coated on polished steel substrate (Data scale: (a) 5 μm, (b) 1 μm; R_{RMS}=280.38nm.)

5.2.3 Ta Microstructure Comparison on Different Methods Deposited Cr Substrates

Comparison of Ta microstructure is examined in this section. Both samples were obtained under same plasma power and similar deposition parameters. The XRD

microstructure of Tantalum coatings with sputtered Cr-coated and electroplated Cr-coated on polished AISI 4340 steel coupon are displayed in Figure 5.7. The XRD patterns of Ta coatings are compared to the tantalum references of α-Ta (Figure 5.7 e) and β-Ta (Figure 5.7 f) phases. The peaks of sputtered Cr (Figure 5.7 b) and electroplated Cr (Figure 5.7 d) are highly overlapped with the peaks of steel. XRD analysis indicates that PECVD Ta coatings exhibit a mixture of α and β phases Ta on sputtered Cr-coated and electroplated Cr-coated seed layers. Figure 5.7 (a) gives XRD spectrum of Ta coatings on sputtered Cr-coated seed layer. It shows high intensity of β-Ta(002) and small peak of β-Ta(513) as well as α-Ta(110). However, the intensity of β-Ta(002) is decreased when the electroplated Cr-coated was used as the seed layer and the intensity of α-Ta(110) is increased simultaneously. XRD analysis indicates that Ta coating on Cr seed layer exhibit the mixture α- and β- phase Ta and Cr seed layers do not promote α phase formation. However, sputtered Cr shows more crystalline β-phase.

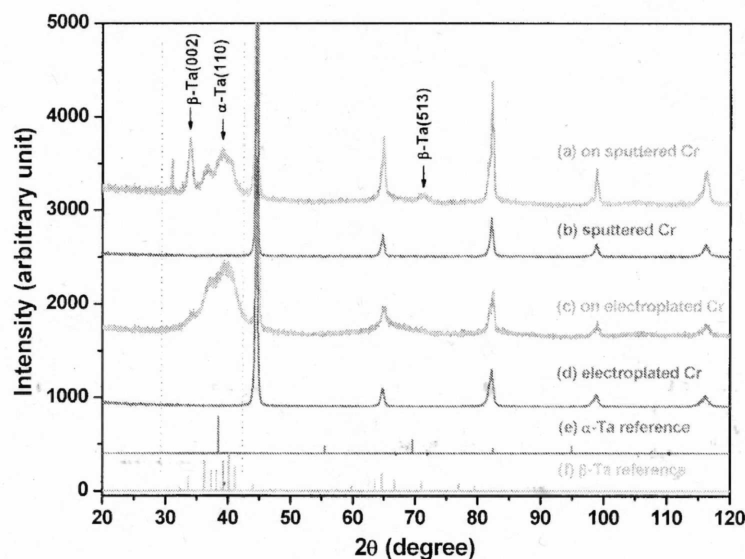

Figure 5.7 Comparison of Ta XRD patterns on Sputtered Cr-coated (b) and electroplated Cr-coated (d) polished steel substrate. (a) Ta on sputtered Cr, (c) Ta on electroplated Cr, (e) α-Ta reference, and (f) β-Ta reference

5.3 Ta Coatings on Au Seed Layer

The SEM surface morphology of sputtered Au coating and PECVD Ta coating on Au-coated polished AISI 4340 steel coupon is shown in Figure 5.8 under different magnification. Figure 5.8 (a,b) shows that the sputtered Au coating is uniformly covered on the steel substrate with particle size about 70nm. Figure 5.8 (c,d) shows the typical CVD Ta morphology was observed on the Au-coated steel surface. After Ta deposited, the typical Au coating can not be observed any more. It indicates that the sputtered Au coatings were completely covered by the Ta coatings. The results also reveal that the Ta coatings are continuously conformal with few defects. The very fine grain size is observed on the surface.

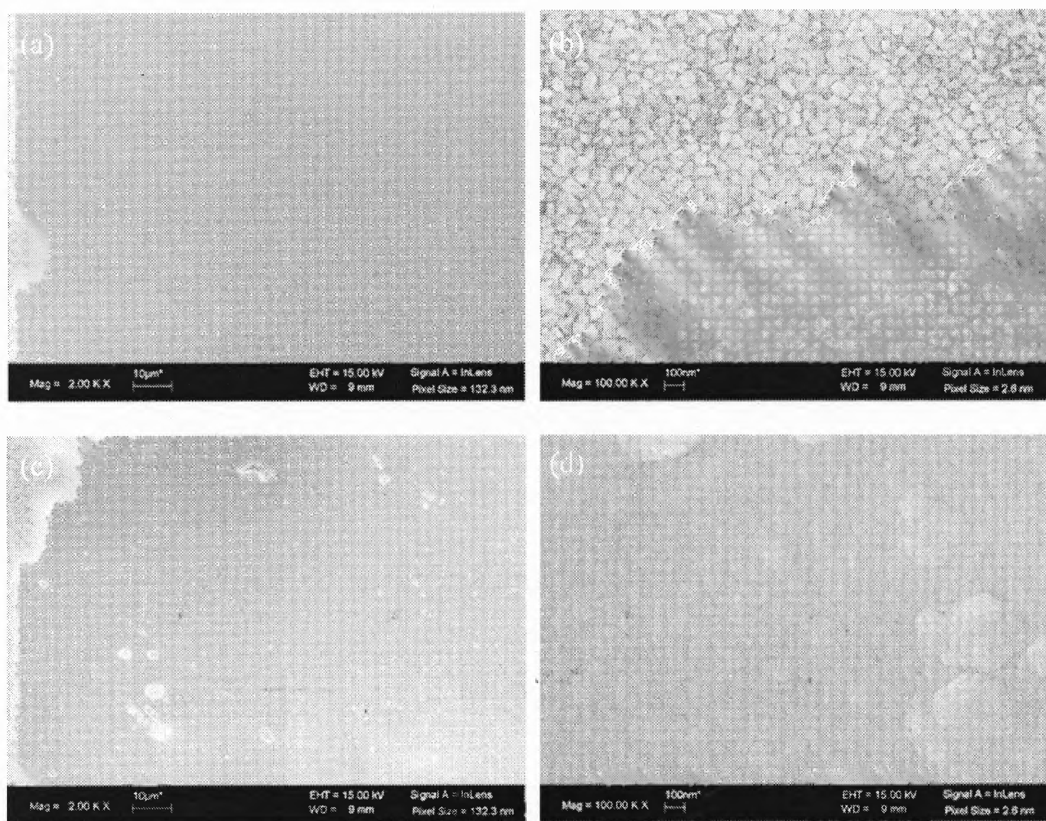

Figure 5.8 Comparison of SEM surface morphology without (a,b) and with (c,d) Ta coatings on Au-coated steel substrates

Figure 5.9 illustrates the EDX patterns before and after Ta deposited on sputtered Au-coated steel substrate. The EDX pattern shows the Mα line of Au has changed to Mα line of Ta. This also confirms that the Ta coatings have uniformly covered on the Au-coated steel substrates.

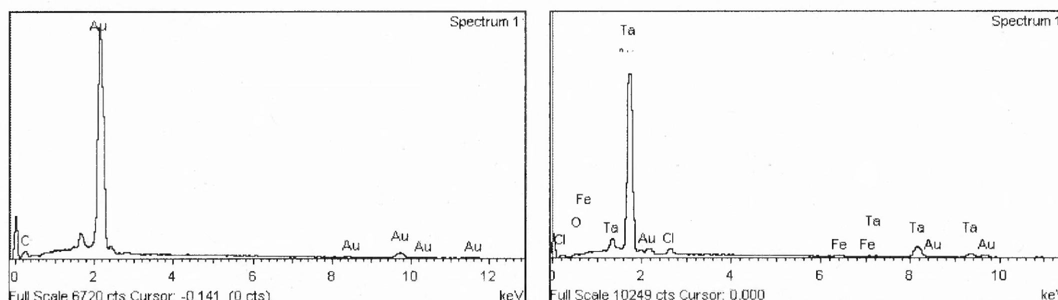

Figure 5.9 EDX patterns of Ta on sputtered Au coated polished steel substrate

The AFM topography of Tantalum coating on Au-coated on polished steel substrate is shown in Figure 5.10. The surface roughness is about 8.496 nm.

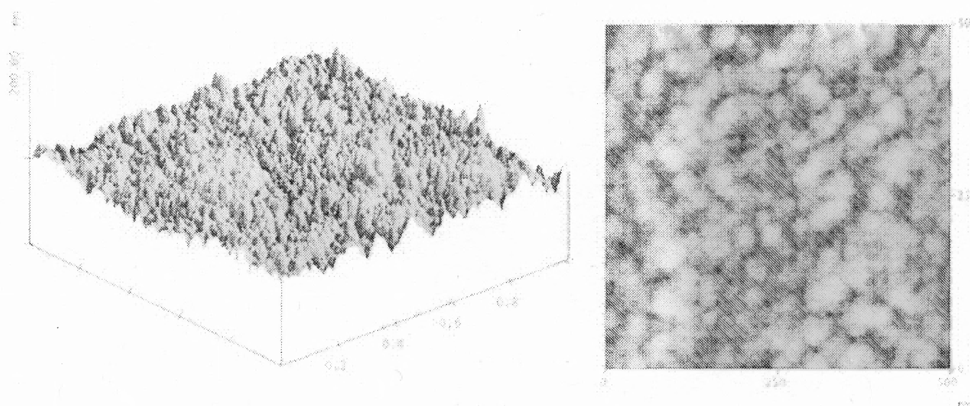

Figure 5.10 Ta AFM 3D and 2D topography of Au-coated on polished steel substrate (Data scale: 200nm, R_{RMS}=8.496nm.)

Figure 5.11 illustrates the XRD spectrum of Tantalum coatings on the sputtered Au-coated polished steel substrate and Au-coated Si wafer. The XRD pattern of Au coating also is showed as a reference. Because the Au(111) is highly overlapped with α-Ta (110), it is hard to recognize the peak of Tantalum from the XRD spectra. However,

all major β phase peaks, like β-Ta (002) and β (513), no longer exist. No evidence of β phase formation is exhibited by CVD Ta coatings deposited on Au seed layer.

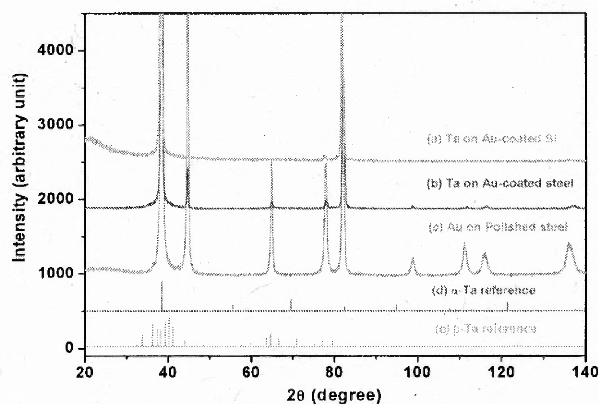

Figure 5.11 XRD patterns of CVD Ta coatings: (a) Ta on Au-coated polished steel substrate (b) Ta on Au-coated Si wafer, and (c) Au coating on polished steel substrate.

In order to recognize the Tantalum peaks, the grazing incidence XRD was been done. Figure 5.12 shows grazing incidence XRD data of CVD Ta coated on Au with different grazing incidence angle: (a) 5°, (b) 3°, (c) 2°, and (d) 1°. This method, which provides structural information of the top coating only, reveals the presence of a clear peak around 38.4° reflecting presence of the alpha phase.

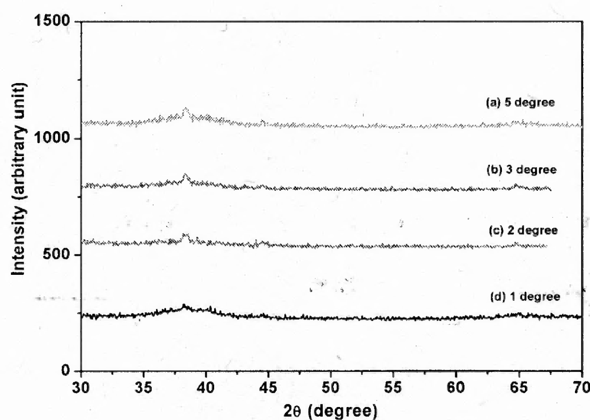

Figure 5.12 Grazing incidence XRD data of CVD Ta coated on Au with different grazing incidence angle: (a) 5°, (b) 3°, (c) 2°, and (d) 1°

5.4 Ta Coatings on Niobium Seed layer

Figure 5.13 compares the SEM surface morphology before and after Ta deposited on sputtered Nb-coated on polished AISI 4340 steel coupon under different magnification. Figure 5.13 (a,b) shows very smooth sputtered Nb surface with no obvious Nb particles boundary and with few defects. Figure 5.13 (c,d) shows very fine grain CVD Ta coatings. There are lots of bright big clusters which are comprised of much smaller particles scattered on the Ta surface. The size of those clusters is about several hundred nanometers.

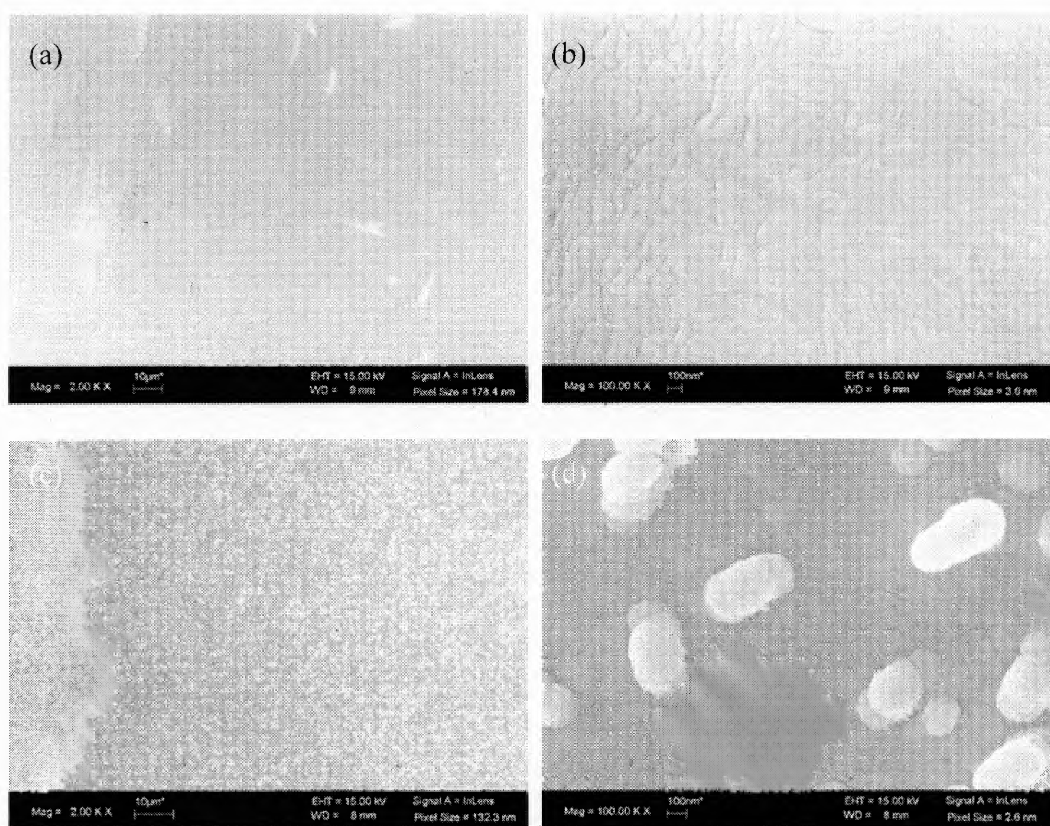

Figure 5.13 Comparison of SEM surface images of CVD Ta coatings deposited on sputtered Nb-coated steel substrates: (a,b) sputtered Nb coating only, (c,d) Ta on Nb-coated steel substrate.

Compared before and after Ta deposited on the Nb coating, the sputtered Nb coatings is completely covered by the Ta coatings on the surface. The results also reveal that the Ta coatings are continuously conformal with few defects.

Figure 5.14 illustrates the EDX patterns before and after Ta deposited on sputtered Nb-coated steel substrate. After Ta deposited, the Mα line of Nb has been replaced by Mα line of Ta in the EDX spectra. It indicates that the Nb coating has been completely covered by Ta coating.

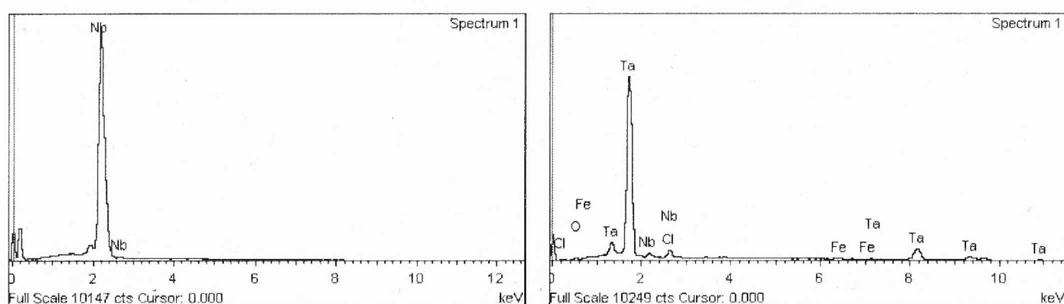

Figure 5.14 EDX patterns of Ta on sputtered Nb coated polished steel substrate

The AFM topography of Tantalum coating on sputtered Nb coated on polished steel substrate is shown in Figure 5.15. The surface roughness is about 18.705 nm.

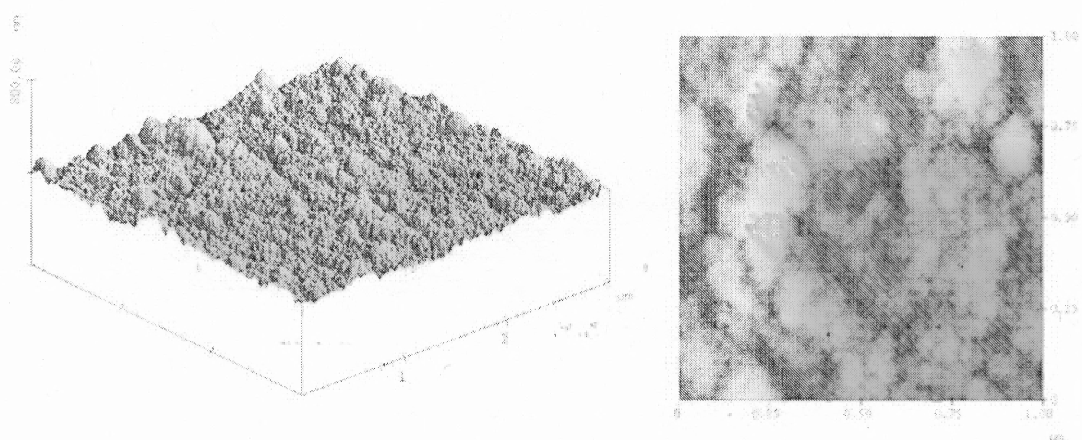

Figure 5.15 Ta AFM 3D and 2D topography of sputtered Nb coated on polished steel substrate (Data scale: 400nm, R_{RMS} = 18.705 nm.)

Figure 5.16 illustrates the XRD spectrum of Ta coatings on the sputtered Nb-coated polished steel substrate and Si wafer with sputtered Nb coating as a reference. The Nb(110) are highly overlapped with Ta(110). Although it is hart to recognize the Ta peak and Nb peak, there is no evidence of β phase formation.

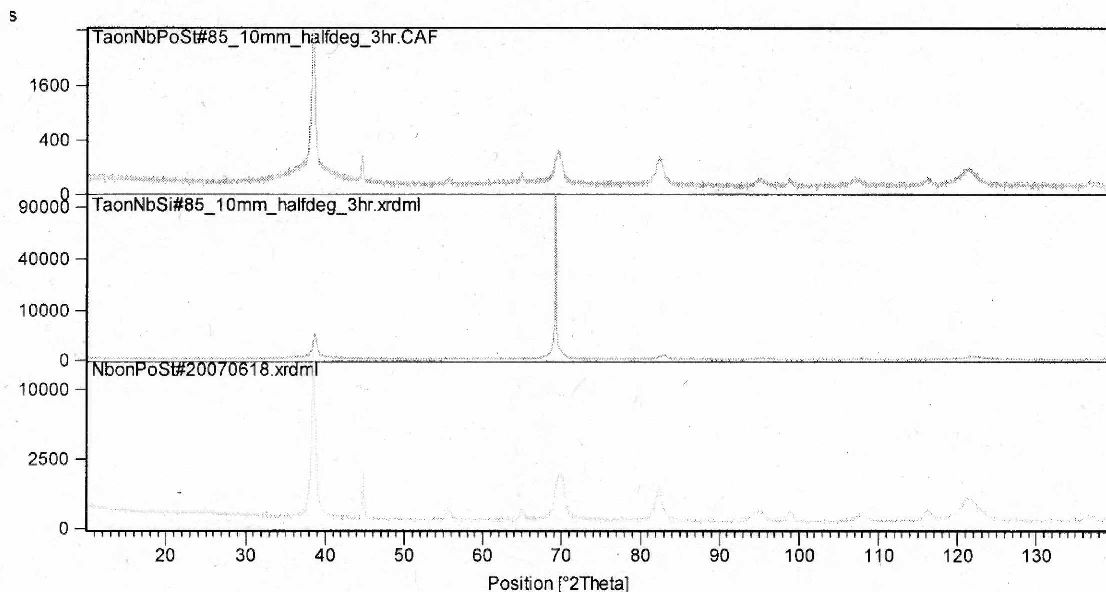

Figure 5.16 XRD patterns of CVD Ta coatings on Nb coated polished steel substrates and Si wafer.

5.5 Ta Coatings on Titanium Seed Layer

Figure 5.17 compares the SEM surface morphology before and after Ta deposited on Ti-coated polished AISI 4340 steel coupon under different magnification. Figure 5.17 (a,b) shows typical sputtering Ti flakes morphology with few defects. Figure 5.17 (c,d) shows that typical round-shape particles of CVD Ta are observed on the surface of Ti coatings after CVD Ta deposited. Lots of big clusters with size about 200nm scatter on the whole surface. Ti feature has been completely covered by the sphere-shape Ta coatings. The results also reveal that the Ta coatings are continuously conformal with few defects.

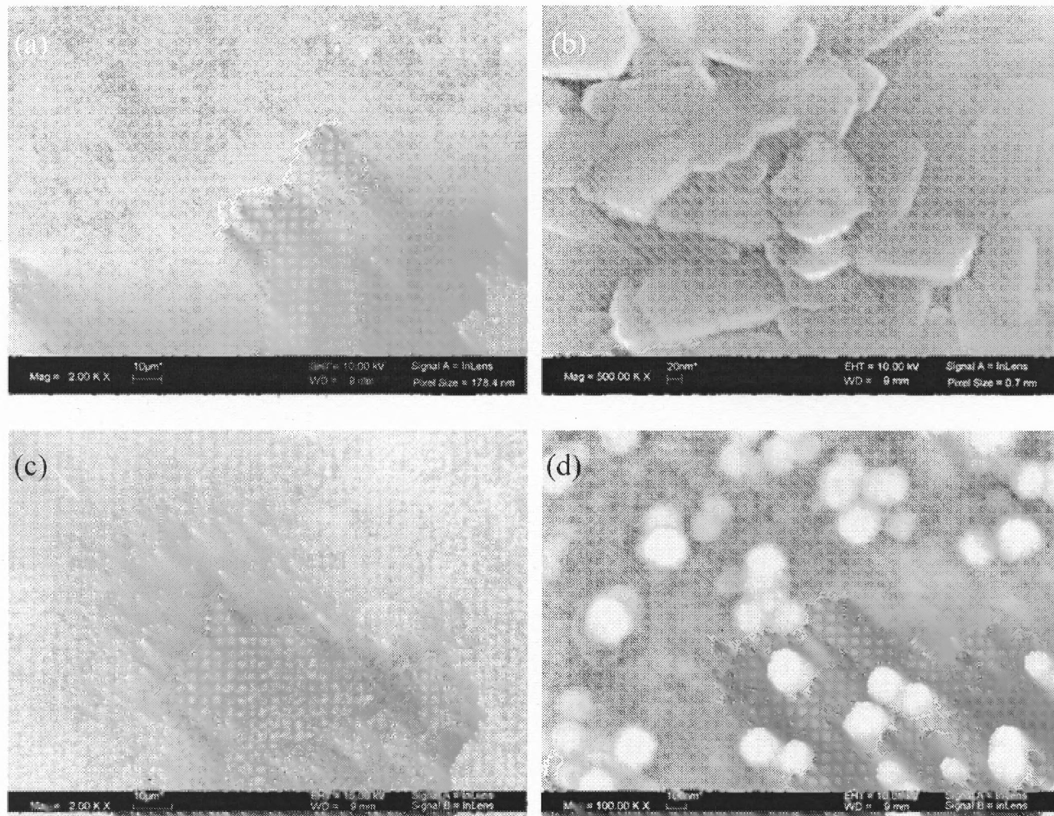

Figure 5.17 Comparison of SEM surface images of CVD Ta coatings deposited on sputtered Ti-coated steel substrates: (a,b) sputtered Ti coating only, (c,d) Ta on Ti-coated steel substrate.

Figure 5.18 illustrates the EDX patterns before and after Ta deposited on sputtered Ti-coated steel substrate. After Tantalum was deposited on Ti coating's surface, the EDX pattern shows clearly Ta Mα line.

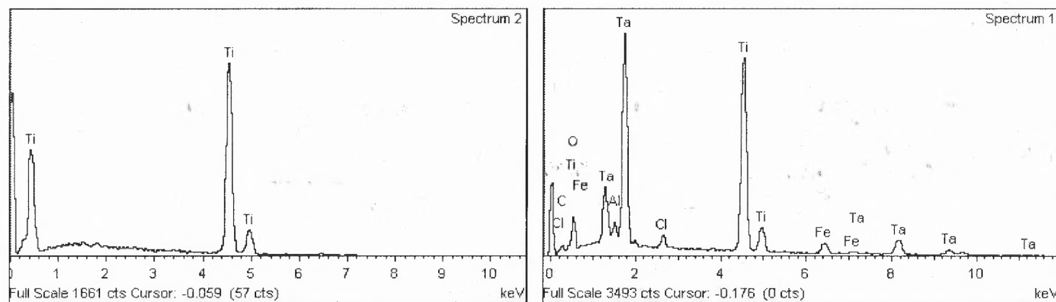

Figure 5.18 EDX patterns of Ta on sputtered Ti coated polished steel substrate

The AFM topography of Tantalum coating on sputtered Ti coated on polished steel substrate is shown in Figure 5.19. The surface roughness is about 28.605 nm.

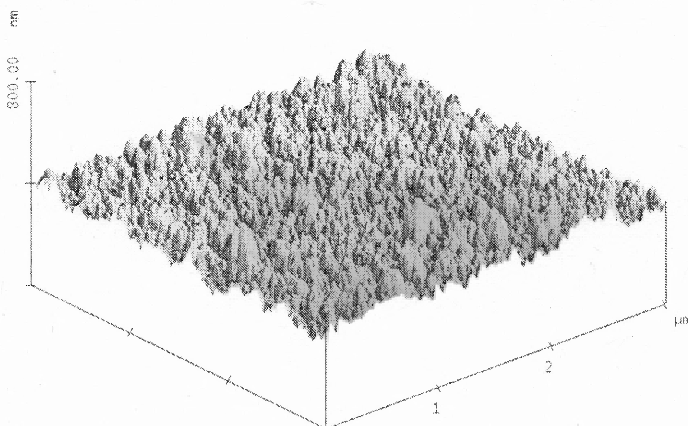

Figure 5.19 Ta AFM 3D topography of sputtered Ti coated on polished steel substrate (Data scale: 400nm, R_{RMS} = 28.605 nm.)

Figure 5.20 illustrates the XRD spectrum of Tantalum coatings on the sputtered Ti-coated on polished steel substrate and sputtered Ti coating as a reference. The peaks of Ti are highly overlapped with both α phase and β phase Ta. Therefore, it is difficult to recognize the peaks of Ta with Ti.

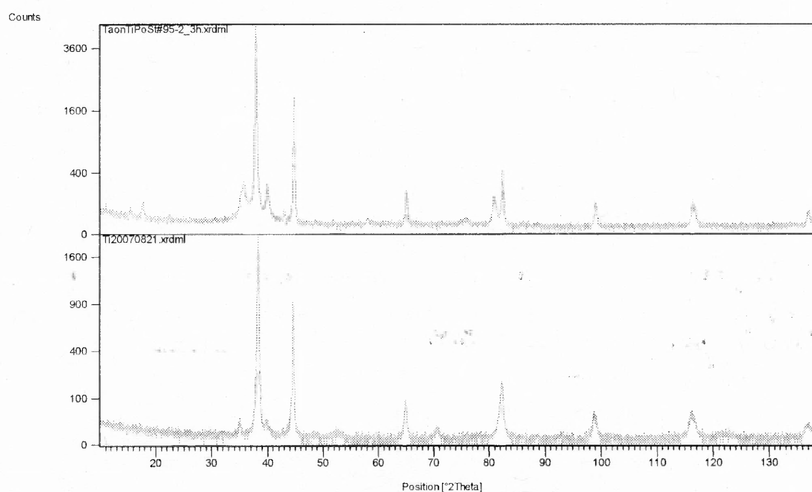

Figure 5.20 XRD patterns of CVD Ta coatings on Ti-coated polished steel substrates.

5.6 Ta Coatings on Platinum Seed Layer

Figure 5.21 compares the SEM surface morphology between sputtered Pt-coated only and after Ta deposited on Pt-coated on polished AISI 4340 steel coupon under different magnification. The very fine Pt coating with a few big clusters morphology is observed. The adhesion of Pt coating with steel substrate is poor. There are lots of crack observed on the Nb coatings.

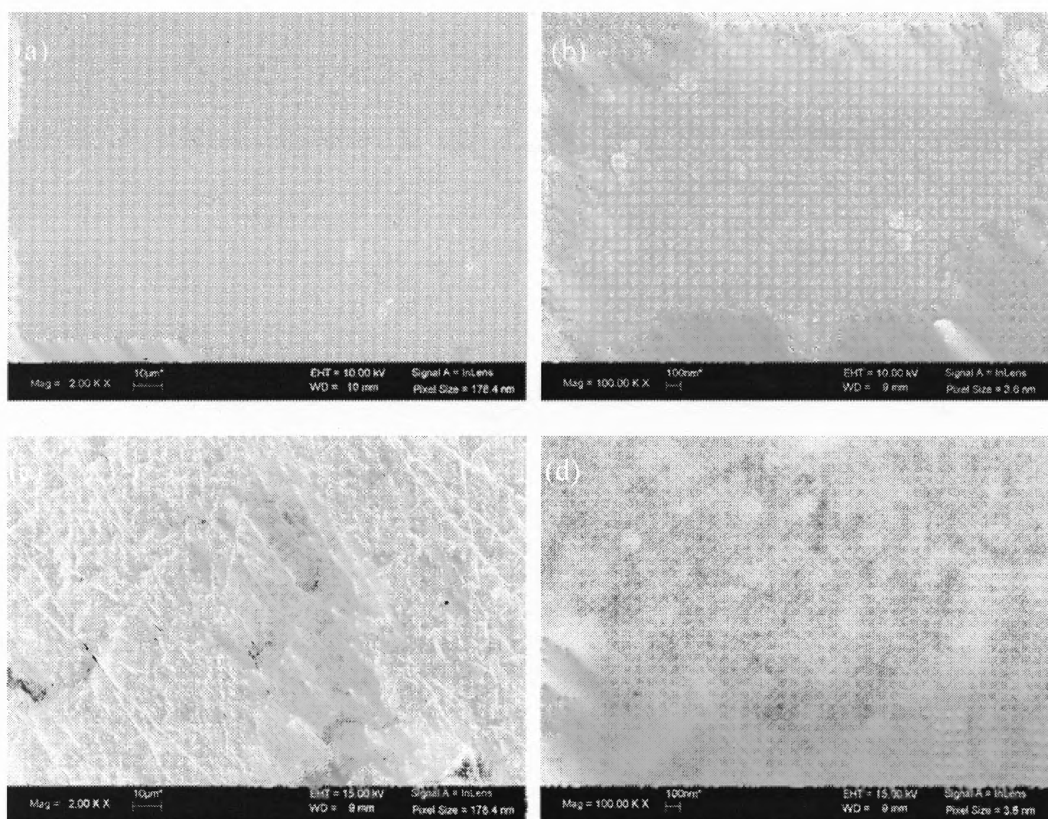

Figure 5.21 Comparison of SEM surface images of CVD Ta coatings deposited on sputtered Pt-coated steel substrates: (a,b) sputtered Pt coating only, (c,d) Ta on Pt-coated steel substrate.

Figure 5.22 illustrates the EDX patterns before and after Ta deposited on sputtered Pt-coated steel substrate. The EDX pattern clearly shows Ta Mα line after Tantalum was deposited on its surface.

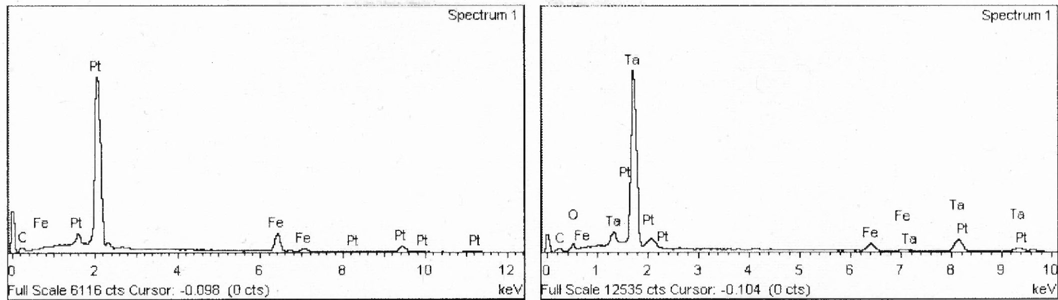

Figure 5.22 EDX patterns of Ta on sputtered Pt-coated polished steel substrate.

The AFM topography of Tantalum coating on Pt-coated on polished steel substrate is shown in Figure 5.23. The surface roughness is about 129.04 nm.

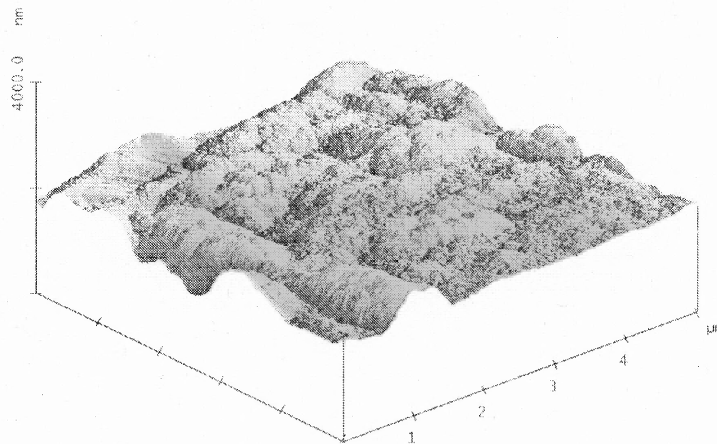

Figure 5.23 Ta AFM 3D topography of Pt-coated on polished steel substrate (Data scale: 400nm, R_{RMS} = 129.04 nm.)

Figure 5.24 illustrates the XRD spectrum of Tantalum coatings on the sputtered Pt-coated on polished steel substrate and sputtered Pt coating as a reference. Although the α-Ta(110) is overlaid with Pt(111), the β-Ta(200) and β-Ta(513) appears on the Ta coating on the Pt-coated steel substrate. It indicates that the Pt could promote β phase formation.

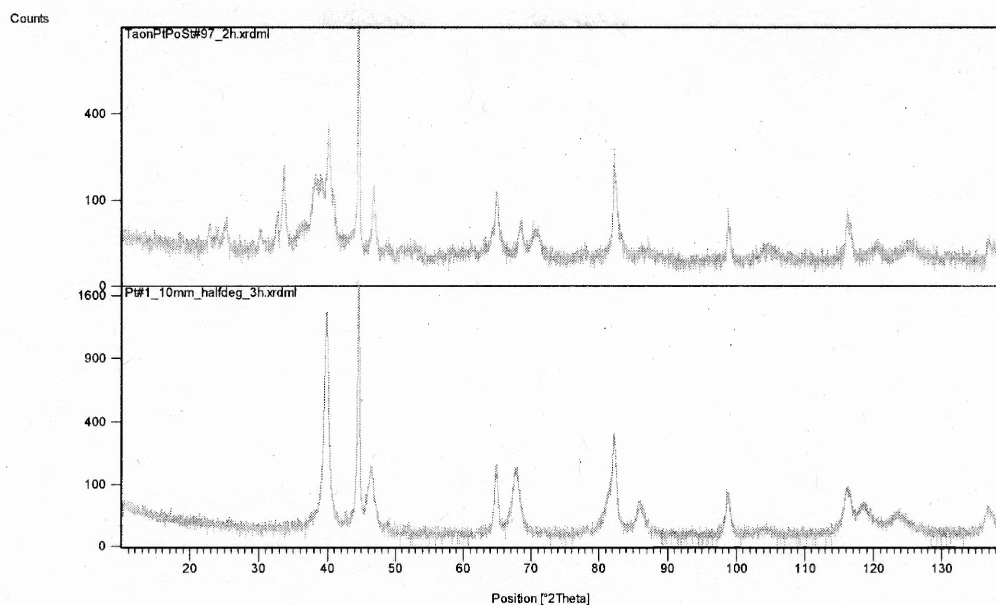

Figure 5.24 XRD patterns of CVD Ta coatings on Pt-coated polished steel substrates.

5.7 Ta Coatings on Tantalum Nitride Seed Layer

The in-situ tantalum nitride (TaN_x) seed layer is produced by using N_2 at the beginning of Ta deposition. The ratio of Ta to N was controlled by changed the flow rate of N_2.

5.7.1 Topographical Characterization

Figure 5.25 shows the typical Tantalum morphology on TaN_x seed layer on polished AISI 4340 coupon under different magnification. The results reveal that the overall surface of the substrates is homogeneously covered by the Ta coating with few defects. The round-shape Ta particles were formed on the TaN_x seed layer. The average size of Ta particles is about 70nm. The elemental analyses by EDX of those coatings indicate that tantalum is the dominant specie with no trace of nitride.

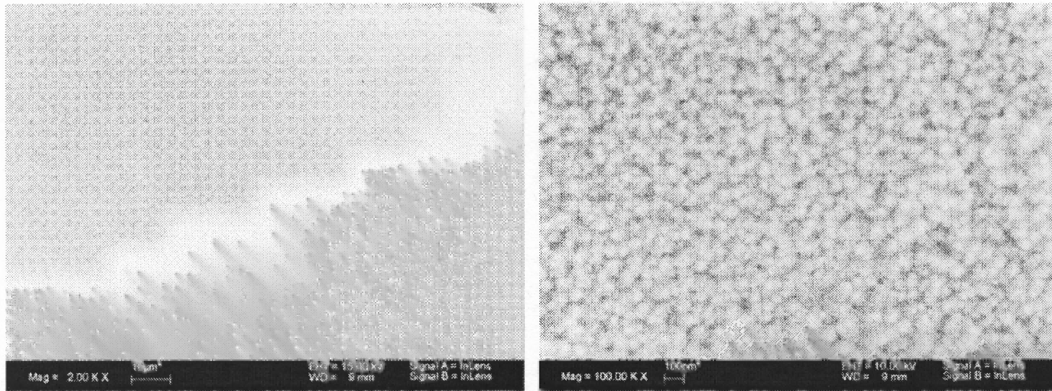

Figure 5.25 SEM surface images of CVD Ta coatings deposited on in-situ TaN_x on polished AISI 4340 steel coupons.

The AFM topography of Tantalum coating on TaN_x seed layer on polished steel substrate is shown in Figure 5.26. The surface roughness is about 26.196 nm.

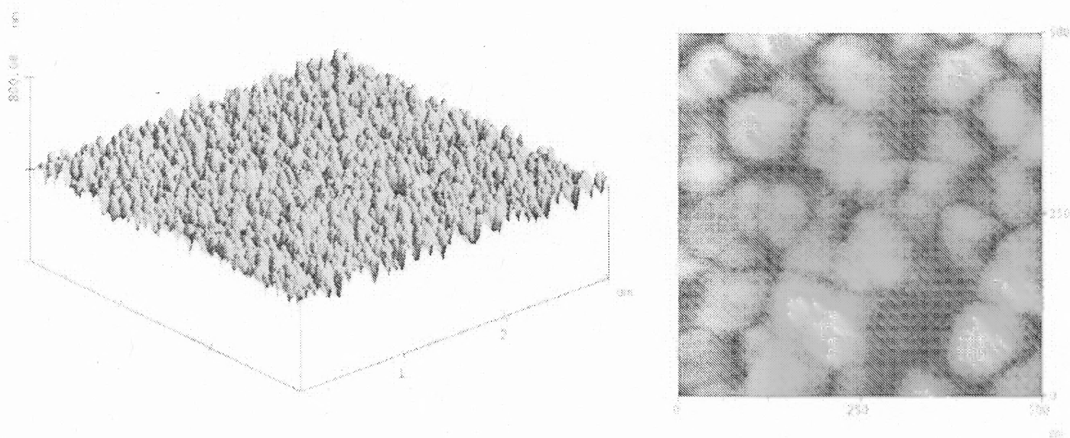

Figure 5.26 Ta AFM 3D and 2D topography of TaN_x seed layer on polished steel substrate (Data scale: 400nm, R_{RMS} = 26.196 nm.)

5.7.2 Step Coverage Characterization

To evaluate the conformal coverage of the Ta coatings, the cross-section of Ta coatings deposited on polished and unpolished AISI 4340 steel substrate was investigated. Cross sectional FE-SEM (Figure 5.27) revealed that the coatings exhibit excellent conformal coverage with uniform coating thickness.

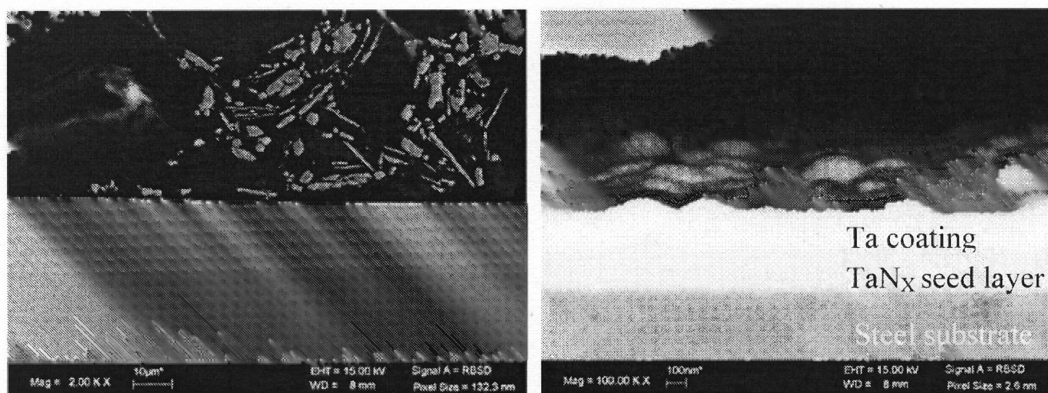

Figure 5.27 The cross-sectional SEM images of Ta coating on in-situ TaN_x seed layer on polished steel coupon

5.7.3 Crystallographic Structures Analysis

The effort has currently been aimed at producing $TaN_{0.1}$ using NH_3 or N_2 in combination with the $TaCl_5$ precursor. The processing conditions are optimized to produce specifically the desirable $TaN_{0.1}$ stoichiometry which will be used to trigger the overlying alpha Ta phase. The crystallographic structures of Ta coatings deposited on TaN_x seed layer on steel substrates were examined using XRD with two theta (2θ) range from 20 to 120°. Figure 5.28 shows Ta coatings on the TaN_x seed layer which was deposited under different N_2 flow rate. The XRD patterns of Ta coatings were compared to those of tantalum references consisting of α and β phases of tantalum (Figure 5.28). By decreased the flow rate of N_2, the β-Ta(200) is disappeared. The proportion of β-Ta phase and α-Ta phase could be changed according to the atom ratio of Ta to N. XRD results of CVD Ta coatings deposited on TaNx seed layers show predominant presence of a phase formation.

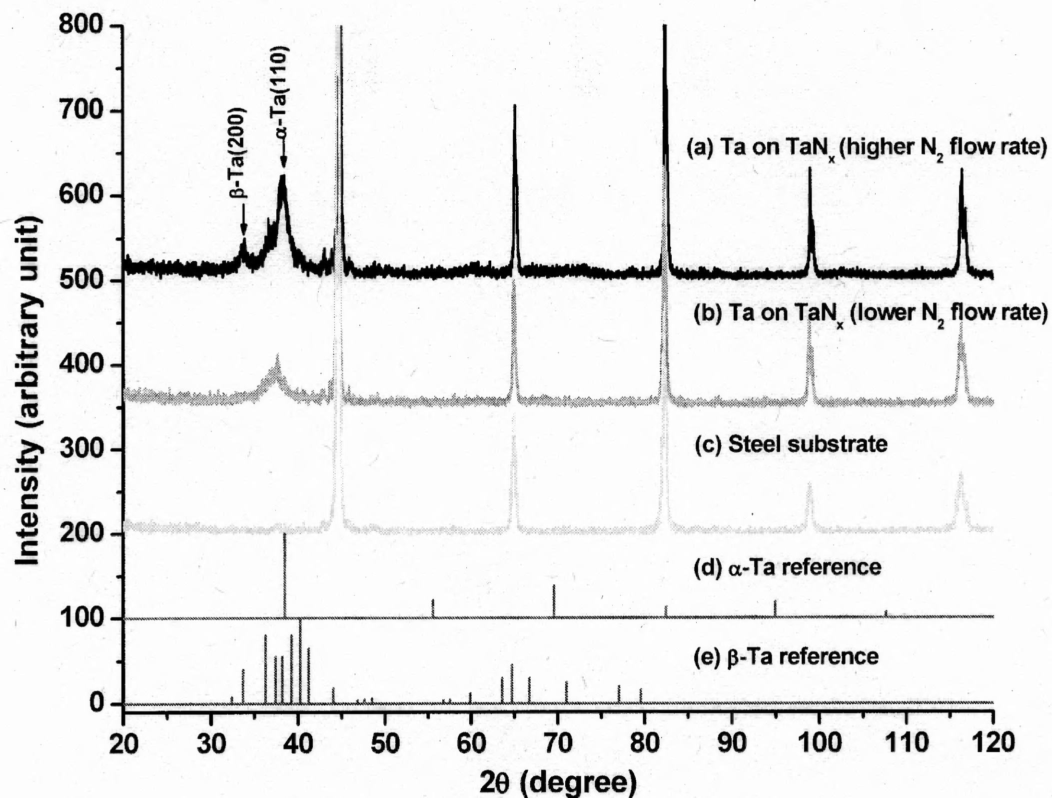

Figure 5.28 XRD patterns of CVD Ta coatings on TaN_x seed layer: (a) Ta on TaN_x (higher N_2 flow rate), (b) Ta on TaN_x (lower N_2 flow rate), (c) steel substrate, (d) α-Ta reference, and (e) β-Ta reference.

5.8 Conclusion

In this chapter, the tantalum coatings on various seed layers have been prepared by PECVD method. The seed layers included Cr, Au, Nb, Pt, Ti, and TaNx. The role of various seed layers were executed to promote the α phase formation. Almost all seed layers were prepared using magnetron sputtered PVD method. The Chromium coatings also were fabricated by electroplated methods. Tantalum Nitride was formed by in-situ reaction using ammonia and nitrogen in combination with the $TaCl_5$ precursor. The results of various characterization studies that were performed on the samples of Tantalum coatings are described. Tantalum coatings have successfully been deposited on various seed layers. The uniform and conformal CVD Ta coatings have been indicated by SEM analysis on all various seed layers. The very fine Tantalum coatings were observed on the seed layers substrates. The AFM analysis indicated that the Ta coatings are continuous and exhibit the typical topography of CVD Ta. Because the particle size of CVD Ta coatings is very small, it always had very low roughness. Therefore, the roughness of Ta samples would be followed the roughness of seed layer substrates. The XRD analysis of the CVD Ta coatings confirmed the presence of α or β phase rich Ta according to different seed layers. XRD analysis indicates that electroplated Cr has a beneficial effect on enhancing α phase formation. CVD Ta coatings deposited on Nb and Au seed layers no longer exhibit evidence of β phase. XRD results of CVD Ta coatings deposited on TaN_x seed layers showed predominant presence of α phase formation.

CHAPTER 6

CONCLUSION

In this work, tantalum coatings have successfully been deposited on steel and silicon substrates by plasma enhanced chemical vapor deposition. The initial goal of this study, which was aimed at developing a process for synthesizing alpha phase tantalum coatings on the AISI 4340 steel coupons that can be used to protect medium caliber gun barrels from wear and erosion, was achieved. After compared all candidate precursor, including organometallic and all halide precursors, the tantalum pentachloride ($TaCl_5$) was chosen as the preferred precursor. This precursor is non-toxic, non-pyrophoric, non-explosive, and carbon-free.

Thermodynamic calculations are carried out for a temperature range from room temperature to 1100 °C. They show that the reaction is endothermic. The enthalpy change for the reaction with TaF_5 is much greater than reactions involving $TaCl_5$ and $TaBr_5$ indicating that a CVD Ta process based on $TaCl_5$ and $TaBr_5$ is expected to require less energy than processes based on TaF_5. Additionally, the Gibbs free energy change indicates that reactions with $TaCl_5$ and $TaBr_5$ show a greater tendency for spontaneity as compared to TaF_5 as the temperature increases. Based on this data, $TaCl_5$ emerged as a promising precursor candidate for Ta deposition. The thermodynamic calculation of Gibbs free energy change reveals that the use of plasma in the CVD Ta process can significantly lower the deposition temperature. The reaction in the presence of plasma spontaneously occurs even at relatively low deposition temperatures.

After loading the substrates into the reactor, in-situ cleaning with excited molecular and atomic hydrogen produced by the RF plasma for 5~20 minutes was

conducted to remove native oxide and organic contaminants. In this study, $TaCl_5$ was used with 10-20 sccm H_2 carrier gas while the gas flow rate of reactant H_2 and dilute He gas was 500 sccm and 150 sccm, respectively. The precursor temperature was in the range of 105-130 °C. The deposition temperature and the reactor pressure were varied in the range of 300~470 °C and 0.7~2 Torr, respectively. The RF power used to produce the plasma was varied in the range of 60~100 W. The plasma working distance is between 1.5" and 2.5".

Ta coatings were characterized with respect to their chemical, structural, and morphological properties by Auger electron spectroscopy (AES), x-ray diffraction (XRD), atomic force microscopy (AFM), x-ray photoelectron spectroscopy (XPS), and scanning electron microscopy (SEM). AFM analysis indicated that the Ta coatings are continuous and exhibit the typical topography expected of CVD metals. SEM/AFM analysis demonstrated that the Ta coatings exhibit continuous coverage with uniform thickness regardless of deposition conditions and the type of seed layers. Performed elemental analysis (EDX) on Ta coatings confirmed formation of high purity Ta coatings under various deposition conditions and with different seed layers. The compositional analyses (AES, XPS and NRA) revealed that CVD Ta coatings are essentially pure with minor impurities of oxygen and chlorine present in the bulk of the coatings. Hydrogen concentration is less than 0.55 at.% in CVD Ta coatings.

The XRD analysis of the CVD Ta coatings confirmed the presence of α or β phase rich Ta according to the deposition condition. These studies indicate that α phase Ta coatings with traces of oxygen, carbon, and chlorine are deposited by PECVD method. The XRD analysis of the CVD Ta coatings confirmed the presence of α or β phase rich

Ta according to the deposition condition. Our results show that the proportion of β phases is increased after decreased the plasma working distance.

The coatings properties have been investigated in relation to deposition temperature, precursor temperature, RF input power and reactant concentration. The XRD data analysis indicated that the in-situ annealing process could promote the β phase formation. A significant enhancement in growth rate was observed by decreasing the distance between the plasma shower head and substrate, and by increasing precursor temperature. XRR measurements showed that the density of the CVD Ta coatings (15.6 g/cm^3) is closed to that of bulk Ta (16.6 g/cm^3).

The various seed layers were used to try to promote the α-phase formation, such as sputtered Cr, electroplated Cr, sputtered Au, sputtered Nb, sputtered Pt, sputtered Ti, and in-situ TaNx. Tantalum coatings have successfully been deposited on various seed layers. The SEM results exhibit dense Ta coatings with perfectly conformal coverage. The typical topography of CVD Ta coatings were indicated by AFM analysis. Ta coatings showed very fine particles size. Therefore, the roughness of Ta coatings always followed the roughness of the seed layer substrates. XRD analysis indicates that mixture α and β phase were deposited on the Cr seed layers, but Cr seed layers do not promote α phase formation. However, sputtered Cr gave more crystalline β phase formation. CVD Ta coatings deposited on Nb and Au seed layers no longer exhibit evidence of β phase. XRD results of CVD Ta coatings deposited on TaN_x seed layers show predominant presence of α phase formation. XRD analysis indicates that electroplated Cr has a beneficial effect on enhancing α phase formation.

REFERENCES

[1] B. C. Arkles, A. E. Kaloyeros, Tantalum and Tantalum-Based Films and Methods of Making the Same, U.S. Patent # 5,919,531, 1999

[2] X. Chen, H. L. Frisch, A. E. Kaloyeros, B. Arkles, J. Vac. Sci. Technol. B 16 (1998) 2887.

[3] A. E. Kaloyeros, X. Chen, S. Lane, H. Frisch, B. Arkles, J. Mater. Res. 15 12 (2000) 2800.

[4] T. T. Kodas, M. J. Hampden-Smith, The Chemistry of Metals CVD, VCH Publishers Inc., 1994, p. 388.

[5] R. A. Levy, X. Lin, J. M. Grow, H. J. Boeglin, R. Shalvoy, J. Mater. Res. 11 (1996) 1483.

[6] S. L. Lee, M. Cipollo, D. Windover, C. Rickard, Surface and Coatings Technology 120/121 (1999) 44.

[7] M. H. Read, C. Altman, Applied Physics letters 7 3 (1965) 51.

[8] A. Schauer, Method of Producing Thin Tantalum Films, Patent # 3,878,079, 1975

[9] S. Sato, T. Inoue, H. Sasahki, Thin Solid Films 86 1 (1981) 21.

[10] J. J. Hauser, J. Appl. Phys. 55 2 (1984) 598.

[11] S. L. Lee, D. Windover, T. M. Lu, M. Audina, Thin Solid Films 420-421 (2002) 287.

[12] D. W. Matson, M. D. Merz, E. D. McClanahan, J. Vac. Sci. Technol. A 10 4 (1992) 1791.

[13] D. W. Matson, E. D. McClanahan, S. L. Lee, D. Windover, Surface and Coatings Technology 146/147 (2001) 344.

[14] W. D. Westwood, N. Waterhouse, P. S. Wilcox, Tantalum Thin Films, Academic Press, London, 1975.

[15] P. N. Baker, Thin Solid Films 14 (1972) 3.

[16] M. H. Rottersman, M. J. Bill, Thin Solid Films 61 3 (1979) 281.

[17] M. Croset, G. Velasco, J. Appl. Phys. 43 4 (1972) 1444.

[18] W. D. Westwood, N. Waterhouse, J. Appl. Phys. 42 7 (1971) 2946.

[19] M. H. Read, D. H. Hensler, Thin Solid Films 10 1 (1972).

[20] D. W. Matson, E. D. McClanahan, J. P. Rice, S. L. Lee, D. Windover, Surface and Coatings Technology 133/134 (2000) 411.

[21] S. L. Lee, M. Doxbeck, J. Mueller, M. Cipollo, P. Cote, Surface and Coatings Technology 177/178 (2004) 44.

[22] D. W. Face, D. E. Prober, J. Vac. Sci. Technol. A 5 6 (1987) 3408.

[23] L. Liu, H. Gong, Y. Wang, J. Wang, A. T. S. Wee, R. Liu, Materials Science and Engineering C 16 1-2 (2001) 85.

[24] K.-W. Kwon, C. Ryu, R. Sinclair, Appl. Phys. Lett. 71 21 (1997) 3069.

[25] K.-W. Kwon, H.-J. Lee, R. Sinclair, Appl. Phys. Lett. 75 (1999) 935.

[26] J. Thewis, Acta Cryst. 5 (1952) 790.

[27] A. Arakcheeva, G. Chapuis, V. Grinevitch, Acta. Cryst. B58 (2002) 1.

[28] A. Arakcheeva, G. Chapuis, H. Birkedal, P. Pattison, V. Grinevitch, Acta. Cryst. B59 (2003) 324.

[29] F. C. Frank, J. S. Kasper, Acta. Cryst. 11 (1958) 184.

[30] J. Hillman, J. Hautala, S. Caliendo, Conference Proceedings ULSI XVI, 2001 MRS, 2001, pp. 313-319

[31] K. Hieber, Thin Solid Films 24 1 (1974) 157.

[32] J. J. Hautala, J. F. M. Westendorp, CVD of Tantalum and Tantalum Nitride Films from Tantalum Halide Precursors, U.S. Patent # 6,900,129 B2, 2005

[33] A. Levesque, A. Bouteville, Chem. Vap. Deposition 10 (2004).

[34] M. Croset, C. Velasco, J. Vac. Sci. Technol. 9 1 (1972) 165.

[35] A. Schauer, M. Roschy, Thin Solid Films 12 2 (1972) 313.

[36] A. P. Mammana, I. L. Torriani, M. A. Silveira, L. A. C. d. Almeida, Vaccum 41 4-6 (1990) 1403.

[37] J. E. Nestell, J. K. J. Scoles, R. W. Christy, Journal of Applied Physics 53 12 (1982) 8993.

[38] K. Hieber, E. Lautenbacher, Thin Solid Films 66 2 (1980) 191.

[39] K. Hieber, N. M. Mayer, Thin Solid Films 90 1 (1982) 43.

[40] S. L. Lee, D. Weindover, Surface and Coatings Technology 108-109 (1-3) (1998) 65.

[41] F. Sajovec, P. M. Meuffels, T. Schober, Thin Solid Films 219 1-2 (1992) 206.

[42] S. Sato, Thin Solid Films 94 (1982) 321.

[43] A. Schauer, W. Peters, Thin Solid Films 8 3 (1971) R9.

[44] A. Schauer, W. Peters, Thin Solid Films 27 1 (1975) 95.

[45] S. Charles, J. Whitman, J. Vac. Sci. Technol. B 18 (2000) 2842.

[46] S. S. Lau, R. H. Mills, Physica Status Solidi (A) Applied Research 17 2 (1973) 609.

[47] L. I. Maissel, P. M. Schaible, J. Appl. Phys. 36 1 (1965) 237.

[48] R. A. Roy, P. Catania, K. L. saenger, J. J. Cuomo, R. L. Lossy, J. Vac. Sci. Technol. B 11 5 (1993) 1921.

[49] P. Catania, R. A. Roy, J. J. Cuomo, J. Appl. Phys. 74 2 (1993) 1008.

[50] P. Catania, J. P. Doyle, J. J. Cuomo, J. Vac. Sci. Technol. A 10 5 (1992) 3318.

[51] D. Fischer, O. Meissner, J. Schreiber, M. Stavrev, C. Wenzel, J. Vac. Sci. Technol. A 15 5 (1997) 522.

[52] R. Hoogeveen, M.Moske, H. Geisler, K. Samwer, Thin Solid Films 275 1-2 (1996) 203.

[53] V. P. Belevskiy, M. V. Belous, V. G. Permyakov, V. M. Yashnik, Physics of Metals and Metallography 33 3 (1972) 105.

[54] V. P. Belevskiy, M. V. Belous, V. G. Permyakov, V. M. Yashnik, Physics of Metals and Metallography 32 6 (1971) 178.

[55] L. G. Feinstein, R. D. Hutteman, Thin Solid Films 16 2 (1973) 129.

[56] N. N. Axelrod, R. B. Marcus, Thin Solid Films 15 (1973) S21.

[57] K. Hieber, N. M. Mayer, Thin Solid Films 90 1 (1981) 43.

[58] R. A. Levy, Microelectronic Materials and Processes, Kluwer Academic Publishers, 1986.

[59] C. H. J. van den Brekel, J. J.M. Blocher, G. E. Vuillard, E. G. Wahl, Proceedings - The Electrochemical Society, 1981, pp. 142-156

[60] K. L. Choy, Progress in Materials Science 48 2 (2003).

[61] K. S. S. Harsha, Principles of Vapor Deposition of Thin Films, Elsevier Science, 2006.

[62] M. Konuma, Film Deposition by Plasma Techniques, Springer-Verlag Berlin and Heidelberg GmbH & Co., 1991, p. 250.

[63] J. L. Vossen, W. Kern, Thin Film Processes II, Academic Press, Inc., 1991.

[64] H. O. Pierson, Handbook of Chemical Vapor Deposition (CVD), Noyes, Park Ridge, NM, 1992.

[65] J. L. Vossen, W. Kern, Thin Film Processes, Academic Press, 1978.

[66] J. A. Papke, R. D. Stevenson, Proc. Conf. Chem. Vap. Deposition Refract. Met., Alloys, Compd., 1967, pp. 193-204

[67] B. C. Arkles, A. E. Kaloyeros, Tantalum and Tantalum-Based Films and Methods of Making the Same, 1999

[68] X. Chen, H. L. Frisch, A. E. Kaloyeros, a. B. Arkles, J. Vac. Sci. Technol. B 16 (1998).

[69] J. J. Hautala, J. F. M. Westendorp, CVD of Tantalum and Tantalum Nitride Films from Tantalum Halide Precursors, 2005

[70] JANAF Thermochemical tables 3rd Ed. J Phys Chem Ref Data, 1986.

[71] N. Schwartz, E. D. Feit, J. Electrochem. Soc.-Solid State Sci Technol 124 (1977) 123.

[72] W. D. Westwood, F. C. Livermore, Thin Solid Films 5 (1970).

[73] D. M. Dobkin, M. K. Zuraw, Principles of Chemical Vapor Deposition, Kluwer Academic Publishers, 2003.

[74] R. A. Levy, J. M. Grow, G. S. Chakravarthy, Chem. Mater. 5 (1993) 1710.

[75] G. S. Chen, S. T. Chen, S. C. Huang, H. Y. Lee, Applied Surface and Science 169-170 (2001) 353.

[76] S. L. Lee, M. Cipollo, D. Windover, C. Rickard, Surface and Coating Technology 120 (1999) 44.

[77] L. Gladczuk, A. Patel, J. D. Demaree, M. Sosnowski, Thin Solid Films 476 (2005) 295.